UNIVERSITY OF WISCONSIN-MADISON

MASTER'S THESIS

A Global Survey of Aerosol Direct Effects

Author:
Alexander V. MATUS

Advisor:
Dr. Tristan S. L'ECUYER

A thesis submitted in partial fulfillment of the requirements for the degree of Master of Science

in the

Atmospheric Radiation and Climate Research Group
Department or Atmospheric and Oceanic Sciences

August 2013

Declaration of Authorship

I, Alexander V. MATUS, declare that this thesis titled, 'A Global Survey of Aerosol Direct Effects ' and the work presented in it are my own.

Alexander V. MATUS
Author

Signature

I hereby approve and recommend for acceptance this work in partial fulfillment of the requirements for the degree of Master of Science:

Tristan S. L'ECUYER
Committee Chair

Signature

Grant W. PETTY
Faculty Member

Signature

Tracey HOLLOWAY
Faculty Member

Signature

Abstract

A Global Survey of Aerosol Direct Effects

by Alexander V. MATUS

Atmospheric aerosols, which alter the global energy budget by scattering and absorbing solar radiation, remain a significant source of uncertainty in our ability to predict future climate. The key to reducing these uncertainties is improved representation of aerosol radiative processes in global models. Multi-sensor observations from the A-Train satellite constellation provide valuable observational constraints necessary to reduce uncertainties in model simulations of aerosol direct effects.

This thesis will discuss recent efforts to quantify aerosol direct effects globally and regionally using CloudSat's new multi-sensor radiative flux and heating rates product. Improving upon previous techniques, this approach leverages the capability of CloudSat and CALIPSO to retrieve vertically-resolved estimates of cloud and aerosol properties critical for accurate assessment of aerosol direct effects.

We estimate the global annual average aerosol direct effect to be -2.0 $\pm$ 0.6 W m^{-2}, which is in better agreement with estimates from global models than previous satellite-based estimates. However, large regional discrepancies exist between modeled and observed estimates of aerosol direct effects. These discrepancies likely result from unrealistic representations of aerosol optical properties and biases in model cloud cover.

A series of regional analyses demonstrate that the magnitude and sign of aerosol direct effects are highly dependent on the surface type and the seasonal distribution of clouds and aerosols. The results from this study evaluate the radiative effects of aerosols on the climate system and offer new insights for improving future estimates.

Acknowledgements

I would like to thank many people who have helped me through the completion of this thesis. I express sincere gratitude to my advisor, Tristan L'Ecuyer, whose expertise, kindness, and patience has enriched my graduate experience. His guidance has helped me develop into a better scientific writer, researcher, and critical thinker. I could not imagine a better advisor and mentor for my graduate studies.

In conjunction with the mentorship of my advisor, I am grateful to work with dynamic and intelligent committee members Grant Petty and Tracey Holloway and appreciate their inputs, insights, and feedback to make this work better. Completion of this thesis would not be possible without the support of AOS faculty, administrators, students, and staff and I appreciate all of their helpful guidance through this process.

I am grateful for the technical support from Dierk Polzin and Pete Pokrandt, who have helped me solve computer and printer problems over the past two years. I would like to thank Norm Wood whose advice and tips in data processing has been invaluable. I am grateful to collaborate with such talented graduate students and officemates whose peer support have helped me along the way. I extend my deepest gratitude to my family for the constant encouragement and support they have provided me.

Contents

Abstract i

Acknowledgements ii

List of Figures vi

List of Tables viii

Abbreviations ix

Symbols xi

1 Introduction 1
- 1.1 Overview of Atmospheric Aerosols . . . 1
- 1.2 Climate Effects of Aerosols . . . 2
- 1.3 Aerosol Direct Effects . . . 4
- 1.4 Research Objectives . . . 9
- 1.5 Significance of Research . . . 10

2 Previous Assessments of Aerosol Direct Effects 13
- 2.1 Introduction . . . 13
- 2.2 Aerosol Measurement Capabilities . . . 13
  - 2.2.1 Ground-based Networks . . . 14
  - 2.2.2 Intensive Field Campaigns . . . 14
  - 2.2.3 Satellite Remote Sensing . . . 15
- 2.3 Measurement-based Estimates . . . 16
- 2.4 Model-based Estimates . . . 18
- 2.5 Reducing Uncertainties in Estimates . . . 19
- 2.6 Remaining Questions . . . 20

3 Data and Methodology 21
- 3.1 Introduction . . . 21
- 3.2 The A-Train Satellite Constellation . . . 21
  - 3.2.1 CloudSat . . . 22

3.2.2 CALIPSO . . . 22
3.2.3 Aqua . . . 23
3.3 CloudSat's 2B-FLXHR-ERB Data Product . . . 23
3.4 Community Earth System Model (CESM) . . . 26
3.5 Methodology . . . 27
3.5.1 Classifying surface types . . . 28
3.5.2 Classifying sky conditions . . . 29

4 Evaluating Global Observations **31**
4.1 Introduction . . . 31
4.2 Data Availability . . . 31
4.3 Global Distribution of All-sky DRE . . . 33
4.4 DRE by Sky and Surface Conditions . . . 37
4.5 Seasonal Variability in DRE . . . 39
4.5.1 Seasonal Maps of Observed DRE . . . 39
4.5.2 Seasonal Cycles in Observed DRE . . . 41
4.6 Global Estimates of Aerosol Direct Effects . . . 43
4.6.1 Previous Estimates . . . 43
4.6.2 2B-FLXHR-ERB Estimates . . . 44

5 Evaluating Global Simulations **48**
5.1 Introduction . . . 48
5.2 Community Earth System Model (CESM) . . . 49
5.3 Global Estimates . . . 49
5.4 Seasonal Variability in DRE . . . 50
5.4.1 Seasonal Maps of Modeled DRE . . . 50
5.4.2 Seasonal Cycles in Modeled DRE . . . 52
5.5 Global Distribution of All-sky DRE . . . 53
5.6 The Role of Sky and Surface Conditions . . . 56

6 Regional Analysis **59**
6.1 Introduction . . . 59
6.2 Overview of Regions . . . 60
6.3 The Americas . . . 61
6.3.1 United States . . . 61
6.3.2 Chile . . . 66
6.4 Africa . . . 72
6.4.1 Sahara . . . 72
6.4.2 Angola . . . 77
6.5 Asia . . . 83
6.5.1 India . . . 83
6.5.2 China . . . 88
6.6 Summary and Discussion . . . 91

7 Conclusions **93**

A 2B-FLXHR-ERB Aerosol Screening **97**

Bibliography **100**

List of Figures

1.1 Aerosol Types . . . 2
1.2 Aerosol Radiative Effects . . . 3
1.3 DRE for Scattering Aerosols . . . 6
1.4 DRE for Absorbing Aerosols . . . 6
1.5 Aerosol Radiative Forcing . . . 11

3.1 A-Train Satellite Constellation . . . 22
3.2 2B-FLXHR-ERB Flowchart . . . 25
3.3 Seasonal Land-Ocean Masks . . . 29

4.1 2B-FLXHR-ERB Sample Count . . . 32
4.2 2B-FLXHR-ERB All-sky DRE and Standard Deviation . . . 34
4.3 2B-FLXHR-ERB DRE by Sky Conditions . . . 38
4.4 2B-FLXHR-ERB All-sky DRE by Season . . . 40
4.5 2B-FLXHR-ERB Time Series . . . 42

5.1 CESM All-sky DRE by Season . . . 51
5.2 CESM Time Series . . . 53
5.3 CESM All-sky DRE . . . 54
5.4 CESM DRE by Sky Conditions . . . 57

6.1 Regional Analysis . . . 61
6.2 USA: Maps . . . 62
6.3 USA: Time Series . . . 63
6.4 USA: Cumulative Density Functions . . . 64
6.5 CHILE: Maps . . . 67
6.6 CHILE: Time Series . . . 69
6.7 CHILE: Cumulative Density Functions . . . 70
6.8 SAHARA: Maps . . . 72
6.9 SAHARA: Time Series . . . 74
6.10 SAHARA: Cumulative Density Functions . . . 75
6.11 ANGOLA: Maps . . . 77
6.12 ANGOLA: Seasonal Maps . . . 79
6.13 ANGOLA: Cumulative Density Functions . . . 81

6.14 INDIA: Maps 84
6.15 INDIA: Time Series 85
6.16 INDIA: Cumulative Density Functions 86
6.17 CHINA: Maps 88
6.18 CHINA: Time Series 90
6.19 CHINA: Cumulative Density Functions 91

A.1 2B-FLXHR-ERB DRE for All Profiles 99

List of Tables

2.1 Previous measurement-based estimates of DRE 17
2.2 Previous model-based estimates of DRE 18

4.1 Fraction of 2B-FLXHR-ERB profiles observed by category 38
4.2 Satellite-based estimates of DRE by category 44
4.3 2B-FLXHR-ERB estimates of DRE (aerosol-only profiles) 45
4.4 2B-FLXHR-ERB estimates of DRE (all profiles) 46

5.1 CESM estimates of DRE by category 50

6.1 USA: Estimates of DRE by category 65
6.2 CHILE: Estimates of DRE by category 71
6.3 SAHARA: Estimates of DRE by category 76
6.4 ANGOLA: Seasonal frequency of occurrence 82
6.5 INDIA: Seasonal frequency of occurrence 87

Abbreviations

AERONET	**AE**rosol **RO**botic **NET**work
AIRS	**A**tmospheric **I**nfra**R**ed **S**ounder
AMIP	**A**tmospheric **M**odel **I**ntercomparison **P**roject
AMSR-E	**A**dvanced **M**icrowave **S**canning **R**adiometer - **E**arth Observing System
AOD	**A**erosol **O**ptical **D**epth
AR4	Fourth **A**ssessment **R**eport of the IPCC
BC	**B**lack **C**arbon
CALIPSO	**C**loud **A**erosol **L**idar and **I**nfrared **P**athfinder **S**atellite **O**bservations
CCN	**C**loud **C**ondensation **N**uclei
CDF	**C**umulative **D**ensity **F**unction
CERES	**C**louds and the **E**arth's **R**adiant **E**nergy **S**ystem
CESM	**C**ommunity **E**arth **S**ystem **M**odel
CTM	**C**hemical **T**ransport **M**odel
CWC	**C**loud **W**ater **C**ontent
DRE	**D**irect **R**adiative **E**ffect
DRF	**D**irect **R**adiative **F**orcing
IPCC	**I**ntergovernmental **P**anel on **C**limate **C**hange
GCM	**G**eneral **C**irculation **M**odel
LW	**L**ong**W**ave
LWC	**L**iquid **W**ater **C**ontent
LLGHG	**L**ong-**L**ived **G**reen**H**ouse **G**ases
MISR	**M**ulti-angle **I**maging **S**pectro**R**adiometer
MODIS	**MOD**erate-resolution **I**maging **S**pectroradiometer

NCAR	**N**ational **C**enter for **A**tmospheric **R**esearch
OC	**O**rganic **C**arbon
OMI	**O**zone **M**onitoring **I**nstrument
POLDER	**POL**arization and **D**irectionality of the **E**arth's **R**eflectances
PDF	**P**robability **D**ensity **F**unction
RF	**R**adiative **F**orcing
RTM	**R**adiative **T**ransfer **M**odel
SPRINTARS	**SP**ectral **R**ad**I**atio**N**-**T**ransport model for **A**e**R**osol **S**pecies
SSA	**S**ingle **S**cattering **A**lbedo
SW	**S**hort**W**ave
TAR	**T**hird **A**ssessment **R**eport of the IPCC
TOA	**T**op **O**f **A**tmosphere

Symbols

A	surface albedo	unitless
$F^{\uparrow}$	upward-directed broadband flux	W m^{-2}
$F^{\downarrow}$	downward-directed broadband flux	W m^{-2}
F_{net}	net flux, defined as $F^{\downarrow} - F^{\uparrow}$	W m^{-2}
g	asymmetry parameter	unitless
τ	optical depth	unitless
ω	single scattering albedo	unitless

Chapter 1

Introduction

1.1 Overview of Atmospheric Aerosols

Atmospheric aerosols are airborne solid and/or liquid particles suspended in the air. Aerosols, typically sized between 1 nm and 100 μm, are small enought to remain suspended in the atmosphere for hours to days. The atmosphere contains many types of aerosols, which are highly variable in size, shape, concentration, and composition, as illustrated in Figure 1.1. The production of aerosols is classified as primary or secondary. Primary aerosols are emitted directly into the atmosphere, whereas secondary aerosols form as a result of gas-to-particle reactions with precursor species. Both primary and secondary aerosols derive from a variety of natural and manmade sources.

Natural aerosols (e.g. sea salt, mineral dust, and volcanic ash) are typically larger than one micron, which is commonly referred to as the coarse mode. Manmade, or anthropogenic, aerosols (e.g sulfate and nitrate) are typically smaller than one micron, which is called the fine mode. Some particles, including organic and black carbon, may have either natural or anthropogenic origins. Averaged globally, nearly 90% of aerosols (by mass) have natural origins, while anthropogenic aerosol comprise the remaining 10% (Schulz et al., 2006). Despite their relative scarcity on a global scale, anthropogenic aerosols can dominate locally near areas of heavy industry or agricultural burning.

In some parts of the world the quantity and composition of atmospheric aerosols has greatly increased in recent years due to changes in land use (such as deforestation,

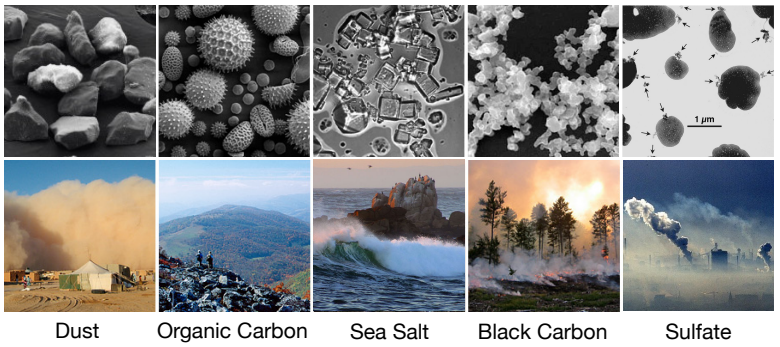

FIGURE 1.1: Aerosols exist over a wide range of sizes, shapes, and concentrations.

overgrazing, and irrigation practices) and fossil fuel emissions from industrial, residential, commercial, and agricultural sectors. Observed aerosol concentrations are typically largest in the atmospheric boundary layer, with concentrations decreasing with altitude in the free troposphere.

Within the troposphere, aerosols are primarily removed through cloud processing and precipitation; wet deposition limits aerosol atmospheric lifetimes to a week or less. However, aerosols from volcanic eruptions and wildfire smoke may be lofted above the troposphere to the stratosphere, where their atmospheric lifetimes are extended to months or years. The length of time in which aerosols reside in the atmosphere increases their potential impact both spatially and climatically.

1.2 Climate Effects of Aerosols

Atmospheric aerosols can have a profound impact on the climate system by altering the global energy budget. As reproduced from the IPCC Fourth Assessment Report (AR4), Figure 1.2 illustrates three pathways by which aerosols may perturb radiative balance: the direct effect, indirect effect, and semi-direct effect.

First, the *aerosol direct effect* is the process in which particles directly interact with light, by scattering and absorbing sunlight. Scattering aerosols cool the atmosphere, whereas absorbing aerosols warm the atmosphere. Most aerosol constituents have a single scattering albedo greater than 0.9, which means the particles effectively scatter

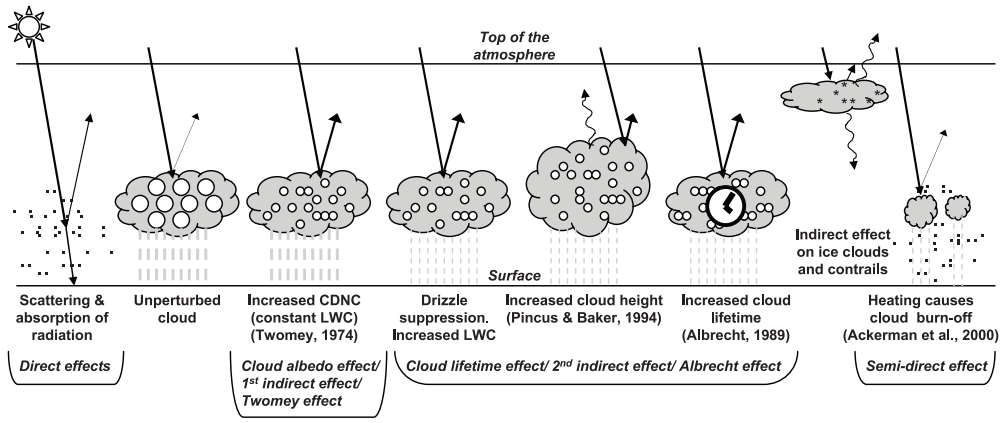

FIGURE 1.2: Aerosols may alter global radiative balance through direct, indirect, and semi-direct effects (Forster et al., 2007).

over 90% of incident light (Ramanathan et al., 2001). Some aerosol constituents, such as black carbon, absorb solar radiation which locally heats the atmospheric column. Averaged globally, scattering aerosols predominate over absorbing aerosols. Overall, the presence of aerosol particles enhances the backscatter of solar radiation to space and leads to a net cooling of the climate system (Ocko et al., 2012).

Second, the *aerosol indirect effect* describes how particles interact indirectly with light, by modifying cloud microphysical properties. Submicron particles may serve as sites on which water vapor condenses into cloud droplets. Higher concentrations of aerosol particles are expected to increase cloud droplet concentrations while reducing the size of each droplet, under the assumption of constant liquid water path. The result is increased cloud albedo, which is termed the first indirect effect (Twomey, 1974).

A reduction in droplet size also decreases the efficiency of warm cloud precipitation and increases cloud height. The presence of aerosols can lead to longer-lived clouds, a phenomenon termed the second indirect effect (Albrecht, 1989). Through indirect effects, aerosols perturb radiative fluxes not by direct interaction with light, but rather by altering the microphysical properties of clouds. The net result of direct and indirect aerosol effects is a brightening of Earth's reflectance and, hence, and a net cooling of the climate system.

Finally, the *aerosol semi-direct effect* is the process by which atmospheric heating from absorbing aerosols can reduce cloud cover and liquid water path. The semi-direct effect is a phenomenon in which aerosols directly interact with light to influence cloud properties. Black carbon, found in soot, is an absorbing aerosol that may contribute to the semi-direct effect. The presence of absorbing aerosols near clouds can heat the atmospheric column and promote cloud burn-off. Furthermore, these aerosols may reduce relative humidity and alter tropospheric stability. The result of the semi-direct effect is proposed to affect radiative balance by modifying cloud properties, although the magnitude of the effect is still highly uncertain.

1.3 Aerosol Direct Effects

This study will focus entirely on assessing aerosol direct effects using state-of-the-art satellite observations. The direct radiative effect (DRE) is defined as the perturbation of net radiative flux due to the presence of aerosols.

$$DRE = \left(F^{\downarrow} - F^{\uparrow}\right)_{aero} - \left(F^{\downarrow} - F^{\uparrow}\right)_{noaero} \tag{1.1}$$

By convention, a positive DRE at the top-of-atmosphere (TOA) denotes an addition of energy to the earth-atmosphere system (a warming effect), whereas a negative DRE denotes a loss of energy from the earth-atmosphere system (a cooling effect). Although aerosols can interact with both shortwave (0.1-4 μm) and longwave (4-50 μm) radiation, shortwave effects tend to be much larger. Thus, aerosol direct effects are commonly assessed only for interactions with shortwave radiation.

Although DRE may be evaluated at any level of the atmosphere, from a radiative balance perspective, the two most important levels to consider are the TOA and surface. These levels represent the upper and lower boundaries of the climate system. Also commonly evaluated is aerosol atmospheric heating, which is defined as the difference between DRE at the TOA and surface.

In addition to the amount of aerosol present, the direct radiative effect is highly dependent on single scattering albedo (SSA), which represents the ratio of scattering to

total extinction. Whereas sulfate and sea salt aerosols (SSA $\simeq$ 1.0 at 0.5 μm) are mostly scattering in the visible spectrum, black carbon aerosols (SSA $\simeq$ 0.2 at 0.5 μm) are considerably more absorbing (Ramanathan et al., 2001). Nearly all aerosols are composed not of a single specie, but rather an amalgamated mixture of several consituents with highly variable optical properties.

Biomass burning aerosols, composed of black carbon, organic carbon, and inorganic compounds, have a 0.55$-\mu$m SSA between 0.85 and 0.89, based on measurements from the Aerosol Robotic Network (AERONET) (Eck, 2003). Aged biomass burning aerosols are less absorbing with an SSA of 0.91, resulting from the condensation of non-absorbing organic gases on existing aerosol particles (Haywood, 2003). Furthermore, biomass burning aerosols from boreal forests tend to have weaker absorption than biomass burning aerosols produced from tropical fires (Wong and Li, 2002).

Arid regions also contribute aerosols through the emission of dust. Mineral dust aerosols have a 0.67$-\mu$m SSA of 0.95 over the Sahara and a 0.67$-\mu$m SSA of 0.93 over China, according to AERONET measurements (Dubovik and Holben, 2002, Mikami et al., 2006). Although less absorbing than black carbon, mineral dust is one of the most abundant aerosol species globally, with an anthropogenic contribution ranging between 30 and 50% (Tegen and Fung, 1995). Overall, particles that absorb solar radiation, including those from biomass burning and mineral dust, reduce the effective SSA of aerosols which strongly influences radiative transfer through the atmosphere.

Most aerosols in the Northern Hemisphere have a SSA between 0.85 and 0.95. This is important because aerosols generally exert a net negative DRE when SSA exceeds 0.95, and a net positive DRE when SSA is less than 0.85 (Ramanathan et al., 2001). In this study, particles with an SSA greater than 0.95 are termed scattering aerosols and those with an SSA less than 0.85 are termed absorbing aerosols. Scattering and absorbing aerosols elicit various responses on radiative heating throughout the atmosphere, as conceptualized in Figures 1.3 and 1.4.

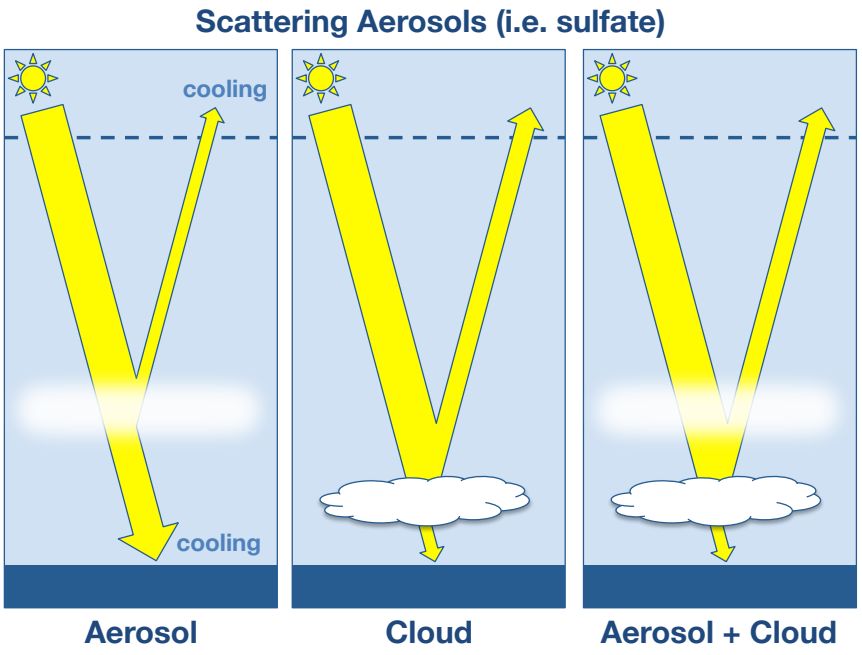

FIGURE 1.3: Scattering aerosols (i.e. sulfate) in cloud-free air (left) result in a negative aerosol direct effect, or cooling, at the top-of-atmosphere.

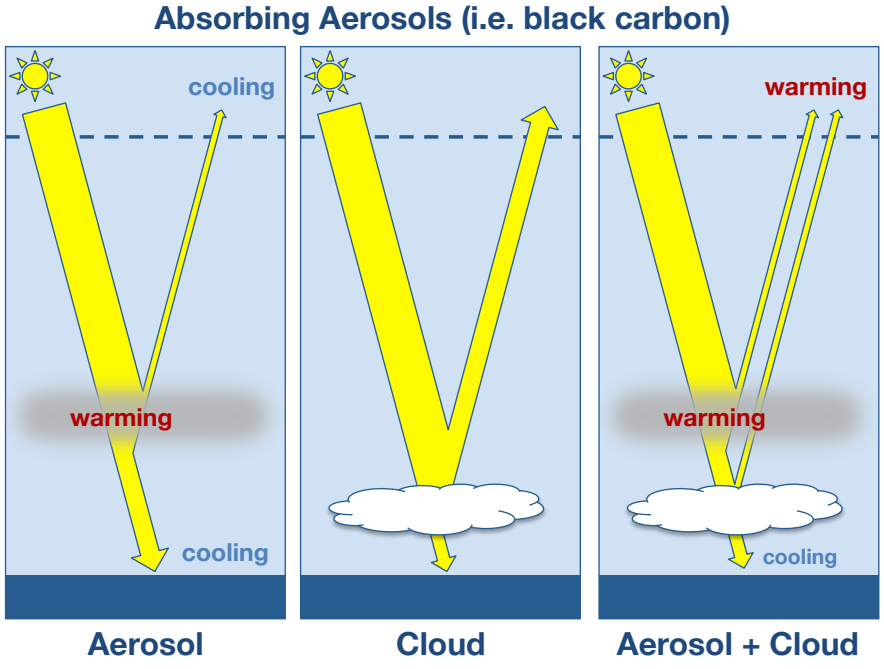

FIGURE 1.4: Absorbing aerosols (i.e. black carbon) over bright surfaces and clouds (right) result in a positive aerosol direct effect, or warming, at the top-of-atmosphere.

Figure 1.3 displays three scenarios in which solar radiation is modified by the presence of clouds and/or scattering aerosols. In the left panel, bright aerosols overlay a dark ocean surface. Sunlight is reflected off the aerosols back to space. This produces a negative DRE, or cooling, at the TOA and surface. In the center panel, a bright cloud is present over a dark surface. Since no aerosols exist in this scenario, there is no aerosol DRE but the cloud enhances the amount of reflected radiation. In the right panel, we observe bright aerosols over a bright cloud. Since the cloud is brighter than aerosols, there is no flux perturbation due to aerosols. Consequently, there is no aerosol DRE when scattering aerosols are present over bright clouds.

Whereas scattering aerosols are largely responsible for cooling at the TOA, the same does not necessarily hold true for absorbing aerosols. Figure 1.4 shows three scenarios in which solar radiation is modified by the presence of clouds and/or absorbing aerosols. In the left panel, dark aerosols overlay an even darker ocean surface. Only a small fraction of sunlight is reflected off of the aerosols back to space. This produces slight cooling at the TOA, warming within the aerosol layer, and cooling at the surface. In the right panel, dark aerosols overlay a bright cloud. Sunlight is absorbed within the aerosol layer, which reduces the quantitiy of solar radiation that can be reflected off of the cloud. This scenario produces warming at the TOA, warming within the aerosol layer, and cooling at the surface.

Although aerosol research has been conducted since the 1960's, the role of aerosols in climate was not widely recognized until the early 1990's (Charlson et al., 1992). During this time, aerosols were identified as a critical missing component in global models that were needed to accurately simulate observed temperature trends over the industrial period. The inclusion of aerosols in climate models have made it possible to simulate aerosol processes and perform global assessments of aerosol radiative effects.

In recent years, improved aerosol datasets from surface, air, and space-based observing platforms have shifted estimates of aerosol radiative effects from largely model-based in IPCC TAR (2001) to increasingly measurement-based in IPCC AR4 (2007)

(CCSP, 2009). However, the quantification of aerosol radiative effects has proven challenging for both model-based and measurement-based assessments due to large variations in aerosol compositions, distributions, and lifetimes.

While a flux perturbation by all aerosols is called an *aerosol radiative effect*, a flux perturbation by only anthropogenic aerosols is called an *aerosol radiative forcing*. Averaged globally, aerosol radiative forcing is likely negative and comparable in magnitude to the forcing from anthropogenic greenhouse gases (Forster et al., 2007). In regions with high concentrations of anthropogenic particles, aerosol forcing can be much larger than the global average, and even exceed the magnitude of greenhouse gas forcing (NRC, 2005). However, aerosol forcing is more difficult to quantify than greenhouse gas forcing. Aerosols are more variable in space and time due to the short atmospheric lifetimes of aerosols, the intermittency of aerosol sources, and the complex interactions of aerosols with clouds and precipitation. Due to limited understanding of aerosol properties on global scales, current estimates of aerosol radiative effects remain uncertain.

The U.S. Climate Change Science Program identified three areas necessary for reducing aerosol forcing uncertainties: (i) improving measurement quality and coverage, (ii) achieving effective use of these measurements to constrain models, and (iii) producing a more accurate representation of aerosols and clouds in models (CCSP, 2009). In the past decade, significant efforts have been made to integrate data from a variety of platforms (ground-based networks, ship, aircraft, and satellite) and techniques (in-situ measurement, remote sensing, numerical modeling, and data assimilation). While significant progress is being made, there are still substantial uncertainties associated with aerosol forcing that inhibit informed decisions on climate policy.

One of the greatest challenges in studying aerosol properties is characterizing the large diversity of aerosol sizes, compositions, sources, spatial distributions, and temporal distributions. Over the past two decades, dedicated aerosol field experiments and ground-based networks have provided detailed measurements of aerosol physical, chemical, and optical properties. However, these measurements fail to capture the large spatial and temporal heterogeneity of aerosol distributions essential for estimating aerosol radiative effects on global scales. Satellite remote sensing remains the

only means of translating information from localized field measurements to characterize aerosol properties over broad spatial and temporal scales.

The most important properties for assessing radiative effects are aerosol optical depth (AOD), single scattering albedo (SSA), and asymmetry parameter. AOD is the column-integrated magnitude of light extinction from aerosols. SSA is the ratio of the scattering coefficient to the extinction coefficient. The asymmetry parameter is the cosine-weighted average of the scattering phase function. Accurate representation of these aerosol optical properties is critical for global assessments of aerosol direct effects.

To date, satellite estimates of aerosol DRE have relied on passive instruments including the Moderate-resolution Imaging Spectroradiometer (MODIS), Multi-angle Imaging Spectroradiometer (MISR), Polarization and Directionality of the Earth's Reflectances (POLDER), Ozone Monitoring Instrument (OMI), and Clouds and the Earths Radiant Energy System (CERES). While these estimates have provided useful benchmarks for model evaluation, passive sensors are typically only able to retrieve aerosol optical properties under clear-sky conditions.

Although some methods have been developed to evaluate DRE over land by integrating satellite and model data, most satellite estimates of DRE currently report values only over ocean. These limitations severely reduce sampling, lead to a clear-sky bias, and introduce systematic error for retrievals sampled in the proximity of clouds. The accuracy of AOD from passive sensors (0.05 to 0.20) is severely compromised compared to that of ground-based sun-photometers (0.01 to 0.02) (Kahn, 2005, Remer et al., 2005). Passive retrievals of AOD tend to exhibit greatest accuracy over dark ocean surfaces.

1.4 Research Objectives

This research approach overcomes previous observational limitations using new multi-sensor aerosol, cloud, precipitation, and radiative flux products from the A-Train satellite constellation. The dataset features collocated observations from CloudSat, CALIPSO, MODIS, and AMSR-E, specifically designed to detect the precise location of clouds, aerosols, and precipitation with complementary estimates of water contents, AOD,

and precipitation intensity. This combination of active and passive observations has the unique capability of estimating aerosol radiative effects in historically poorly sampled regions including those above clouds and over land surfaces. Our main objectives focus on testing the following hypotheses:

1. The combination of active and passive observations will provide a more complete assessment of global aerosol DRE than conventional estimates based exclusively from passive observations.

2. Biases in model DRE will be largest over regions where cloud fields are poorly simulated, for example, stratocumulus in the southeast Pacific.

3. Integrating data from complementary sensors may ultimately improve our ability to assess the radiative forcing contribution from anthropogenic aerosols.

The study objectives are designed to leverage the strengths of CloudSat and CALIPSO cloud and aerosol observations in the context of broader swath AMSR-E and MODIS products to improve estimates of the direct radiative effects of aerosols on global scales. Improved aerosol measurements are expected to lead to a more realistic representation of aerosol processes in global climate model (GCM) simulations.

1.5 Significance of Research

This study addresses key issues in understanding the radiative effects of aerosols in the climate system through the synthesis of satellite and model analyses. It embraces NASA's goal of using Earth system observations to improve understanding of important processes in the Earth-atmosphere system and improve climate predictability. The results of this study are expected to advance current understanding of aerosol radiative effects and reduce uncertainties in representing these effects in climate models.

Dedicated aerosol research over the past two decades has greatly advanced our understanding of complex aerosol processes. Despite increased knowledge on aerosol-radiation interactions, there remain significant uncertainties concerning the role of aerosol

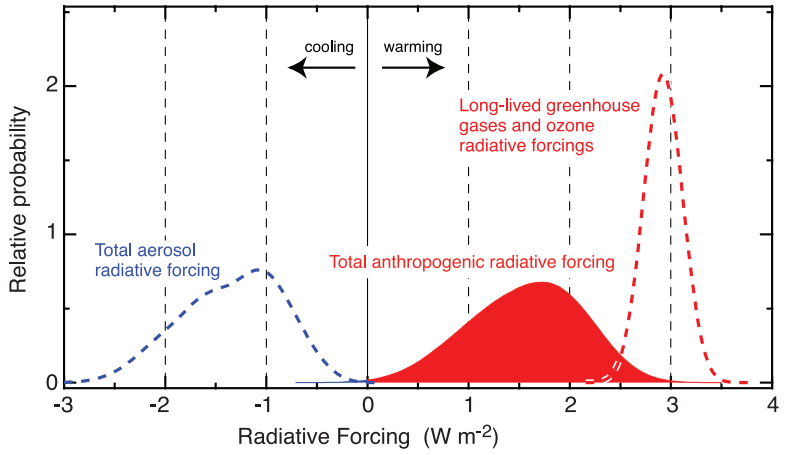

FIGURE 1.5: The cooling from aerosol radiative forcing partially offsets the warming from greenhouse gas radiative forcing (Forster et al., 2007).

forcing of the climate system. Currently, the large uncertainty in aerosol radiative forcing (RF) from preindustrial times to the present must be reduced to allow for meaningful projections of future climate.

According to the IPCC AR4, the present-day global average anthropogenic RF is +2.9 W m^{-2} (with a 90% confidence interval of 2.6 to 3.2 W m^{-2}) from long-lived greenhouse gases and -1.3 (-2.2 to -0.5) W m^{-2} from aerosols. This produces a total anthropogenic RF of +1.6 (0.6 to 2.4) W m^{-2}, as shown in Figure 1.5. Given an increase in global mean surface temperature of 0.7°C since preindustrial times, the RF response yields a transient climate sensitivity of 0.3 to 1.1°C/(W m^{-2}).

Most global emission scenarios anticipate a doubling of CO_2 by the second half of the 21st century, which equates to a RF of about 4 W m^{-2}. Therefore, the estimated surface temperature increase due to doubled CO_2 ranges from 1.2 to 4.7°C. This range of uncertainty in projected temperatures is considerably large for climate policy. The largest contribution to the overall uncertainty is aerosol RF, which underscores the need for improved measurements of aerosol radiative properties.

Over the past decade, there has been significant progress in improving aerosol measurements from a variety of observing platforms, including satellite, airborne, and ground-based, and laboratory instrumentation. Each observing platform has strengths and weaknesses for sampling measured quantities. Laboratory measurements provide

highly detailed characterization of aerosols under limited atmospheric conditions. Aircraft and ground-based sampling can accurately measure physical and chemical properties, albeit with limited spatial and temporal coverage. These measurements are often used to better constrain more global evaluations of aerosol properties from GCM simulations and satellite observations.

Satellite observations offer the greatest spatial coverage of aerosol measurements. The wide spatial coverage of satellites provides the unique opportunity to perform global assessments of aerosol radiative effects from observations. Satellite passive imagers can retrieve daily AOD globally over cloud-free and dark surfaces. Space-based lidars can retrieve the vertical distribution of aerosol properties along the orbital path of the instrument. Despite global coverage, the sampling from satellite observations is often an issue of concern. For this reason, measurements from multiple satellite platforms, often combined with model simulations to fill in the gaps, are synthesized for more comprehensive retrievals of desired aerosol properties.

The coordinated efforts of data integration mark a critical step for advancing the quality of aerosol measurements. Despite limitations inherent in all observational data techniques, the individual strengths of each may be exploited through effective data integration. Complementary sensors from multiple platforms and datasets provide the necessary observational constraints to reduce uncertainties in the retrieval of aerosol properties. High-quality observations improve climate model simulations of aerosol radiative effects. The effective use of advanced instrument platforms, coordinated measurement strategies, and numerical techniques offer important advances toward reducing uncertainties in current estimates of aerosol radiative effects.

Collectively, the sensors aboard the A-Train satellite constellation offer an unprecedented dataset for assessing the climate impact of aerosols. A key advantage of these measurements is the ability to detect aerosols in the presence of clouds. Vertically-resolved profiles of aerosol radiative properties is achieved using a combination of active and passive sensors from the A-Train. Together, these sensors provide the accuracy and spatial coverage necessary for improving global assessments of aerosol DRE.

Chapter 2

Previous Assessments of Aerosol Direct Effects

2.1 Introduction

As discussed in Chapter 1, the chief difficulty in assessing aerosol radiative effects arises from the large spatial and temporal heteorogeneity of aerosol sizes, shapes, concentrations, and compositions. Accurately characterizing aerosol properties has proven challenging in previous assessments of aerosol direct effects. Measurements or model simulations alone are often inadequate for characterizing the wide diversity of aerosol properties. For this reason, global assessments of DRE require an integrated approach which effectively combine measured observations and model simulations.

2.2 Aerosol Measurement Capabilities

Measurements of aerosol properties provide useful constraints on model simulations of aerosol processes. The accuracy of a measurement needs to be sufficiently high to achieve the desired accuracy for radiative forcing estimates. For example, to obtain an accuracy of 1 W m^{-2} in instantaneous estimates of TOA clear-sky aerosol DRE, the accuracy of measured AOD must be within 0.02 and the accuracy of SSA must be within 0.02 over land (CCSP, 2009). To achieve the same forcing accuracy at the surface, an

even tighter measurement accuracy is required. The importance of measurement accuracy highlights the need for high-quality datasets of aerosol optical properties.

There currently exist several platforms for measuring aerosol optical properties. These include ground-based networks, field campaigns, and satellite remote sensing. Each measurement technique has advantages and disadvantages. Errors in the measurement of aerosol optical properties can significantly bias the estimate of the aerosol direct effect, which will be discussed in greater detail later in this chapter.

2.2.1 Ground-based Networks

Ground-based networks provide highly accurate measurements of aerosol properties at fixed locations over extended periods of time. The largest ground-based aerosol network in the world is the Aerosol Robotic Network (AERONET).

Comprised of over 200 sites globally, AERONET performs high quality measurements of all major tropospheric aerosol regimes using a connected suite of well-calibrated sun photometers and radiometers. Spectral measurements of sun and sky radiance are calibrated and screened for cloud-free conditions (Smirnov et al., 2000). Stations measure spectral AOD at 440, 670, 870, and 1020 nm with an accuracy of ± 0.015. SSA is measured with an accuracy of ± 0.03 provided AOD is greater than 0.4.

AERONET measurements provide a high-quality climatology of aerosols near the surface. Data are uniformly acquired and processed at all stations which, in some cases, have been in continuous operation for over 10 years. The measurements are complementary to other ground-based aerosol networks with lesser spatial or temporal coverage, including the Department of Energy's Atmospheric Radiation Measurement (ARM) network, NOAA's national SURFace RADiation budget (SURFRAD) network, NASA's Micro Pulse Lidar NETwork (MPL-NET), and the European Aerosol Research Lidar NETwork (EARLINET).

2.2.2 Intensive Field Campaigns

Field experiments provide the opportunity to combine in situ and remote sensing observations of physical and chemical aerosol properties from a variety of measurement

platforms. Ground-based, aircraft, ship, and satellite observations are synthesized over limited spatial and temporal domains to study aerosol processes in exhaustive detail. Field campaigns are typically conducted downwind of known continental aerosol source regions, such as North America, East Asia, and North Africa. Intensive measurements coupled with model simulations allow field experiments to vastly improve physical and microphysical understanding of regional aerosols in the atmosphere over time periods ranging from weeks to months.

2.2.3 Satellite Remote Sensing

Satellite remote sensing remains the only way of characterizing the large spatial and temporal heterogeneities of aerosol optical properties. Space-based monitoring of aerosols has been performed for over two decades. Although originally designed for other purposes, the earliest aerosol sensors provided benchmark studies of global aerosol distributions. These instruments, both launched in 1978, include the Advanced Very High Resolution Radiometer (AVHRR) and the Total Ozone Mapping Spectrometer (TOMS). AVHRR, a weather satellite sensor, observed radiances in the visible and near infrared wavelengths which could be used to retrieve aerosol properties over the ocean. TOMS, an ozone monitoring sensor, featured UV channels sensitive to aerosol absorption over ocean and land.

More recently, satellites have been launched that were specifically designed for aerosol measurements. These newer sensors have the capability to observe aerosol properties over multiple wavelengths, polarizations, and scattering angles. In addition, advanced cloud screening techniques improve aerosol retrievals in close proximity to clouds. The recent suite of aerosol-dedicated satellite sensors include MODIS, MISR, and CERES. Each sensor features unique measurement capabilities for the global retrieval of aerosol optical properties.

Aboard the Terra and Aqua satellite platforms, MODIS measures radiance in 36 spectral channels in the visible, near infrared, and infrared parts of the spectrum. MODIS

aerosol retrievals employ separate algorithms over land and ocean, with greater accuracy for retrievals over ocean. Retrieved aerosol optical depths tend to be overestimated by 10-15% due to contamination of cirrus clouds. MODIS can also derive an aerosol fine-mode fraction, which is the fraction of small particles in terms of aerosol extinction. On a monthly basis, the MODIS fine-mode fraction agrees with AERONET retrievals over ocean to within 20% (Remer et al., 2005).

MISR aboard Terra measures upwelling shortwave radiances in 4 spectral bands (446, 558, 672, and 866 nm) and at 9 viewing angles in the forward and aft directions along the orbital path (Diner et al., 2002). Its wide range of along-track viewing angles allows for increased accuracy in aerosol retrievals over bright surfaces compared to mono-directional instruments. The accuracy of AOD measurements from both the MODIS and MISR sensors is about 0.05 globally, and slightly improved over dark water (Kahn, 2005, Remer et al., 2005).

Aboard Terra and Aqua, CERES observes broadband shortwave and longwave radiances at three channels. Observed radiances are converted to TOA flux using the Angular Distribution Models (ADM) as a function of sun angle, viewing angle, and scene type (Loeb et al., 2002). These retrievals of TOA flux under clear-sky conditions can be compared to the expected flux for an aerosol-free atmosphere to derive the aerosol direct effect. Such an approach requires ancillary measurements of AOD from other sensors, such as MODIS or MISR.

2.3 Measurement-based Estimates

Global estimates of aerosol direct effects from measurement-based techniques are most effectively achieved through satellite remote sensing. Although observations from ground-based networks and field campaigns may fill in missing data, satellite retrievals ultimately form the foundation for characterizing global aerosol properties.

Since aerosol measurements from satellites are typically limited to cloud-free conditions, previous satellite-based estimates focus on clear-sky DRE. To obtain aerosol

TABLE 2.1: Measurement-based estimates of annual average DRE [W m^{-2}] at the top-of-atmosphere and surface, as evaluated separately over ocean and land surfaces.

	Ocean		Land	
Products	TOA	SFC	TOA	SFC
MODIS (Remer and Kaufman, 2006)	-5.9	–	–	–
MODIS_A (Bellouin et al., 2005)	-6.4	-8.9	–	–
CERES_A (Loeb and Manalo-Smith, 2005)	-5.5	–	–	–
CERES_B (Loeb and Manalo-Smith, 2005)	-3.8	–	–	–
CERES_C (Zhang, 2005)	-5.3	–	–	–
MODIS_G (Yu, 2004)	-5.7	-10.0	-5.5	-13.5
MISR_G (Yu, 2004)	-6.5	-11.1	-4.9	-11.8
MO_GO (Yu, 2004)	-5.1	-8.8	-4.8	-11.6
MO_MI_GO (Yu, 2004)	-5.1	-8.7	-4.4	-10.6
POLDER (Boucher and Tanré, 2000)	-5.7	-7.7	–	–
Mean±StdDev	-5.5±0.7	-8.7±1.7	-4.9±0.4	-11.9±1.2

properties in the shortwave spectrum, satellite sensors often perform retrievals at mid-visible wavelengths, such as 550 nm. Given that aerosol retrievals from passive instruments commonly use different algorithms for ocean versus land, measurement-based estimates of DRE are separated accordingly.

Table 2.1 presents several satellite-based estimates of annual average DRE at the TOA and surface. Separate results are shown over ocean and land since passive instruments commonly use different aerosol retrieval algorithms for ocean versus land. The mean of all estimates yield an annual average DRE over ocean of -5.5±0.2 W m^{-2} at the TOA and -8.8±0.7 W m^{-2} at the surface (Yu et al., 2006). Over ocean, cooling at the surface is nearly 60% greater than cooling at the TOA, with the difference attributed to atmospheric absorption by aerosols.

Passive satellite sensors tend to have difficulty accurately retrieving aerosol measurements over bright and spatially heterogeneous land surfaces. Therefore, DRE estimates over land often rely on filling in missing satellite data with model simulations as well as satellite-model integrations. Averaged annually, measurement-based techniques estimate the clear-sky DRE over land surfaces at -4.9±0.3 W m^{-2} at the TOA

TABLE 2.2: Model-based estimates of annual average DRE [W m^{-2}] at the top-of-atmosphere and surface, as evaluated separately over ocean and land surfaces.

	Ocean		Land	
Products	TOA	SFC	TOA	SFC
GOCART (Chin et al., 2002)	-4.1	-6.9	-4.1	-9.7
SPRINTARS (Takemura and Nakajima, 2002)	-1.6	-2.7	-1.7	-5.1
GISS (Koch, 2005)	-3.5	-4.8	-2.8	-7.2
LMDZ-INCA (Balkanski and Schulz, 2007)	-4.7	-5.8	-4.3	-9.2
LMDZ-LOA (Reddy, 2005)	-2.3	-4.1	-2.0	-6.9
Mean±StdDev	-3.2±1.3	-4.9±1.6	-3.0±1.2	-7.6±1.9

and -11.7±0.7 W m^{-2} at the surface (Yu et al., 2006). Compared to DRE over ocean, terrestrial DRE estimates are more positive at the TOA and more negative at the surface, suggesting that aerosol absorption over land is stronger than that over oceans.

2.4 Model-based Estimates

Since the IPCC TAR, there have been significant advances in modelling aerosol direct effects. Most current global climate models (GCMs) have the capability to estimate aerosol direct radiative effects, with horizontal resolutions often finer than 2° and vertical resolutions of 20 levels or greater. Current global models include effects from most important anthropogenic and natural aerosol species. Some of the more complex models can even account for the evolution of particle size distributions throughout aerosol lifetimes. Internal and external mixing of aerosol components is another feature employed in most newer models (CCSP, 2009). Recent developments in modeling have led to significantly more physically realistic simulations of aerosol processes.

Table 2.2 displays several model-based estimates of annual average DRE. As with Table 2.1, results are shown over ocean and land, as well as at the top-of-atmosphere and at the surface. The ensemble of five GCMs, including GOCART, SPRINTARS,

GISS, LMDZ-INCA, and LMDZ-LOA, yield an annual average DRE over ocean of -3.2±0.6 W m^{-2} at the TOA and -4.9±0.8 W m^{-2} at the surface (Yu et al., 2006). Model-based estimates, although weaker than measurement-based estimates, give a surface cooling about 53% greater at the TOA than at the surface.

Since it currently remains challenging to estimate aerosol properties over land from passive measurements, DRE estimates over land generally rely heavily on model simulations. Model-based estimates of annual average DRE over land is -3.0±0.6 W m^{-2} at the TOA and -7.6±0.9 W m^{-2} at the surface (Yu et al., 2006). Table 2.2 reveals that model-based estimates of DRE over land are generally more positive than measurement-based estimates of DRE over land.

2.5 Reducing Uncertainties in Estimates

Averaged globally, measurement-based estimates of DRE are 55-80% larger than model-based estimates. On regional scales, the differences between measurements and models can be even greater. Such discrepancies likely result from uncertainties in observed and simulated aerosol optical depth, single scattering albedo, surface albedo, as well as differences in radiative transfer schemes (Yu et al., 2006).

Since MODIS-retrieved AOD tends to be overestimated due to cloud contamination, MODIS-based assessments likely result in comparable overestimates of aerosol DRE (Chand et al., 2012). As for model-based estimates, it is possible that complex aerosol processes (especially in the vicinity of clouds) are not realistically represented in models and could lead to biases in simulated estimates of aerosol direct effects.

Significant uncertainties exist in global estimates of DRE from both measurement-based and model-based techniques. The largest discrepancies generally occur in DRE estimates over land and in cloudy skies. Furthermore, anthropogenic aerosols are often difficult to isolate using current observational techniques. While models have the capability to simulate the radiative forcing from anthropogenic aerosols, large uncertainties remain since current estimates are poorly constrained by observations.

2.6 Remaining Questions

Most assessments of aerosol direct effects from passive satellite observations only consider aerosol direct effects under clear-sky conditions. Instrument limitations posed by passive sensors inhibit current measurement-based estimates of global DRE. Since the magnitude and sign of aerosol direct effects are highly dependent on clouds, it is critically essential that clouds are adequately represented in global DRE assessements.

Evaluating DRE over land and in cloudy skies requires characterization of the vertical cloud and aerosol distributions. This has proved challenging for both models and observations due to the large errors introduced by incorrect assumptions of three-dimensional cloud and aerosol fields. The lack of aerosol observations over cloudy-sky conditions ultimately hinder global assessments of aerosol direct effects. High-quality measurements of aerosol properties in poorly sampled regions are necessary to reduce uncertainties in current global estimates of DRE.

Chapter 3

Data and Methodology

3.1 Introduction

Previous studies have performed global assessments of aerosol direct effects using passive satellite sensors, including MODIS, MISR, and CERES. Although satellite observations offer global spatial coverage of aerosol measurements, passive sensors are often unable to retrieve aerosol properties over land and in the presence of clouds. In this study, we overcome these barriers using a combination of active and passive sensors from the A-Train satellite constellation. Collocated A-Train measurements can provide the necessary observational constraints to overcome limitations which have severely handicapped previous measurement-based assessments of DRE.

3.2 The A-Train Satellite Constellation

The A-Train (or Afternoon Train) is a constellation of five satellites which follow a sun-synchronous orbit at an altitude of 690 km. The satellites cross the equator within a few minutes of each other at around 1:30 am/pm local solar time. The benefit of formation flying is that a large number of observations may be collected at the same location and at the same time. The current satellites in the A-Train include Aura, CloudSat, CALIPSO, and Aqua, as shown in Figure 3.1, as well as GCOM-W1 (not pictured).

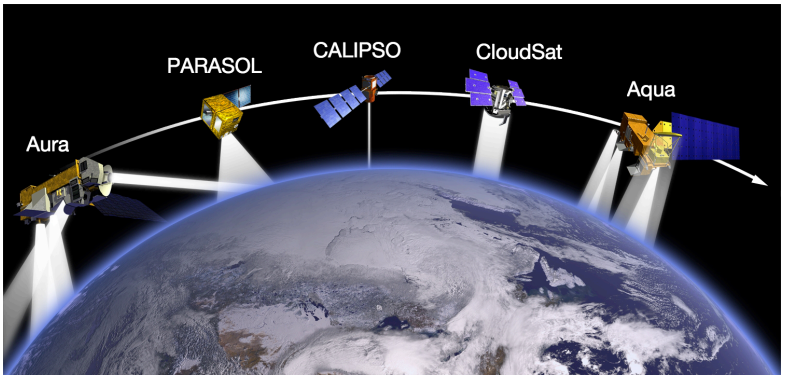

FIGURE 3.1: NASA's A-Train satellites monitor the global climate system using a suite of nearly simultaneous collocated measurements.

A-Train satellite observations are used to build high-resolution three-dimensional views of earth's atmosphere and surface. Each satellite features complementary sensors which together improve our scientific understanding of climate processes. Collectively, the sensors aboard the A-Train satellite constellation offer an unprecedented dataset for assessing the climate impact of aerosols. In this study, we assess aerosol direct effects using collocated observations from the CloudSat, CALIPSO, and Aqua platforms.

3.2.1 CloudSat

CloudSat has been actively monitoring cloud properties from space since its launch in April 2006. The main sensor aboard CloudSat is the Cloud Profiling Radar (CPR), a 94-GHz nadir-viewing radar that measures the returned backscattered energy, location, and altitude of clouds and precipitation. CloudSat was designed to profile clouds and their physical properties to improve the way in which clouds are parameterized in global models and, therefore, contribute to improved prediction of weather, climate, and cloud-climate feedbacks.

3.2.2 CALIPSO

The Cloud-Aerosol Lidar with Orthogonal Polarization (CALIPSO) was launched, along with CloudSat, from a single Delta II rocket at Vandenberg Air Force Base, California. A joint U.S. (NASA) and French (Centre National d'Etudes Spatiales/CNES) venture,

CALIPSO features an active dual-wavelength dual-polarization lidar used to probe the vertical structure of thin clouds and aerosols in the atmosphere. Lidar profiles from the Cloud-Aerosol Lidar with Orthogonal Polarization (CALIOP) instrument are complemented by infrared radiation measurements from the Imaging Infrared Radiometer (IIR). The CALIPSO satellite provides new insight into the role that clouds and atmospheric aerosols play in regulating weather, climate, and air quality.

3.2.3 Aqua

The Aqua satellite platform performs global measurements of land, ocean, and atmospheric properties. Data are collected from various sensors to allow scientists to assess global changes, identify their anthropogenic and natural causes, and improve model development for long-term forecasting. Aqua includes six sensors, including the Moderate Resolution Imaging Spectroradiometer (MODIS). MODIS scans the earth's surface at 36 spectral bands, providing valuable measurements of global surface and atmospheric properties. The Advanced Microwave Scanning Radiometer - Earth Observing System (AMSR-E), also aboard Aqua, measures terrestrial, oceanic, and atmospheric parameters, including sea ice concentration. Collectively, the instruments aboard the CloudSat, CALIPSO, and Aqua platforms measure the key variables necessary for assessing global aerosol radiative effects.

3.3 CloudSat's 2B-FLXHR-ERB Data Product

The 2B-FLXHR-ERB data product utilizes vertical distributions of liquid and ice cloud effective radii and water contents from CloudSat's Level-2 cloud water content product (2B-CWC). These observations are combined with temperature and humidity profiles from the European Centre for Medium-range Weather Forecasts (ECMWF) analyses as well as surface albedo and emissivity data from the International Geosphere-Biosphere Programme (IGBP) global land surface classification (Henderson et al., 2013). Collectively, these data initialize a broadband radiative flux model, known as BUGSrad, to compute vertical profiles of radiative fluxes and heating rates.

BUGSrad is a two-stream, adding-doubling solution to the radiative transfer equation introduced by Ritter and Geleyn (1992). The model assumes a plane-parallel atmosphere over the 1.4x1.8 km CloudSat field of view. Molecular absorption and scattering is computed using the correlated-k method of Fu and Liou (1992). The delta-Eddington approximation is applied over six shortwave (0-4 μm) bands and a constant-hemisphere approximation is applied over twelve longwave (>4 μm) bands. The bands are then weighted and combined into broadband estimates of shortwave and longwave fluxes. Finally, the algorithm computes the pressure derivative of net radiative flux to derive vertical heating rates.

$$\mathcal{H} = \frac{g}{C_p} \frac{\partial F^{net}}{\partial p} \tag{3.1}$$

The resulting fluxes and heating rates are output for each CloudSat footprint at a vertical resolution of 240 m, forming the 2B-FLXHR data product. The 2B-FLXHR-ERB data product used in the current study is the result of several improvements to the existing 2B-FLXHR algorithm (Henderson et al., 2013). L'Ecuyer et al. (2008) showed that thin clouds undetected by CloudSat may lead to significant errors in radiative flux estimates. By including coincident lidar observations from CALIPSO and radiance measurements from MODIS, a method was developed to improve constraints on cloud and aerosol properties in radiative flux calculations.

Furthermore, the radiative transfer model was modified to simulate solar position at all possible zenith angles to compute radiative fluxes for both daytime and nighttime satellite retrievals so that the resulting fluxes approximate diurnal averages. Future algorithm development plans include Atmospheric Infrared Sounder (AIRS) temperature and humidity sounding retrievals to reduce the dependence on ECMWF analyses. It is noted that the source of temperature and humidity information has a negligible impact on estimates of aerosol DRE since it is derived from flux differences.

The key steps in generating the new 2B-FLXHR-ERB data product are summarized in the flowchart illustrated in Figure 3.2. Cloud location is determined based on CloudSat's 2B-GEOPROF-LIDAR product. Cloud properties are obtained using a combination of CloudSat's 2B-CWC-RO, CloudSat's MODIS-based 2B-TAU, and CALIPSO's

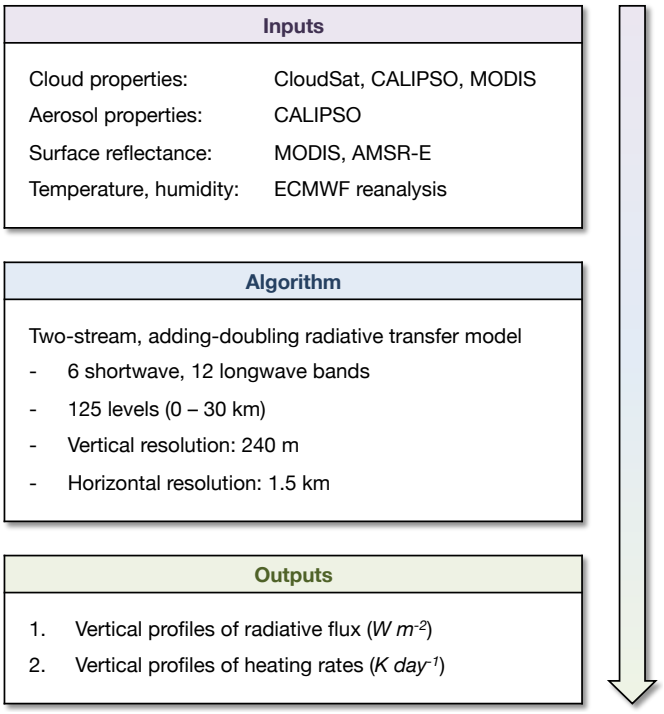

FIGURE 3.2: A flowchart of the 2B-FLXHR-ERB algorithm.

Version 3 products. Precipitation location and intensity are identified using CloudSat's 2C-PRECIP-COLUMN product, which retrieves cloud and rain liquid water contents and estimates the vertical extent of liquid precipitation in the column.

Aerosol optical depth is determined based on CALIPSO's Aerosol Layer product. CALIPSO's vertical feature mask (VFM) product is used to determine aerosol species type and vertical distribution. Aerosol optical properties, including single scattering albedo and asymmetry parameter, are retrieved for each aerosol layer using an approach similar to the Spectral Radiation-Transport Model for Aerosol Species (SPRINTARS) global transport model (Takemura and Nakajima, 2002). Retrieved aerosol properties from CALIPSO form critical observational inputs for the 2B-FLXHR-ERB algorithm.

The 2B-FLXHR-ERB algorithm computes upwelling and downwelling SW and LW radiative fluxes at 125 vertical levels. The uppermost level is at an altitude of about 25 km above mean sea level and is treated as the top-of-atmosphere. The lowest level is at the surface. The data product has a vertical resolution of 240 m and a horizontal

resolution of 1.5 km, as constrained by the maximum resolution provided by CloudSat observations.

3.4 Community Earth System Model (CESM)

Measurement-based assessments of DRE provide valuable observational constraints for global model simulations. In a first effort to use the 2B-FLXHR-ERB dataset to validate model performance, DRE estimates are compared against a widely-used global model, the Community Earth System Model (CESM). Improved accuracy in model simulations of DRE will lead to reduced uncertainties in global estimates of aerosol effects on future climate.

CESM is a fully-coupled general circulation model (GCM) that provides state-of-the-art computer representations of Earth's past, present, and future climate. Maintained by the Climate and Global Dynamics Division (CGD) at the National Center for Atmospheric Research (NCAR), CESM comprises five geophysical component models simultaneously simulating earth's atmosphere, ocean, land surface, sea ice, and land ice. All five models communicate using a central coupler component in a fully-coupled model environment. The coupling infrastructure of CESM provides the ability to use a single code base in a complete development cycle to optimize global simulations over various model configurations and resolutions (Worley and Craig, 2011).

This CESM simulation used in this study features an Atmospheric Model Intercomparison Project (AMIP) style run. In AMIP simulations, the atmospheric model is constrained by observed sea surface temperatures and sea ice concentrations based on climatology from 1979 to the present. The AMIP model configuration leverages the atmospheric model without the added complexity of ocean-atmosphere feedbacks in the climate system.

Physical atmospheric processes are represented using Version 5.1 of the Community Atmosphere Model (CAM5). This version of CAM offers several improvements over its predecessor, CAM4, including an enhanced treatment of stratus-radiation-turbulence interactions, shallow convection, and stratiform microphysics. The CAM5

simulation invokes the 3-mode prognostic Modal Aerosol Model (MAM) scheme and the Rapid Radiative Transfer Model (RRTMG) radiation scheme, which features a similar set of distinct radiation calculations as those employed in the 2B-FLXHR-ERB algorithm (Worley and Craig, 2011). Based on prescribed model parameters, monthly-averaged aerosol DRE at the top-of-atmosphere is simulated over a comparable time period from 2002 to 2006.

3.5 Methodology

The 2B-FLXHR-ERB dataset computes vertical profiles of radiative flux, but does not explicitly output aerosol DRE. To compute DRE, it is necessary to difference the net flux (downwelling minus upwelling) computed with aerosols present from an alternate net flux computed without aerosols present. Since this method employs a radiative transfer model to calculate radiative fluxes, conditions can be simulated for an aerosol-free atmosphere by setting all aerosol inputs to zero. The standard 2B-FLXHR-ERB algorithm has been configured to perform these calculations and include the results in the output so that aerosol DRE may be calculated. The 2B-FLXHR-ERB dataset comprises near-global (82°S to 82°N) observations of DRE profiles from July 2006 to April 2011.

In the 2B-FLXHR-ERB data product, fluxes are calculated over 12 solar zenith angles to simulate solar position throughout a 24-hour period. The use of artificial solar zenith angles allows radiative fluxes to be for all CloudSat profiles, including profiles during nighttime conditions. Such an approach is advantageous for studying Earth's radiation budget. To reduce data variability caused by the diurnal cycle of solar insolation, a 12-pixel moving average is performed over all profiles within the dataset. Applying this moving average to the 2B-FLXHR-ERB dataset maintains results consistent with diurnally-averaged radiative fluxes.

For quality control, profiles which include bad or missing input data are removed from the dataset. Data are screened based on the following criteria: bad surface bin, high uncertainty in cloud water content (CWC), missing CWC, missing 2B-Tau data product, missing CALIOP, missing MODIS-AUX, missing AMSR-AUX, or out-of-bounds

flux observations. The criteria are described in more detail in Table 14 of the CloudSat FLXHR-Lidar Data Product Documentation (Henderson and L'Ecuyer, 2011).

Data are available for every CloudSat overpass in which input fields satisfy quality control. The five-year dataset features observations from nearly every location on earth, including a wide range of environmental variability. Aerosol direct effects depend, to a large extent, on the environmental conditions in which aerosols reside in the atmosphere, including surface type (i.e. land and ocean) and sky conditions (i.e. clear-sky and cloudy-sky). To gain insight into the enviromental factors which influence aerosol direct effects, DRE observations are categorized based on surface type and sky conditions.

3.5.1 Classifying surface types

The magnitude and sign of aerosol direct effects are highly dependent on the reflectivity of the underlying surface. Bright surfaces serve to enhance atmospheric warming from absorbing aerosols, whereas dark surfaces serve to enhance cooling from scattering aerosols. As seen from space, oceans are uniformly dark in the visible spectrum. Conversely, land surfaces are often inhomogeneous and can be much more reflective, which can greatly alter the direct radiative effect exerted by aerosols.

Accurate assessment of aerosol direct effects requires knowledge of surface reflectance characteristics. The 2B-FLXHR-ERB algorithm accounts for land and ocean reflectance characteristics using surface albedo and emissivity data from the International Geosphere-Biosphere (IGBP) global surface classification. Global land cover classification is derived from a suite of observational MODIS products aboard the Terra and Aqua platforms. Data are synthesized to produce a high-quality annual global composite of 17 land cover types (Moody et al., 2005).

Surfaces are grouped into *land*, *ocean*, or *margin* categories. The combination of these three categories yields *global* coverage. For seasonal analyses, global surface maps are averaged over a seasonal time period. For annual analyses, global surface maps are averaged over a yearly time period. The seasonal land-ocean masks used in the current analysis are shown in Figure 3.3.

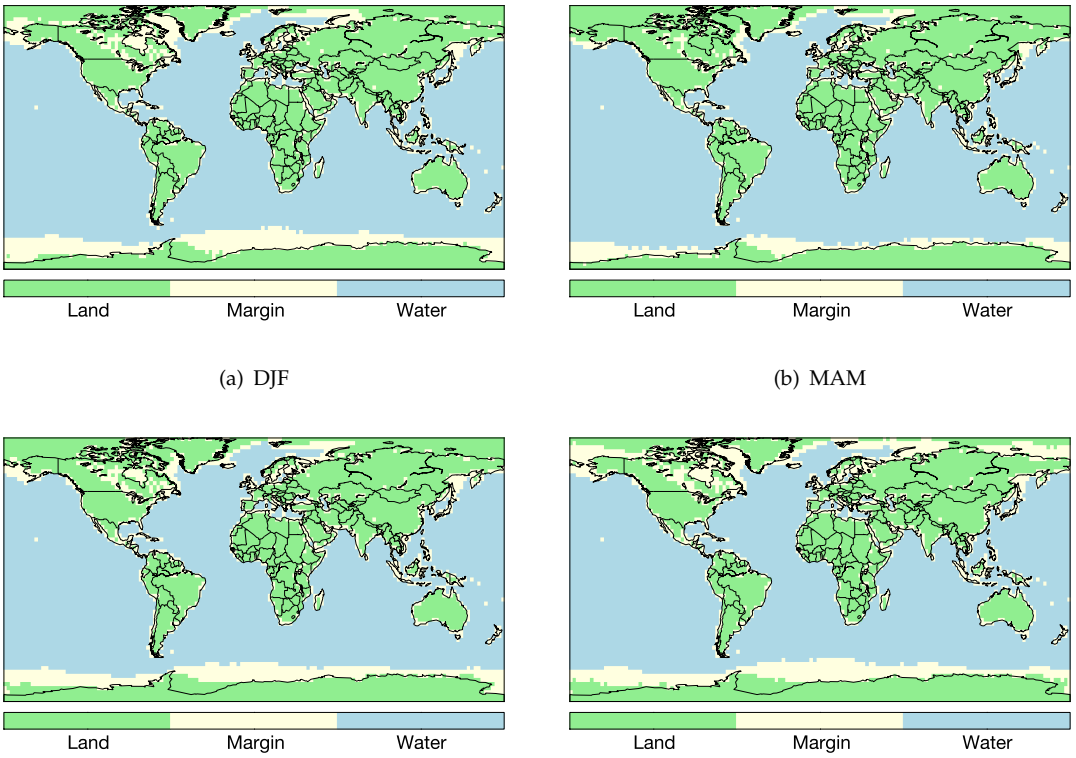

(a) DJF (b) MAM

(c) JJA (d) SON

FIGURE 3.3: Seasonal average land-ocean masks used in the 2B-FLXHR-ERB dataset are based on IGBP surface classifications.

In these maps, profiles which are not consistently (over 90%) land or ocean are labeled *margin*, as indicated by the yellow shading. These marginal surfaces include coastlines and seasonally-transient sea ice. Averaged annually, the surface of the earth is classified as 31% land, 52% ocean, and 17% margin. Due to the presence of marginal surfaces, the combined area of land and ocean is not representative of global coverage.

3.5.2 Classifying sky conditions

Aerosol direct effects also depend strongly on the presence of clouds. Cloud type, height, and location are all critical factors which may influence the radiative effect exerted by aerosols. Similar to a bright surface, a bright cloud enhances atmospheric

heating from absorbing aerosols. Alternatively, a bright cloud may nullify the cooling imposed otherwise by scattering aerosols. Therefore, knowledge of both cloud and aerosol fields is required for accurate assessment of aerosol direct effects.

Sky conditions are categorized as clear-sky or cloudy-sky. Clear-sky conditions are assessed if no clouds or precipitation is detected by either CloudSat or CALIPSO. Cloudy-sky conditions are assessed if either CloudSat or CALIPSO detects a cloud. Cloudy-sky conditions cover a wide range of cloud types, from optically thin to optically thick. Since cirrus clouds are often optically transparent to visible radiation, aerosol direct effects are similar to clear-sky conditions when cirrus clouds are present.

As a result, cloudy-sky conditions are further categorized by cloud type: *cirrus* or *other clouds*. Cirrus is identified if CALIPSO detects a single cloud layer above 440 mb. For all profiles in which clouds and/or precipitation is detected by CALIPSO or CloudSat, the scene is labeled as other clouds. A 12-pixel moving average is applied to all profiles in the dataset. If a profile is not consisently (over 80%) clear-sky, cloudy-sky (cirrus), or cloudy-sky (other clouds), it is labeled as *mixed-sky*.

Overall, the methodology of this study is designed to leverage aerosol measurements from a suite of satellite platforms. Improved measurements of aerosol optical properties provide valuable observational constraints for model simulations of aerosol direct effects. Whereas many previous studies have focused entirely on global estimates of DRE, this study also investigates regional variability. By discriminating DRE by surface and sky conditions, further insight may be gained into the role of aerosols in the climate system.

Chapter 4

Evaluating Global Observations

4.1 Introduction

This section presents estimates of global aerosol direct effects from the new 2B-FLXHR-ERB dataset in quantifying aerosol direct effects. The results are displayed in the form of global maps, seasonal plots, and tables of annual average values. All maps display binned averages of observed values over over 2.5°x2.5° bins. To improve the signal-to-noise ratio, we apply a Gaussian filter with a kernal standard deviation of 0.8. Later in this chapter, results will be shown for observed DRE as sorted by sky and surface conditions to highlight the dependence of aerosol effects on their environment.

4.2 Data Availability

The 2B-FLXHR-ERB dataset spans a five-year period, from July 2006 to April 2011, while covering the globe between 82°S and 82°N. The dataset yields a total of 730 million flux profiles from 19,935 CloudSat granules. Of this total, 98.6% of the granules satisfy quality control. DRE is computed only if CALIPSO detects aerosols within a given profile, which comprises 286 million profiles, or 39% of the total.

All profiles from the 2B-FLXHR-ERB dataset are well-sampled globally, as shown in Figure 4.1(a). The global sample density is mostly homogeneous with greatest coverage at the poles. The average sample density of all profiles over 2.5° bins is 74,400.

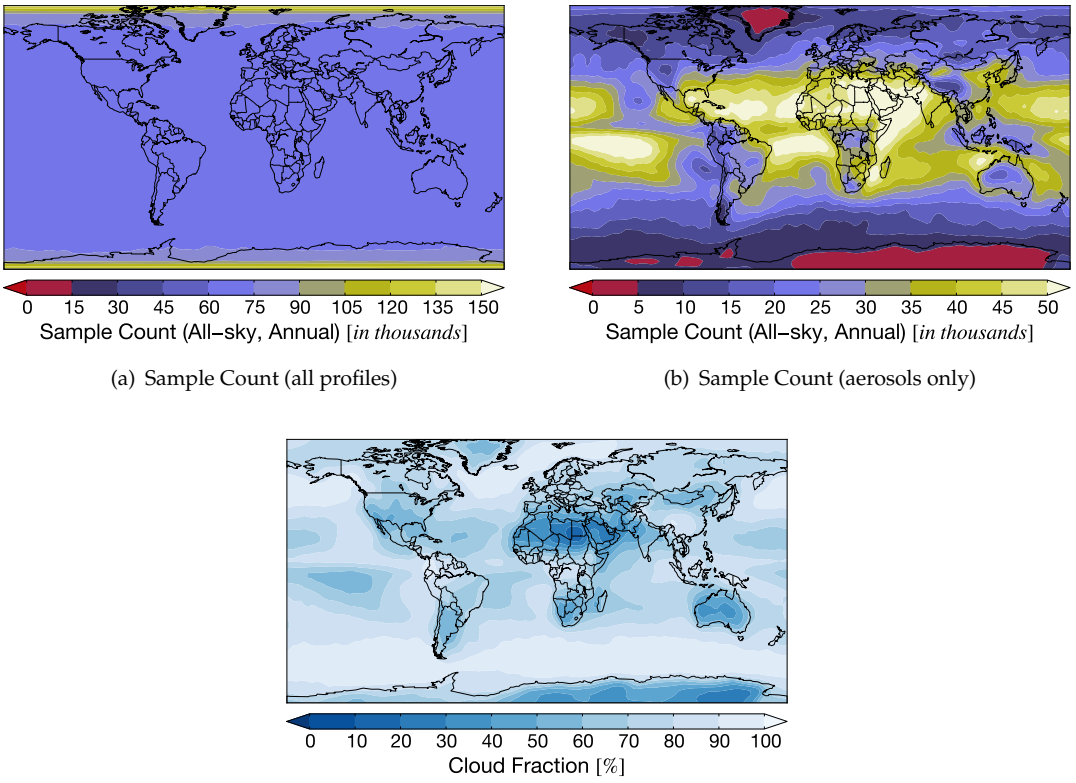

(a) Sample Count (all profiles)

(b) Sample Count (aerosols only)

(c) CloudSat/CALIPSO Total Cloud Fraction

FIGURE 4.1: Sample density maps of (a) all 2B-FLXHR-ERB profiles and (b) profiles in which CALIPSO detects aerosols, as influenced by (c) CloudSat/CALIPSO observed total cloud fraction.

After screening for aerosols, the sample coverage becomes more spatially heterogeneous. Figure 4.1(b) displays the global sample density for aerosol-detected profiles. The average sample density of aerosol-detected profiles is 24,900. Equatorial regions are generally better sampled, especially over predominantly cloud-free areas. Since CALIPSO cannot detect aerosols under optically thick clouds, the sample coverage for aerosol-detected profiles is similar to the global distribution of total cloud fraction in Figure 4.1(c). Based on five years of observations from CloudSat and CALIPSO, the average global cloud fraction of the dataset is 71%.

This study considers 2B-FLXHR-ERB observations from aerosol-detected profiles. After screening for aerosols, the least well-sampled regions include Greenland and Antarctica, where the sample density dips below 5,000 over in some areas. CALIPSO

does not detect aerosols as frequently in these locations; therefore, there are fewer satellite observations in which DRE may be computed. Similarly, there are relatively fewer aerosol observations over the southeast Pacific Ocean, central Africa, Himalayas, and Indonesia, resulting from the high frequency and coverage of clouds. Regional analyses of Greenland and Antarctica are excluded from this study due to limited data availability over these areas.

4.3 Global Distribution of All-sky DRE

The global distribution of observed aerosol direct effects provide a useful benchmark against which model estimates of aerosol effects may be evaluated. Figure 4.2 maps annual average all-sky DRE and the standard deviation of all-sky DRE at the top-of-atmosphere (TOA), in the atmospheric column (ATM), and at the surface (SFC). As noted in Chapter 3, aerosol atmospheric heating is defined as the difference between DRE at the top-of-atmosphere and surface. All values are shown in units of W m^{-2}.

The global distribution of annual average all-sky DRE at the TOA is displayed in Figure 4.2(a). DRE is negative globally, indicative of an overall cooling of the climate system due to the presence of aerosols. Whereas most regions exhibit negative DRE (cooler colors like blue), there are a few areas where DRE is positive (warmer colors like orange).

The largest negative DRE occurs over the Sahel and Middle East due to scattering from desert dust over dark ocean or vegetated land surfaces. DRE is also negative over heavily urbanized areas of India and China, mainly due to anthropogenic aerosol emissions. Over open ocean, DRE is slightly negative resulting from sea salt aerosol scattering sunlight over the dark ocean surface.

In other locations aerosols produce a warming effect. Over the bright Sahara, desert dust absorbs solar radiation resulting in positive DRE. Similarly, black carbon from biomass burning can produce a positive DRE when transported over bright snow-capped surfaces, such as the Rocky, Andes, and Himalaya Mountains. Off the coast of

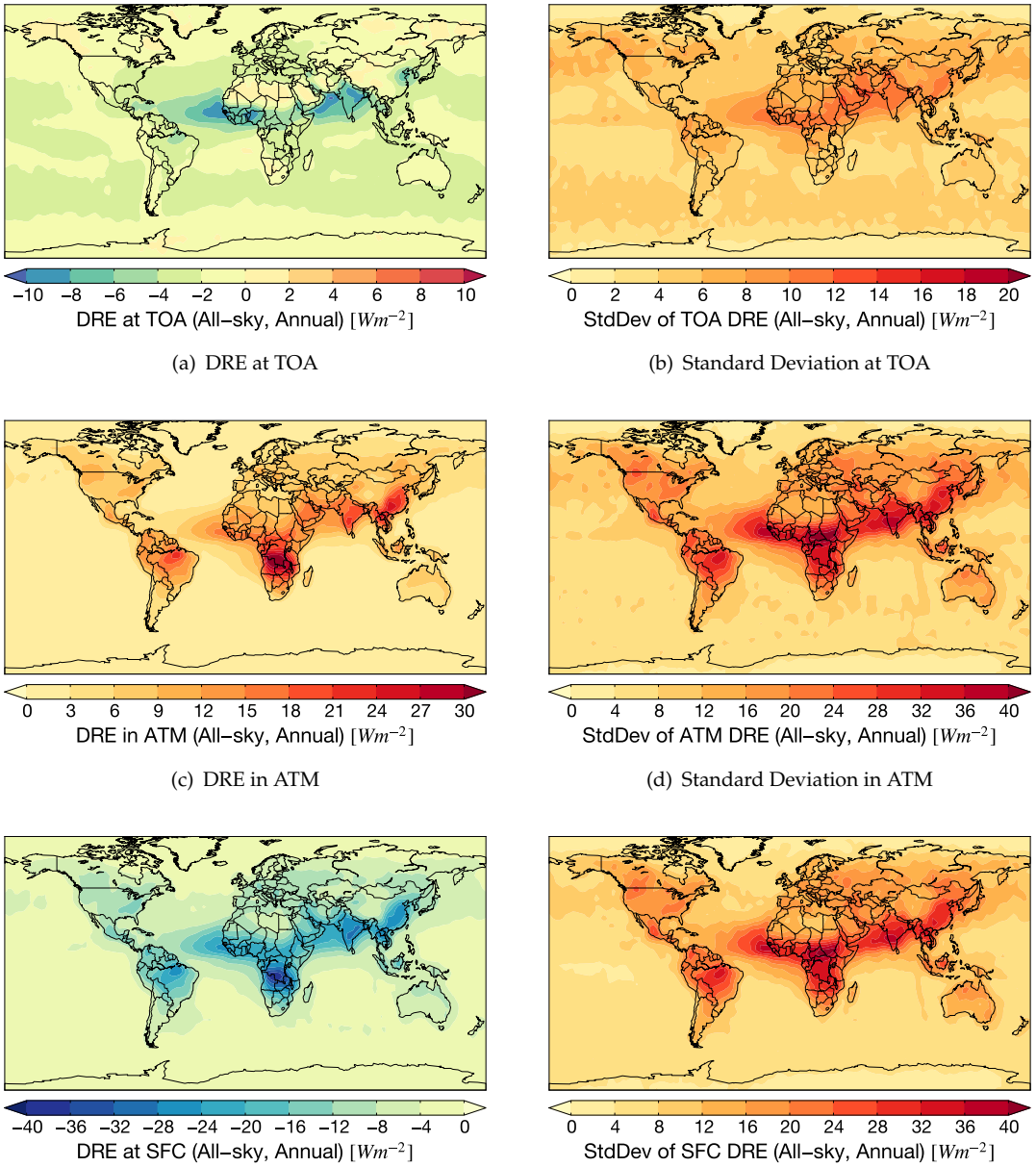

(a) DRE at TOA

(b) Standard Deviation at TOA

(c) DRE in ATM

(d) Standard Deviation in ATM

(e) DRE at SFC

(f) Standard Deviation at SFC

FIGURE 4.2: Observed DRE and standard deviation at the top-of-atmosphere (TOA), in the atmospheric column (ATM), and at the surface (SFC).

Angola in southern Africa, absorbing soot from biomass burning can produce a warming effect when located over the nearly ubiquitous bright marine stratocumulus clouds.

The countervailing warming from absorbing aerosols serves to offset the prevailing cooling from scattering aerosols. Over certain regions, including the Sahara, aerosol direct effects are strongly influenced by aerosol absorption. However, scattering aerosols predominate the global average, which results in a net cooling at the top of atmosphere.

Figure 4.2(b) maps the standard deviation of all-sky DRE at the TOA. Globally, the standard deviation at the TOA is 5.0 W m^{-2}. Over the Sahel and Middle East, values may exceed 10 W m^{-2}. These regions experience large seasonal variability in DRE due to monsoonal influence. Over subtropical oceans, where there is little seasonal variability in DRE, the standard deviation is generally less than 3 W m^{-2}.

Figure 4.2(b) displays the global distribution of all-sky aerosol absorption within the atmospheric column. Globally, the average DRE is positive, which suggests a warming of the atmosphere due to the presence of absorbing aerosols. Some regions are strongly positive (red), whereas other regions exert a negligible aerosol direct effect (yellow). Note that the atmospheric heating by aerosols is positive everywhere globally since aerosols do contribute to enhancing fluxes of visible radiation.

Regionally, there are several locations in which strong aerosol absorption is observed. India and southeastern China exhibit a positive DRE in excess of 20 W m^{-2} in some locations. Northern Brazil, which experiences seasonal wildfires, is also a region of isolated positive DRE. The most prominent region of aerosol absorption is central Africa, where aerosols exert a net effect of over 30 W m^{-2}.

Absorbing aerosols, including black carbon and mineral dust, are largely responsible for regions of aerosol atmospheric heating. Biomass burning is the primary emissions source in regions such as Brazil, southern Africa, and southeast Asia. Desert dust dominates aerosol absorption over northern Africa and the Middle East. Generally, source regions for absorbing aerosols are confined to land surfaces, which explains the high prevalence of positive DRE observed over land compared to ocean.

The standard deviation of aerosol atmospheric absorption is shown in Figure 4.2(d), with a global average of 12.5 W m^{-2}. Largest values are observed in central Africa,

where standard deviation can exceed 40 W m^{-2}. Southern India is another region which reveals large standard deviations of aerosol atmospheric absorption. The absorbing aerosols in these regions contribute to large variability in observed DRE values.

The global distribution of all-sky DRE observed at the surface is mapped in Figure 4.2(c). DRE is negative globally, indicative of a reduction in solar radiation at the surface due to the presence of aerosols. Both absorbing and scattering aerosols contribute to negative DRE at the surface. As a result, aerosols always contribute to reducing the amount of sunlight that reaches the surface.

Cooling at the surface is generally stronger in magnitude than the cooling at the top-of-atmosphere. Absorbing aerosols exert particularly strong cooling at the surface. Figure 4.2 also reveals that aerosol direct effects at the top-of-atmosphere are not necessarily present in the same geographic locations as direct effects at the surface.

There are several regions in which aerosol surface cooling predominates, including India, southeastern China, northern Brazil, and central Africa. In the Democratic Republic of Congo, aerosols exert a surface DRE as low as -30 W m^{-2}. Biomass burning aerosols are largely responsible for the strong aerosol cooling in central Africa. Surface DRE is greatest in magnitude in the tropics and relatively weaker at the poles since solar insolation is strongest near the equator compared to higher latitudes.

The standard deviation of all-sky DRE at the surface is mapped in Figure 4.2(f). Globally, the standard deviation is 11.2 W m^{-2}. Over central Africa, the standard deviation can be greater than 40 W m^{-2}. Biomass burning in this region contributes absorbing aerosols which reduce the amount of sunlight reaching the surface. Large standard deviation values are also observed over southern India. Over subtropical oceans, the standard deviation is generally less than 3 W m^{-2}.

4.4 DRE by Sky and Surface Conditions

The 2B-FLXHR-ERB dataset synthesizes observations from multiple complementary sensors that provide a comprehensive view of environmental conditions at a given location. Collocated observations from CloudSat, CALIPSO, and MODIS provide detailed information about observed cloud cover and cloud type. Retrievals from MODIS and AIRS monitor reflectivity properties at the Earth's surface. Knowledge of the sky and surface conditions provide additional observational constraints to offer valuable insights into the dependence of aerosol radiative effects on their environment.

As a result, observed DRE has been sorted by surface types (land, ocean, and global) and sky conditions (clear-sky, cloudy-sky: cirrus, cloudy-sky: other clouds, mixed-sky, and all-sky). Table 4.1 displays the fraction of total observations, as categorized by surface and sky conditions. The global, all-sky condition comprises 237 million radiative flux profiles, or 100% of total observations.

Some environmental conditions are better sampled than others. Globally, clear-sky observations comprise 38% of total observations, whereas cloudy-sky (cirrus) observations make up only 6%. Under the cloudy-sky (other) category, global observations are better represented at 28%. For scenes containing a mixture of clear-sky and cloudy-sky observations, the global percentage is also 28%. The least sampled category in Table 4.1 is cirrus-only observations over land, which is still sufficiently well-sampled at 4.5 million observations.

Figure 4.3 shows global maps of annual average DRE at TOA, as sorted by sky conditions. As shown in Figure 4.3, the presence of clouds can alter the effects of aerosols. Classification of DRE by sky conditions lends further insight into the environmental conditions that influence the magnitude and sign of aerosol direct effects.

In Figure 4.3(a), the most negative clear-sky DRE exists over western Africa, India, and China. In some localized areas, annual average clear-sky DRE exceeds -10 W m^{-2}. There are few locations where clear-sky DRE is positive, such as the bright Sahara, Arabian, Namib, and Atacama deserts. Positive values of DRE are generally no greater than 1 W m^{-2} in these locations.

TABLE 4.1: The fraction of 2B-FLXHR-ERB profiles observed within each category [%], in which the global, all-sky total is 237 million profiles.

	Clear-sky	Cloudy-sky (cirrus)	Cloudy-sky (other)	Mixed-sky	All-sky
Land	14	2	9	6	31
Ocean	24	4	19	22	69
Global	38	6	28	28	100

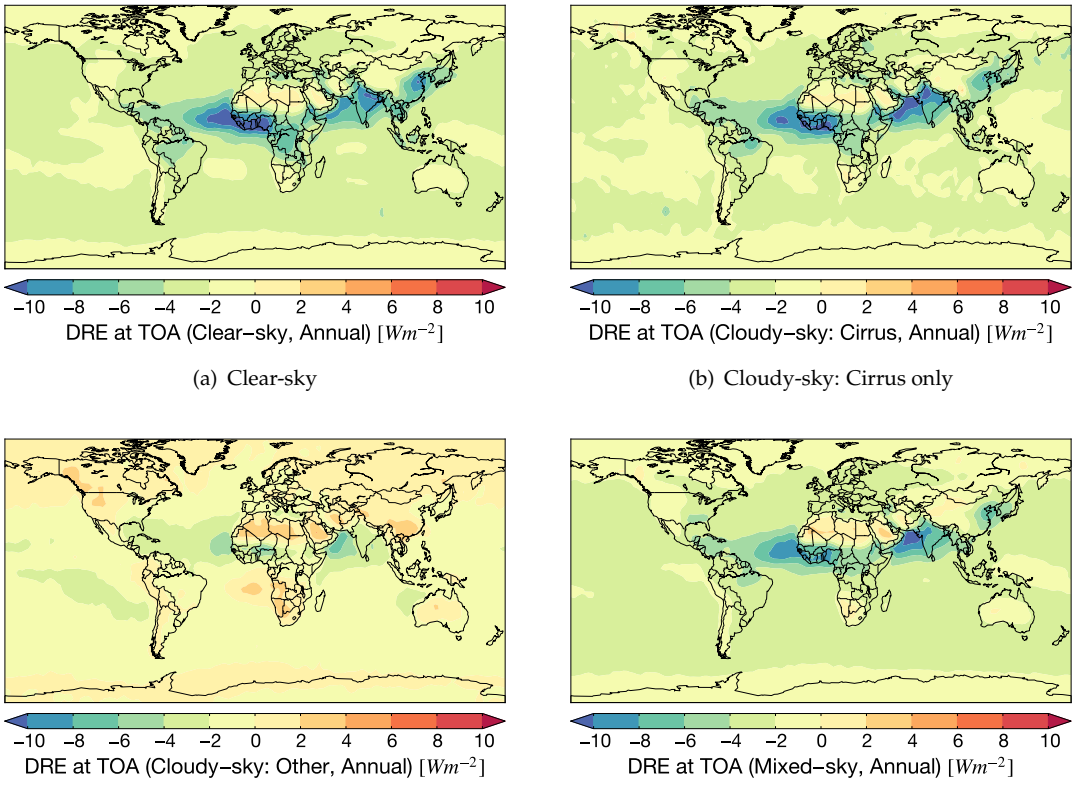

(a) Clear-sky

(b) Cloudy-sky: Cirrus only

(c) Cloudy-sky: Other Clouds

(d) Mixed-sky

FIGURE 4.3: Observed annual average DRE at TOA, as sorted by sky conditions.

There are strong similarities between Figure 4.3(a) and Figure 4.3(b). The global distribution of clear-sky DRE is nearly identical to the global distribution of cloudy-sky DRE when only cirrus are considered. Since cirrus clouds are optically thin, the presence of cirrus does not substantially alter aerosol direct effects compared to clear-sky conditions. Table 4.1 indicates that there are 6.5 times more clear-sky observations than cirrus-only observations. For this reason, Figure 4.3(b) exhibits noticeably more

regional noise than Figure 4.3(a).

In cloudy skies, positive DRE is observed over source regions of biomass burning or mineral dust aerosols, as shown in Figure 4.3(c). Isolated pockets of aerosol cooling exist over the Sahel and India. However, there are fewer instances of negative DRE overall compared to clear-sky observations. Weak aerosol cooling is evident over global oceans. Concentrations of scattering aerosols over optically-thin low clouds are primarily responsible for observations of negative DRE under cloudy-sky conditions.

Observations that are neither entirely clear-sky nor cloudy-sky are labeled mixed-sky. Figure 4.3(d) shows that annual average mixed-sky DRE is most negative over western Africa, India, and China. Positive mixed-sky DRE exists over northern Africa. Overall, the maps from Figure 4.3 demonstrate that DRE depends strongly on surface and sky conditions.

4.5 Seasonal Variability in DRE

4.5.1 Seasonal Maps of Observed DRE

The previous section summarized DRE as annual averages. However, aerosol sources exhibit strong seasonal variability resulting in associated variations in direct effects. Figure 4.4 documents observed variability in all-sky DRE over four seasonal periods: December-January-February (DJF), March-April-May (MAM), June-July-August (JJA), and September-October-November (SON).

In DJF, the presence of scattering aerosols produces isolated areas of cooling over the Sahel, northern India, and eastern China. There is slight cooling over the global oceans (most notably over the Southern Ocean) due to sea salt aerosols. Slight aerosol warming exists over Antactica, which receives solar radiation during this time of year. Furthermore, aerosol warming is evident over the northern United States where snow cover produces a highly reflective surface.

The aeolean transport of mineral dust over the Sahara and Arabian peninsula intensifies during MAM. As a result, there is stronger cooling over the Sahel and India.

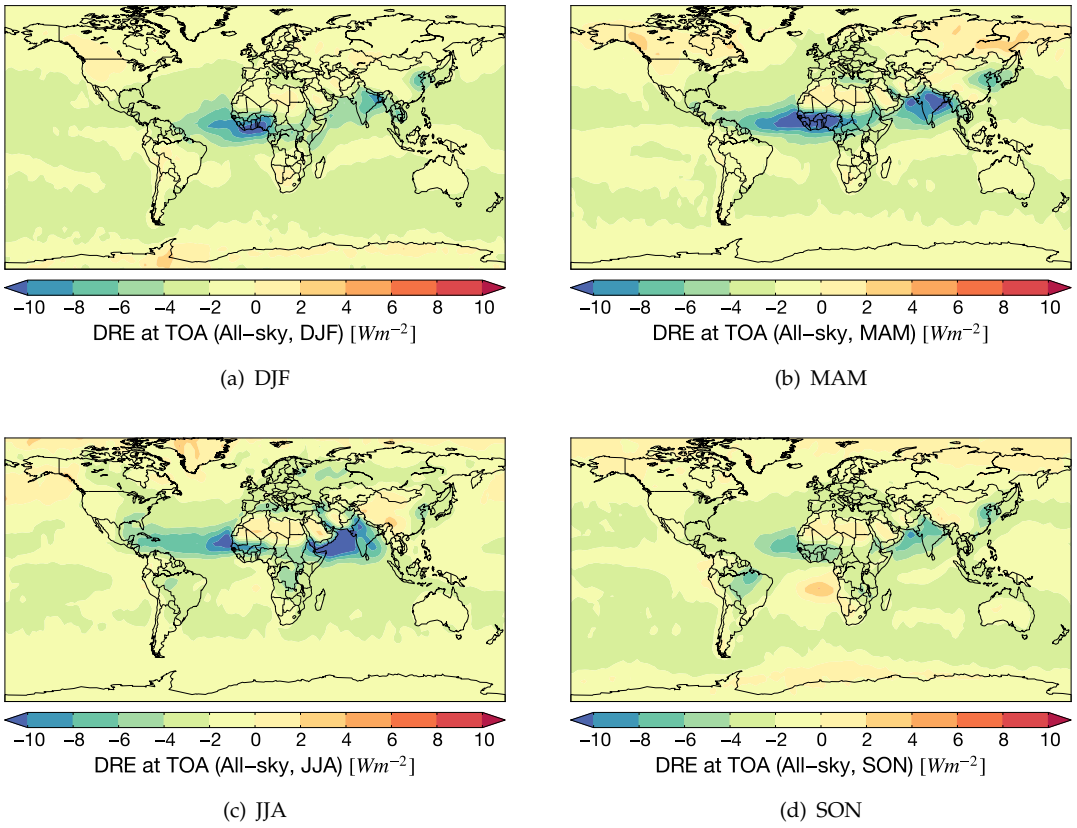

FIGURE 4.4: Seasonally-averaged maps of observed all-sky DRE at TOA.

Aerosol cooling extends over the equatorial Atlantic Ocean due to the long-range transport of Saharan dust. Aerosol warming is noted over northern Canada and Siberia, presumably resulting from biomass burning emissions over snow-covered terrain.

The Intertropical Convergence Zone (ITCZ) advances to its northernmost extent during JJA. Consequently, Saharan dust transport over the subtropics produces aerosol cooling over the dark Atlantic Ocean and aerosol warming over the bright Saharan desert. Monsoonal winds transport mineral dust over the Arabian Sea, which experiences its maximum aerosol cooling during JJA. Long sunlight hours coupled with low sun angles result in aerosol warming over Greenland and Arctic sea ice.

During SON, there is notably less aerosol cooling over western Africa and southern Asia as mineral dust transport subsides. Biomass burning in South America and southern Africa peak during this time. Aerosol cooling is also evident over northern Brazil

due to biomass burning. Off the coast of Angola, there is aerosol warming over a region where soot aerosols are transported over marine stratocumulus clouds. East Asia experiences isolated aerosol cooling resulting from anthropogenic emissions of scattering aerosols, such as sulfate.

Overall, large seasonal variability exists in observations of aerosol DRE, as illustrated in Figures 4.4 and 4.5. The 2B-FLXHR-ERB dataset reveals that aerosol direct effects are not only spatially heterogeneous, but temporally heterogeneous as well. Mineral dust and biomass burning emissions near the equator are largely influenced by the ITCZ, which exhibits a pronounced seasonal cycle. Therefore, a complete investigation of aerosol direct effects requires a thorough examination of interannual variability.

4.5.2 Seasonal Cycles in Observed DRE

Figure 4.5 summarizes monthly-averaged global DRE, in which values are computed as sine-weighted averages of global DRE. Subplots of *clear-sky*, *cloudy-sky (cirrus)*, *cloudy-sky (other)*, *mixed-sky*, and *all-sky* conditions are presented separately for comparison. Monthly values are plotted for aerosol atmospheric heating (red), DRE at the top-of-atmosphere (blue), and DRE at the surface (green).

Atmospheric heating by aerosols is positive for all months and all sky conditions. Aerosol direct effects peak during the JJA season due to an increased production of absorbing mineral dust and biomass burning aerosols during these months. Aerosol atmospheric heating is strongest under cloudy-sky conditions, with a maximum value of 7.0 W m^{-2} during July. Minimum values typically occur during the DJF season.

Surface DRE remains negative throughout the year under all sky conditions. Similar to aerosol atmospheric heating, surface DRE is strongest during the JJA season. Monthly-averaged values range between 5.0 and 8.0 W m^{-2} under all conditions. The minimum monthly value of surface DRE is -8.6 W m^{-2}, observed under mixed-sky conditions during July.

Globally, DRE at the top-of-atmosphere is negative under all sky conditions and remains nearly constant throughout the year. Overall, values are smaller in magnitude than at the surface or within the atmospheric column. Under clear-sky, cirrus-only,

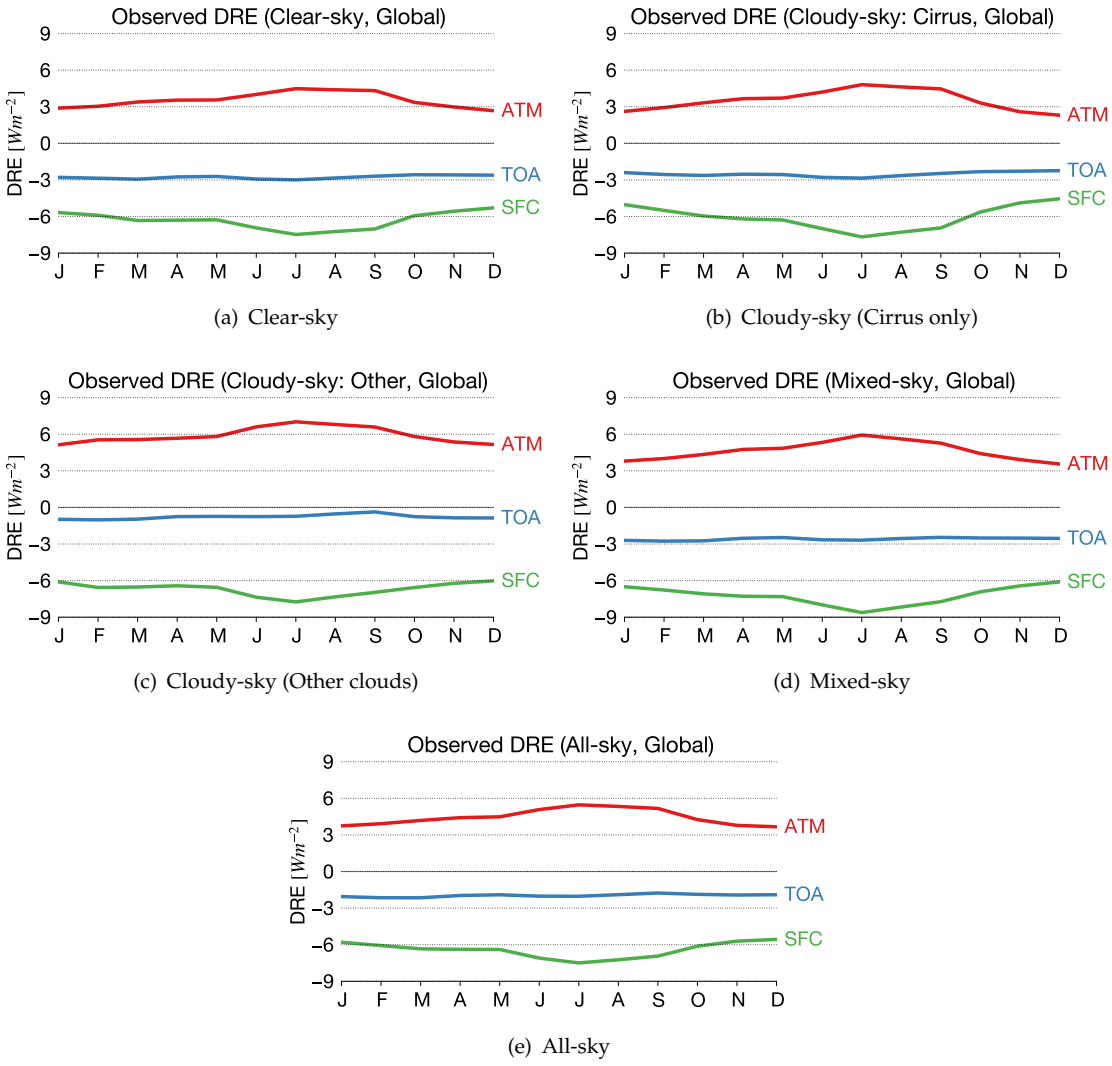

(a) Clear-sky

(b) Cloudy-sky (Cirrus only)

(c) Cloudy-sky (Other clouds)

(d) Mixed-sky

(e) All-sky

FIGURE 4.5: Seasonal cycle of observed aerosol atmospheric heating (red), top-of-atmosphere DRE (blue), and surface DRE (green).

and mixed-sky conditions, DRE at the top-of-atmosphere ranges between -2.2 and -3.0 W m^{-2}. However, values range between -0.3 and -1.0 W m^{-2} under cloudy skies. Thick clouds, not including cirrus, serve to suppress DRE at the top-of-atmosphere, which promotes a net warming effect on the climate system.

Overall, Figure 4.5 complements Figure 4.4 in describing the seasonal variability in aerosol direct effects. Globally, all monthly values of DRE are negative at the top-of-atmosphere and surface and aerosol atmospheric heating is positive throughout the year. DRE at the surface and in the atmospheric column reaches its greatest magnitude

during the JJA season, largely due to the increased production of absorbing mineral dust and biomass burning aerosols. Global DRE at the top-of-atmosphere, however, remains relatively constant throughout the year.

4.6 Global Estimates of Aerosol Direct Effects

4.6.1 Previous Estimates

Before presenting annually-averaged global estimates of DRE from the 2B-FLXHR-ERB dataset, it is useful to review current estimates published in the literature for context. Referencing the studies of Yu et al. (2006) and Loeb and Manalo-Smith (2005), the IPCC AR4 reports DRE estimates under two conditions: clear-sky ocean and all-sky ocean. Results from these studies are displayed in Table 4.2.

Yu et al. (2006) summarize a global mean, diurnally-averaged clear-sky DRE from various observational methods using satellite sensors including MODIS, CERES, MISR, and POLDER. The reported clear-sky ocean value of -5.5 $\pm$ 0.7 W m^{-2} is considerably stronger than the 2B-FLXHR-ERB value of -2.9 W m^{-2}. However, the value reported by Yu et al. (2006) is likely exaggerated due to subpixel cloud contamination from passive observations with large spatial footprints (Chand et al., 2012).

Loeb and Manalo-Smith (2005) use MODIS and CERES retrievals to convert clear-sky ocean DRE to all-sky ocean DRE. This technique assumes no contribution to DRE from cloudy regions, which is shown to impact global DRE estimates. Loeb and Manalo-Smith (2005) reports an all-sky ocean DRE of -1.6 to -1.8 W m^{-2}, which is more consistent with the 2B-FLXHR-ERB estimate of -2.1 W m^{-2}.

The results published in the IPCC AR4 represent the current state of knowledge on aerosol direct effects. Observational estimates of DRE are reported for clear-sky ocean and all-sky ocean conditions. No studies referenced in the report directly performed observational estimates of DRE in the presence of clouds. In addition, there are no global observational estimates of DRE published in the IPCC AR4.

TABLE 4.2: Previous satellite-based estimates of annual average DRE [W m^{-2}], as sorted by sky and surface conditions.

	Clear-sky	Cloudy-sky (cirrus)	Cloudy-sky (other)	Mixed-sky	All-sky
Land	—	—	—	—	—
Ocean	-5.5 $\pm$ 0.7$^{\alpha}$	—	—	—	-1.6 to -1.8$^{\beta}$
Global	—	—	—	—	—

α: Yu et al., 2006
β: Manalo-Smith, 2005

4.6.2 2B-FLXHR-ERB Estimates

Compared to previous assessments of aerosol DRE, the 2B-FLXHR-ERB dataset offers a more comprehensive view of aerosol direct effects. The multi-sensor approach sorts aerosol DRE among sky and surface conditions, which had never been performed previously. Since aerosol direct effects are highly dependent on the environment in which aerosols reside, it is critically important to consider surface and sky conditions to more fully understand the radiative impacts of aerosols on the climate system.

Table 4.3 summarizes global annual average DRE at the TOA. Values correspond to the sine-weighted averages of the global maps shown in Figure 4.3. The corresponding standard deviations of observed values are shown in parentheses. These observational results are sorted by sky conditions and surface types to be consistent with Table 4.2.

Note the similar values in clear-sky DRE over land (-2.7 W m^{-2}) and over ocean (-2.7 W m^{-2}). Averaged globally, aerosol cooling is comparable over land and ocean despite significantly greater aerosol emissions from terrestrial sources. The variability of clear-sky DRE observations is greater over land than over ocean, as evidenced by the standard deviation in observed values. Since clear-sky DRE values are identical over land and ocean, the global estimate of clear-sky DRE is also -2.7 W m^{-2}.

As expected, aerosol DRE in cirrus-only skies are similar to those observed in clear skies. Cirrus clouds reduce the magnitude of aerosol direct effects, on average, by about 10%. Cloudy-sky values over land (-2.5 W m^{-2}) and over ocean (-2.4 W m^{-2}) are comparable and similar to clear-sky values. The global estimate of DRE under cirrus-only skies is -2.5 W m^{-2}.

TABLE 4.3: 2B-FLXHR-ERB estimates of annual average DRE [W m^{-2}], as sorted by sky and surface conditions, for profiles in which CALIPSO detects aerosol. The standard deviations of observed values are shown in parentheses.

	Clear-sky	Cloudy-sky (cirrus)	Cloudy-sky (other)	Mixed-sky	All-sky
Land	-2.7 (7.4)	-2.5 (8.1)	0.3 (9.0)	-2.0 (8.4)	-1.7 (8.2)
Ocean	-2.7 (4.5)	-2.4 (4.9)	-1.1 (7.4)	-3.8 (4.5)	-2.1 (5.6)
Global	-2.7 (5.4)	-2.5 (5.8)	-0.7 (7.3)	-2.6 (5.3)	-2.0 (6.0)

Annual average DRE under cloudy skies is 0.3 W m^{-2} over land and -1.1 W m^{-2} over ocean. The positive DRE observed over land is largely a result of absorbing aerosols transported over bright clouds. Regions experiencing positive DRE are predominantly over land, as shown in Figure 4.3(b). Negative cloudy-sky DRE over ocean result from mineral dust advected over optically-thin low clouds in the North Atlantic. It is noted that there are large uncertainties with observations off the coast of West Africa due to the possible misclassification of dust aerosols with clouds.

Under mixed skies, results reflect a combination of clear-sky and cloudy-sky values. Annual average mixed-sky DRE is -2.0 W m^{-2} over land and -3.8 W m^{-2} over ocean. The mixed-sky ocean estimate includes a significant number of mostly clear observations, especially off the coast of West Africa, which explains its large magnitude relative to the clear-sky ocean estimate. The global mixed-sky DRE estimate is -2.6 W m^{-2}.

All-sky results have contributions from both clear-sky and cloudy-sky observations. All-sky DRE is -1.7 W m^{-2} over land and -2.1 W m^{-2} over ocean. Despite stronger aerosol direct effects over ocean, there is a larger standard deviation in observed values over land. Globally, we observe an annual average all-sky DRE of -2.0 W m^{-2} with a standard deviation of 6.0 W m^{-2}.

To assess the uncertainties in CALIPSO aerosol products, Henderson et al. (2013) conducted several sensitivity studies with the 2B-FLXHR-ERB data product: (a) CALIPSO AOD retrievals are perturbed by a factor of 2, based on results in Kittaka et al. (2011), (b) all non-marine aerosols are changed to smoke, (c) all non-marine aerosols are changed to dust, and (d) all smoke aerosols are changed to dust. These four cases represent extreme scenarios to provide an upper bound on the potential error in simulated fluxes.

TABLE 4.4: 2B-FLXHR-ERB estimates of annual average DRE [W m^{-2}], as sorted by sky and surface conditions, for all profiles. The standard deviations of observed values are shown in parentheses.

	Clear-sky	Cloudy-sky (cirrus)	Cloudy-sky (other)	Mixed-sky	All-sky
Land	-2.1 (4.4)	-1.9 (6.2)	0.1 (3.8)	-1.4 (5.5)	-0.9 (4.4)
Ocean	-2.4 (4.4)	-2.1 (4.7)	-0.4 (3.9)	-2.5 (4.3)	-1.2 (4.3)
Global	-2.3 (4.4)	-2.0 (5.1)	-0.3 (3.4)	-2.1 (4.5)	-1.1 (4.0)

Collectively, these uncertainties suggest an error of ± 0.6 W m^{-2} in the annually-averaged global all-sky DRE estimate.

For completeness, Table 4.4 displays annual average DRE from the 2B-FLXHR-ERB dataset using an alternate approach that includes all profiles for which CALIPSO detects no aerosols. Since it is not possible to separate scenes where CALIPSO simply misses aerosols due to detection issues from those that legitimately contain no radiatively important aerosols, the true global direct effect likely lies between the results presented in Tables 4.3 and 4.4. DRE estimates evaluated in this way are smaller than estimates shown in the previous table since profiles in which CALIPSO does not detect aerosols contribute 0 W m^{-2} to the overall mean.

Clear-sky DRE over land (-2.1 W m^{-2}) and over ocean (-2.4 W m^{-2}) are slightly weaker than estimates for aerosol-dectected observations. However, the standard deviations do not differ over land and ocean, suggesting consistent variability between the two surfaces. The global estimate of clear-sky DRE is -2.3 W m^{-2} with a standard deviation of 4.4 W m^{-2}.

Cloudy-sky DRE is 0.1 W m^{-2} over land and -0.4 W m^{-2} over ocean. These values are considerably more neutral than those observed for aerosol-detected observations. Furthermore, there is reduced variability in observed DRE. The standard deviation over land (3.8 W m^{-2}) and ocean (3.9 W m^{-2}) is considerably lower for all profiles since most cloudy-sky observations do not contain aerosols. The global cloudy-sky DRE estimate is -0.3 W m^{-2}.

Mixed-sky DRE is stronger over ocean (-2.5 W m^{-2}) than over land (-1.4 W m^{-2}). The mixed-sky estimate over ocean is 1.3 W m^{-2} less than for aerosol-detected observations, suggesting a significant contribution of 0 W m^{-2} observations from aerosol-free profiles. However, the standard deviation remains similar for mixed-sky DRE over ocean. Averaged globally, mixed-sky DRE is -2.1 W m^{-2}.

Annual average all-sky DRE is -0.9 W m^{-2} over land and -1.2 W m^{-2} over ocean, which are significantly weaker than observed DRE when only aerosol-detected profiles are considered. The global all-sky DRE is -1.1 W m^{-2} with a standard deviation of 4.0 W m^{-2}. Therefore, annual average all-sky DRE is reduced by 0.9 W m^{-2} when including all profiles in the 2B-FLXHR-ERB dataset.

Overall, there are notable differences in values depending on whether or not non-aerosol profiles are included in the analysis. Due to the complexity of aerosol radiative interactions, a realistic estimate of global aerosol DRE is likely from a combination of values from both tables. Further discussion of the all-profile approach is provided in Appendix A.

Chapter 5

Evaluating Global Simulations

5.1 Introduction

The past decade has brought about a new wave of aerosol modeling capabilities. Many general circulation models (GCMs) are now able to simulate a comprehensive suite of atmospheric aerosols, including sea salt, mineral dust, sulfate, black carbon, and organic carbon. GCMs, which account for both natural and anthropogenic aerosols, can simulate aerosol emissions, precursor emissions, chemical transformation, atmospheric transport, and removal processes. The most sophisticated models can even simulate the hygroscopic growth of aerosols, a process in which ambient water vapor condenses on aerosols to increase particle size (CCSP, 2009).

Climate models greatly facilitate global assessments of aerosol direct effects. Models can easily, and uninvasively, test the environmental response to prescribed initial conditions, which are commonly constrained by in-situ measurements and satellite observations. This study compares results from a GCM simulation with observations from the 2B-FLXHR-ERB dataset in an effort to evaluate the representation of aerosol direct effects in models. Improved accuracy in DRE simulations can contribute to reduced uncertainties in global estimates of aerosol direct effects.

5.2 Community Earth System Model (CESM)

The Community Earth System Model (CESM) is a fully-coupled GCM that generates state-of-the-art computer representations of Earth's past, present, and future climate. This study features an Atmospheric Model Intercomparison Project (AMIP) style simulation of the CESM, which constrains sea surface temperature and sea ice to climatological values from 1979 to the present. All CESM model output analyzed in this study was supplied courtesy of Jen Kay at NCAR via personal communication.

Atmospheric dynamics are simulated using Version 5.1 of the Community Atmosphere Model (CAM5.1). The CAM5 simulation invokes the 3-mode prognostic Modal Aerosol Model (MAM) scheme and the Rapid Radiative Transfer Model (RRTMG) radiation scheme, which features a similar set of distinct radiation calculations as the 2B-FLXHR-ERB algorithm for all-sky, cloud-free, and aerosol-free conditions (Worley and Craig, 2011). Based on prescribed model parameters, monthly-averaged aerosol direct effects at the top-of-atmosphere are simulated from 2002 to 2006. CESM model simulations are output at 1.0°x1.25° horizontal resolution.

5.3 Global Estimates

The modeled global all-sky DRE estimate (-1.7 W m^{-2}) is similar to the observed global all-sky estimate (-2.0 W m^{-2}). All-sky DRE over ocean is identical for both simulations and observations. All-sky DRE over land is -0.5 W m^{-2} from CESM simualations and -1.7 W m^{-2} from 2B-FLXHR-ERB observations. The largest discrepancies between model and observations occur in the DRE estimates over land.

Table 5.1 shows the simulated annual average global estimates of DRE. Similar to observational results from Chapter 4, DRE values are sorted by sky and surface conditions. Global estimates of clear-sky DRE from CESM are comparable to 2B-FLXHR-ERB observations. The simulated clear-sky DRE estimate is -3.3 W m^{-2}, which is 0.6 W m^{-2} stronger than the observed clear-sky DRE estimate of -2.7 W m^{-2}. Whereas CESM simulates a 1.8 W m^{-2} difference between clear-sky DRE over land and ocean, 2B-FLXHR-ERB observations report no difference between these two values.

TABLE 5.1: CESM estimates of annual average DRE [W m^{-2}], as sorted by sky and surface conditions.

	Clear-sky	Cloudy-sky	All-sky
Land	-2.0	1.0	-0.5
Ocean	-3.8	-0.9	-2.1
Global	-3.3	-0.4	-1.7

Simulations of cloudy-sky DRE tend to agree best with 2B-FLXHR-ERB observations of DRE under optically thick clouds. In both simulations and observations, cloudy-sky DRE is positive over land and negative over ocean. The global cloudy-sky DRE estimate is in agreement between CESM (-0.4 W m^{-2}) and 2B-FLXHR-ERB (-0.7 W m^{-2}).

Overall, global results are in good agreement between the CESM model and 2B-FLXHR-ERB observations. However, there are regional discrepancies which become increasingly more apparent once DRE is sorted by surface and sky conditions. Clouds present a significant source of discrepancy between simulation and observations. Since clouds are such a pervasive feature in the atmosphere, these differences become magnified in global evaluations of aerosol direct effects.

5.4 Seasonal Variability in DRE

5.4.1 Seasonal Maps of Modeled DRE

CESM is capable of simulating global distributions of DRE on interannual timescales. The seasonal variability of DRE from CESM is compared with observations from the 2B-FLXHR-ERB dataset. Figure 5.1 maps the seasonally-averaged all-sky DRE over DJF, MAM, JJA, and SON. Results are displayed in a four-panel plot to be consistent with 2B-FLXHR-ERB observations shown in Figure 4.4.

The most dominant source of aerosol scattering during DJF is from marine sea salt. Over oceanic subtropical high pressure regions there exist areas of negative DRE. The direct effect is nearly negligible at high latitudes. Positive DRE is found over isolated locations in the Sahara, where absorbing mineral dust aerosols are present.

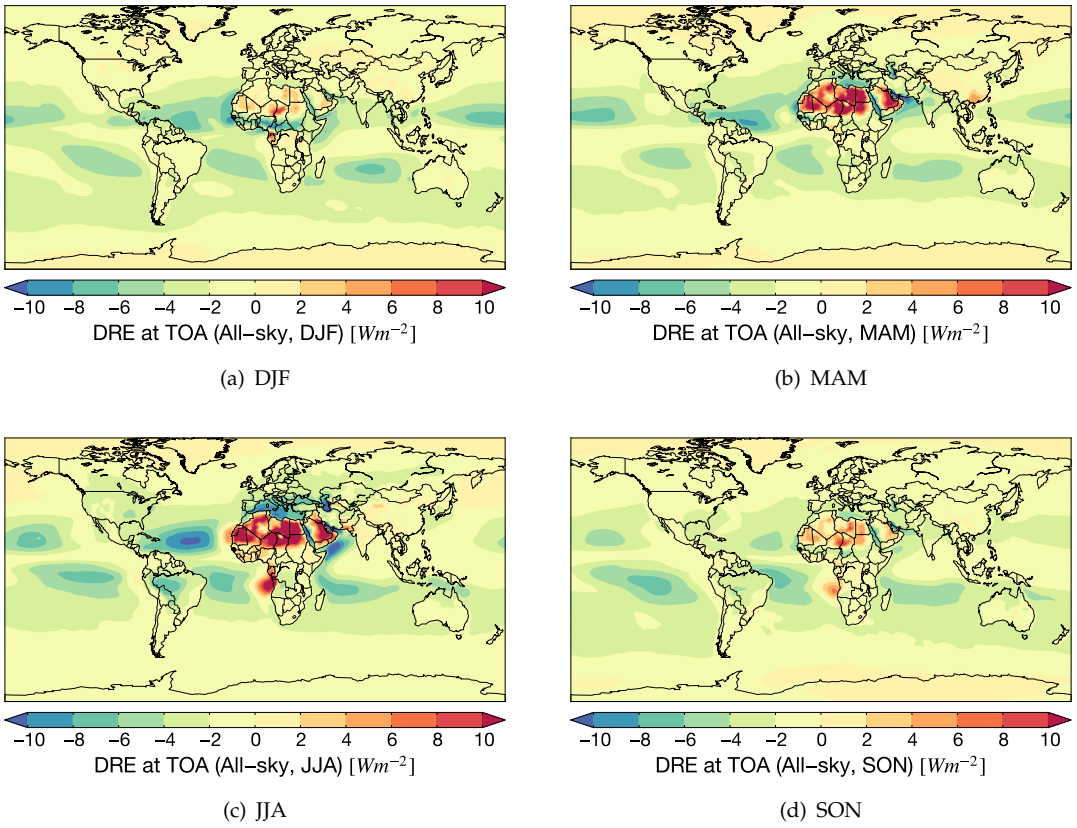

(a) DJF (b) MAM

(c) JJA (d) SON

FIGURE 5.1: Seasonally-averaged maps of modeled all-sky DRE.

During MAM, the direct effect intensifies over the Sahara as windblown dust is lifted by strengthened winds. DRE exceeds 10 W m^{-2} over parts of northern Africa. Elevated values of DRE are also found over eastern Saudi Arabia and southern China. Pockets of negative DRE exist over subtropical high pressure regions of global oceans.

Aerosol DRE is largest over northern Africa in JJA. DRE exceeds 10 W m^{-2} in other regions, including Saudi Arabia and the Angola Basin. Positive DRE over the Angola Basin is a result of absorbing biomass burning aerosols over marine stratocumulus clouds. During this time, aerosol DRE is most negative over subtropical oceanic regions. There is also negative DRE in the Arabian Sea and Mediterranean Sea, presumably influenced by nearby desert dust.

The aerosol direct effect is notably weakened in SON compared to JJA. Mineral dust and biomass burning emissions subside during this season. Over the Sahara, DRE

values are generally less than 5 W m^{-2}. Reduced DRE values are also found over the Middle East and the Angola Basin. Over the oceanic subtropics, all-sky DRE diminishes during SON. Similar to observations, modeled aerosol direct effects are much weaker overall at high latitudes.

Overall, CESM performs reasonably well in simulating the large seasonal variability in all-sky DRE. Global trends observed in CESM simulations of DRE are similar in magnitude to those observed in the 2B-FLXHR-ERB dataset. However, there are significant regional discrepancies between simulations and observations, especially over northern Africa and oceanic subtropical high pressure regions. Over extended spatial and temporal scales, observed and simulated DRE are more comparable.

5.4.2 Seasonal Cycles in Modeled DRE

Figure 5.2 presents DRE from the CESM simulation for *clear-sky*, *cloudy-sky*, and *all-sky* conditions. Peak values of aerosol atmospheric heating occur during the JJA season. Elevated DRE values result from an increased production of absorbing Saharan dust during the JJA season. Simulated aerosol atmospheric heating is strongest under clear-sky conditions, with a maximum value of 4.1 W m^{-2} during June. Minimum values typically occur during the DJF season as values dip as low as 2 W m^{-2}.

Surface DRE remains negative under all sky conditions. Similar to aerosol atmospheric absorption, surface DRE is strongest during the JJA season. Monthly-averaged values generally range between -3.0 and -7.0 W m^{-2}, which are slightly weaker than surface DRE values observed in the 2B-FLXHR-ERB dataset. The minimum value of surface DRE is -7.4 W m^{-2}, as simulated under clear-sky conditions in June.

DRE at the top-of-atmosphere remains relatively constant throughout the year. All DRE values are negative, with exceptions in July and August under cloudy-sky conditions. Under clear-sky conditions, DRE at the top-of-atmosphere ranges between -3.0 and -3.7 W m^{-2}. Under cloudy-sky (other) conditions, values are less negative and range between -0.7 and 0.1 W m^{-2}. Simulated all-sky values are consistent with all-sky values observed in the 2B-FLXHR-ERB dataset.

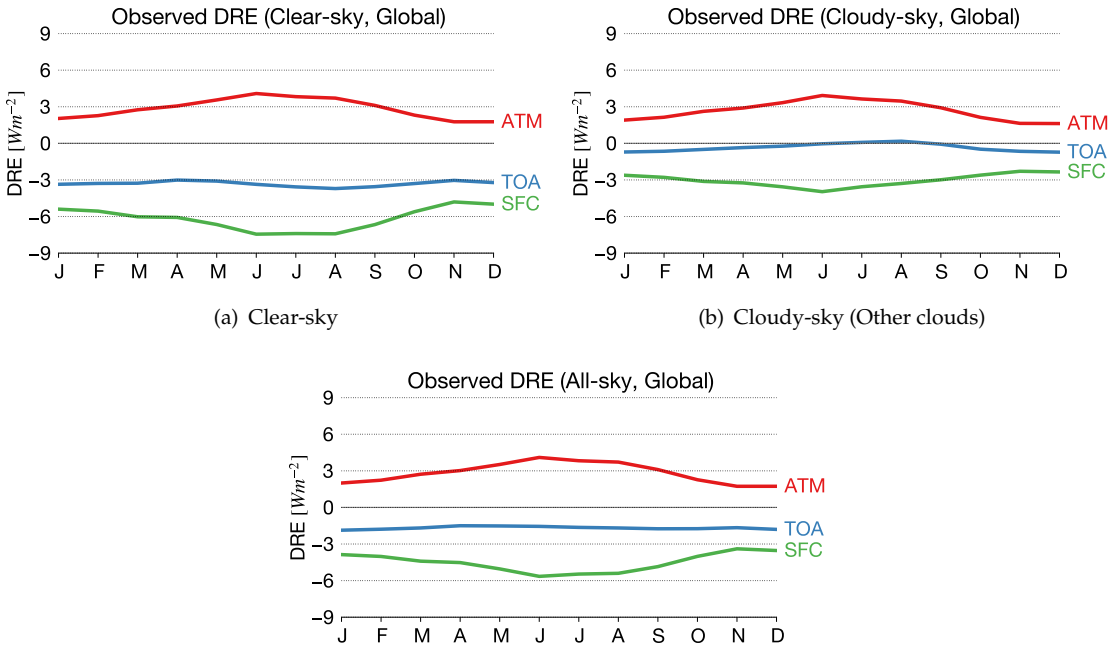

(a) Clear-sky

(b) Cloudy-sky (Other clouds)

(c) All-sky

FIGURE 5.2: Seasonal cycle of modeled aerosol atmospheric heating (red), top-of-atmosphere DRE (blue), and surface DRE (green).

Overall, global time series of simulated DRE agree favorably with global time series of observed DRE. The overall trends observed in CESM simulations are consistent with 2B-FLXHR-ERB observations. The greatest magnitude in surface DRE occurs during the JJA season in both simulations and observations. Finally, global DRE at the top-of-atmosphere shows no seasonal cycle and remains relatively constant during all months.

5.5 Global Distribution of All-sky DRE

While global mean aerosol direct effects and their annual cycle are fairly well-represented in the model, there is evidence of significant regional biases. Figure 5.3 maps the global distribution of simulated annual average all-sky DRE at the top-of-atmosphere, in the atmospheric column, and at the surface. Also shown are differences between modeled and observed DRE at these three levels to highlight regional discrepancies between observed DRE from the 2B-FLXHR-ERB dataset and modeled DRE from the CESM simulation.

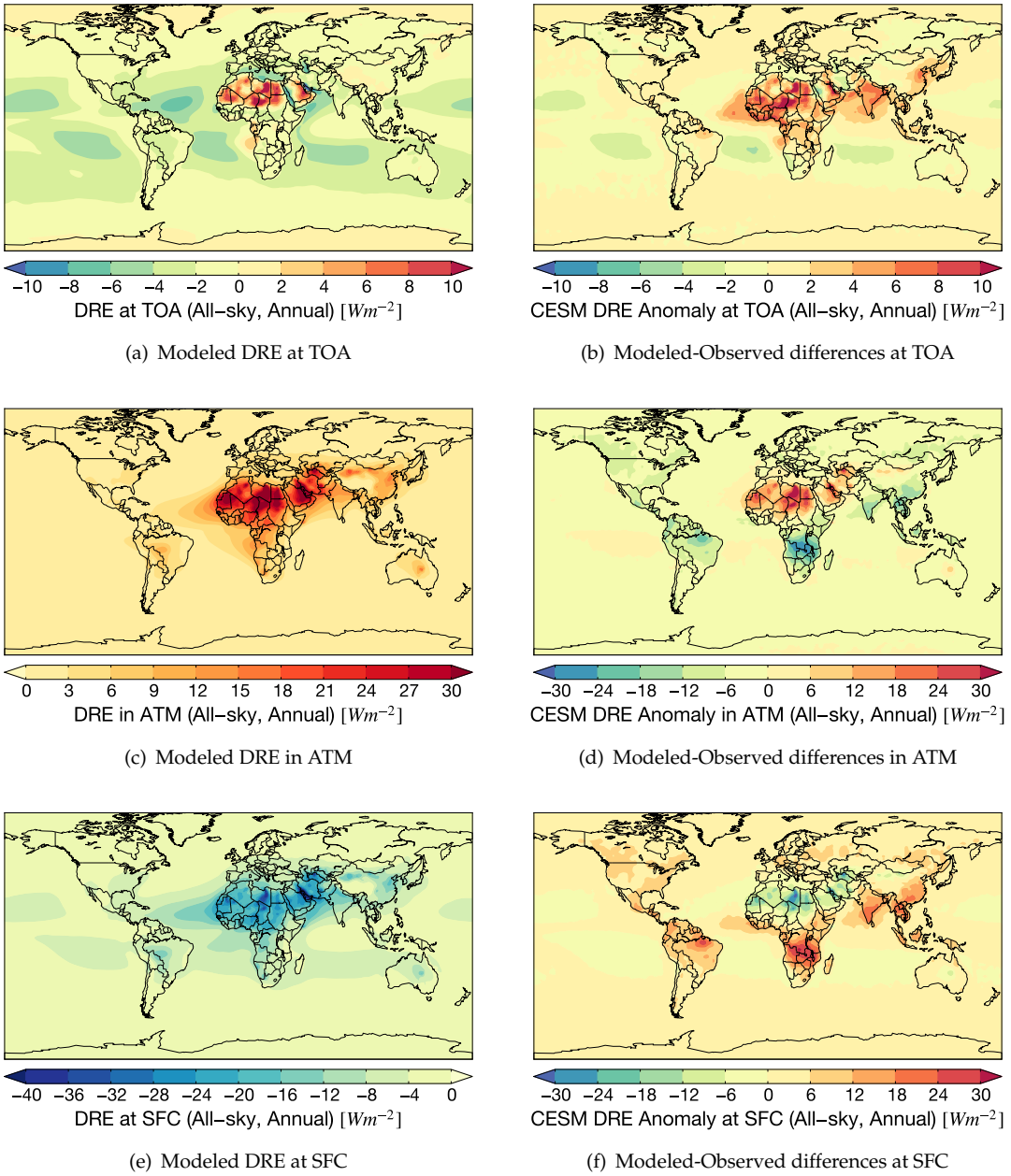

(a) Modeled DRE at TOA

(b) Modeled-Observed differences at TOA

(c) Modeled DRE in ATM

(d) Modeled-Observed differences in ATM

(e) Modeled DRE at SFC

(f) Modeled-Observed differences at SFC

FIGURE 5.3: Modeled all-sky DRE at the top-of-atmosphere, atmospheric column, and surface (a, c, e) and differences in modeled versus observed all-sky DRE (b, d, f).

In contrast to observations, positive DRE exists over much of northern Africa and the Middle East. Over isolated regions of the Sahara, DRE exceeds 10 W m^{-2}, most likely due to the model overestimating the absorption by mineral dust. The map also shows an area of positive DRE over the Angola Basin, resulting from the presence of biomass burning aerosols over marine stratocumulus. Over global oceans, negative DRE predominates over regions of subtropical high pressure.

There are significant differences in DRE at the top-of-atmosphere between CESM simulations and 2B-FLXHR-ERB observations, as highlighted in Figure 5.3(b). While a positive anomaly corresponds to a modeled DRE larger than observations, a negative DRE equates to a modeled DRE smaller than observations. Over northern Africa, India, and China, the CESM DRE anomaly exceeds 5 W m^{-2}. Positive DRE anomalies also exist in isolated pockets of predominantly cloudy areas over ocean.

India and China, which exert strong aerosol cooling in 2B-FLXHR-ERB observations, show negligible aerosol direct effects in the CESM simulation. Northern Africa, which produced slightly positive DRE in observations, exhibits much strongly positive DRE in the model. Although the global estimates of DRE are nearly identical for simulations and observations, there are significant regional discrepancies between the two.

CESM simulates much stronger aerosol absorption than observations in several locations, which correspond to source regions for biomass burning emissions and desert dust transport. However, significantly stronger warming exists over desert dust regions. Both aerosol types, including mineral dust and black carbon, at least partially absorb solar radiation.

The most prominent region of aerosol absorption is in northern Africa. Saharan dust is simulated to heat the atmospheric column by over 30 W m^{-2} in some areas. Aerosol warming is spatially inhomogeneous in the Sahara as atmospheric heating may vary by tens of W m^{-2} over several hundred kilometers. In contrast, the 2B-FLXHR-ERB observations show largest atmospheric heating as a result of biomass burning emissions rather than mineral dust transport.

Compared to 2B-FLXHR-ERB observations, CESM overestimates DRE over northern Africa and underestimates DRE over southern Africa. These two regions feature

distinctly different aerosol types: mineral dust to the north and black carbon to the south. This result is consistent with findings from Shindell et al. (2013), which found that CMIP5 underestimates biomass burning and soot emissions and also overestimates absorbing aerosol optical depth over the Sahara region.

All-sky DRE at the surface is simulated in Figure 5.3(e). Modeled surface DRE is negative everywhere globally, which is consistent with observations from the 2B-FLXHR-ERB dataset. Over northern Africa, surface DRE is -20 W m^{-2} or less. In isolated locations, values exceed -30 W m^{-2}. Unlike 2B-FLXHR-ERB observations, CESM simulates a negligible surface DRE over southern Africa.

Similar to aerosol atmospheric heating, modeled DRE at the surface is spatially heterogeneous over northern Africa. Values may vary by tens of W m^{-2} over several hundred kilometers. The irregular pattern of surface DRE likely results in response to the land surface model used in CESM, in which surface reflectances are highly variable over the Sahara. Whereas CESM simulates strong localized variations in surface DRE, comparable features are not observed in 2B-FLXHR-ERB measurements.

Compared to 2B-FLXHR-ERB observations, CESM underestimates surface DRE over the Sahara and overestimates surface DRE over southern Africa, South Asia, and Brazil. As illustrated in Figure 5.3(f), CESM DRE anomalies exceed 30 W m^{-2} in parts of southern Africa. Furthermore, CESM overestimates land surface DRE by about 5 W m^{-2}.

5.6 The Role of Sky and Surface Conditions

Since CESM takes into account cloud coverage and surface properties, it is possible to separate DRE by surface and sky conditions. Analysis of model output is designed to be consistent with analysis of observations. Simulated DRE is sorted by surface types (land, ocean, and global) and sky conditions (clear-sky, cloudy-sky, and all-sky). While surface types are identical for both model and observational analyses, sky conditions are treated somewhat differently in the model due to differences between observed clouds and the way clouds are reported in large GCM gridboxes. In the model analysis,

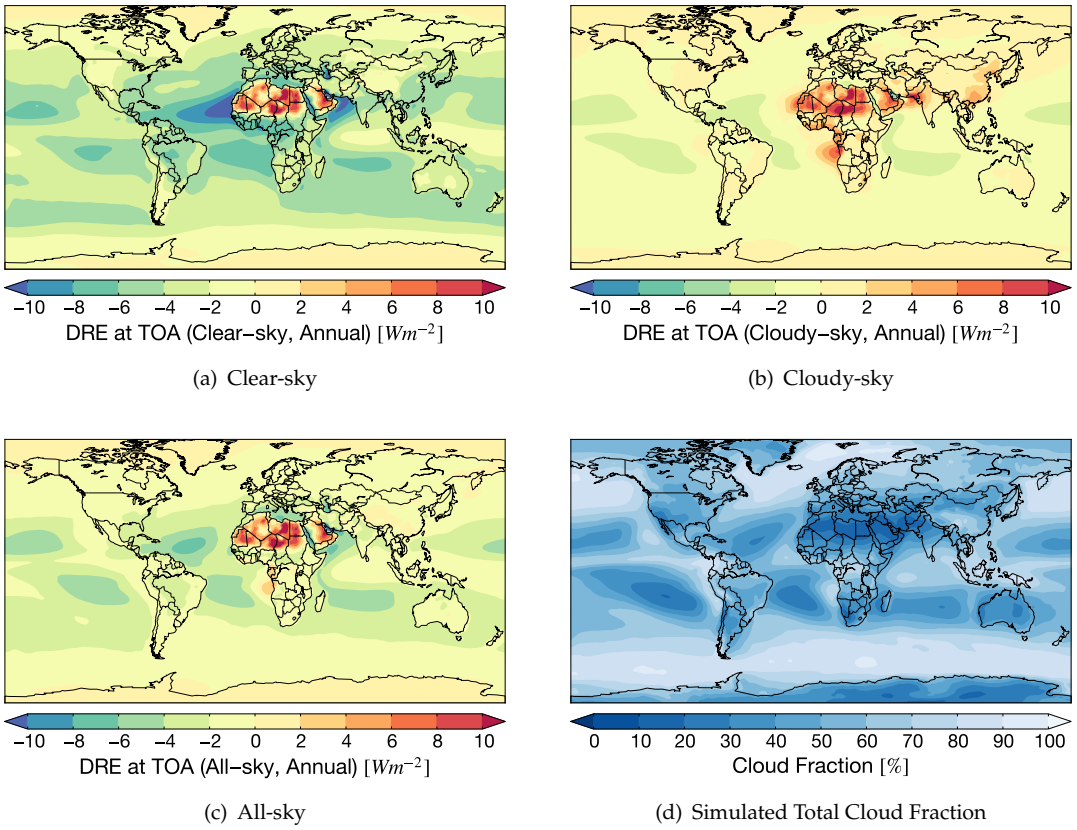

(a) Clear-sky

(b) Cloudy-sky

(c) All-sky

(d) Simulated Total Cloud Fraction

FIGURE 5.4: CESM simulated maps of annual average (a) clear-sky DRE, (b) cloudy-sky DRE, (c) all-sky DRE, and (d) total cloud fraction.

cloudy-sky conditions are treated as a single category, as opposed to further separating out thin cirrus and broken cloud scenes.

Figure 5.4 presents maps of annual average DRE at the TOA under clear-sky, cloudy-sky, and all-sky conditions. Similar to observations, there is considerable variability in modeled DRE based on the presence or absence of clouds. However, the distribution of DRE reveals a notably different pattern in model and observational analyses.

The global distribution of clear-sky DRE, as mapped in Figure 5.4(a), shows predominantly negative aerosol direct effects consistent with 2B-FLXHR-ERB observations. The strongest negative DRE exists over the North Atlantic Ocean and Arabian Sea, likely due to mineral dust transport. DRE is slightly negative over global oceans due to the presence of scattering aerosols over the dark ocean surface. Positive DRE exists over northern Africa and the Middle East, where values exceed 5 W m^{-2}.

Simulated cloudy-sky DRE in Figure 5.4(b) shows mostly positive values of DRE, especially over land. Slightly negative DRE exists over global oceans, with values reaching -3 W m^{-2} over subtropical high pressure regions. Over northern Africa, DRE is greater than 5 W m^{-2}. Positive DRE is also found over the Middle East, South Asia, and off the coast of Angola. Over the Angolan Basin, DRE is positive due to the presence of absorbing biomass burning aerosols over stratocumulus clouds.

All-sky DRE is positive over northern Africa, the Middle East, and the Angolan Basin. The strongest DRE is simulated over the Sahara, where values can exceed 5 W m^{-2}. The modeled distribution of all-sky DRE is heavily influenced by the modeled total cloud fraction over ocean, where values reach as low as -5 W m^{-2} over subtropical high pressure regions. The all-sky map reflects a combination of features highlighted in the clear-sky and cloudy-sky maps weighted by their relative frequency of occurrence. Averaged globally, all-sky DRE maps are comparable between observations and simulations, despite large differences that are quite apparent on regional scales.

Global climate models offer unique insights for assessing the role of aerosols in climate. Recent advancements in modeling have made it possible to simulate complex aerosol properties that contribute significantly to aerosol direct effects. One such widely-used climate model, CESM, simulates aerosol direct effects globally at the top-of-atmosphere and surface. Global observations of DRE provide valuable benchmarks for evaluating the performance of climate models to further scientific understanding of aerosol radiative effects.

Averaged globally, modeled all-sky DRE (-1.7 W m^{-2}) from CESM compares favorably with observed all-sky DRE (-2.0 W m^{-2}) from the 2B-FLXHR-ERB dataset even though global maps highlight notable regional discrepancies. Sorting DRE by sky and surface conditions further reveals that discrepancies depend largely on the environmental conditions in which aerosols are present. For example, an incorrectly simulated cloud can alter the sign of DRE from negative to positive which may alter global estimates. The strong sensitivity of DRE to sky and surface conditions underscores their importance in global and regional assessments of aerosol direct effects.

Chapter 6

Regional Analysis

6.1 Introduction

The results presented in the previous chapters clearly reflect the large spatial and temporal variability of atmospheric aerosols and their optical properties. Assessments of aerosol direct effects often omit these regional complexities in favor of presenting smoothed global averages. As has been previously discussed, localized direct effects can exert significant influence on modifying global averages. Failure to account for regional effects can greatly distort global assessments of aerosol direct effects.

In Chapters 4 and 5, we presented global evaluations of aerosol DRE from 2B-FLXHR-ERB observations and CESM simulations. Although global DRE remains fairly consistent between observations and simulations, results tend to show disagreement as DRE is evaluated over finer spatial and temporal scales. The categorization of DRE by surface and sky conditions further reveals that regional discrepacies between modeled and observed DRE may be at least partially explained by differences in surface reflection and cloud cover. This chapter aims to further resolve these discrepancies through detailed analyses of aerosol direct effects over selected regions.

6.2 Overview of Regions

The observed strength of aerosol direct effects is often linked to the relative proximity of particles to their source regions. For example, aerosol direct effects from Saharan dust are generally strongest over or near the Sahara. Since aerosols typically have atmospheric residence times of less than one week, observed particle concentrations are largest within several hundred kilometers of the aerosol source.

It follows, therefore, that the source regions of aerosols exhibit the most pronounced direct effects. Over deserts, mineral dust aerosols tend to predominate aerosol radiative impacts. Over industrialized locations, anthropogenic emissions can produce potentially strong localized effects. However, meteorological conditions, atmospheric chemistry, and topography can also greatly influence the spatial distribution of aerosols.

To further investigate regional discrepancies, observed and simulated aerosol direct effects are analyzed over several known source regions for aerosols. The regions are selected to capture the full variability in global aerosol direct effects. Figure 6.1 shows the map of observed annual average all-sky DRE from Figure 4.2(a), as well as inset boxes showing the cumulative density function (CDF) of aerosol direct effects over six selected regions, including the United States, Sahara, China, Chile, Angola, and India.

The CDF of each region features a characteristic shape. Some regions, like South Asia, have a gentle slope. Other regions, like the southeast Pacific, have a steep slope. Even without quantitative values on the axes, the shape of each CDF describes the relative likelihood of a random observation less than or equal to a given value of DRE. Whereas a gentle slope indicates a broad range of observed values, a steep slope indicates a narrow range of observed values. Here we will explore, in detail, aerosol direct effects over these six regions from three broad geographic areas: the Americas, Africa, and Asia.

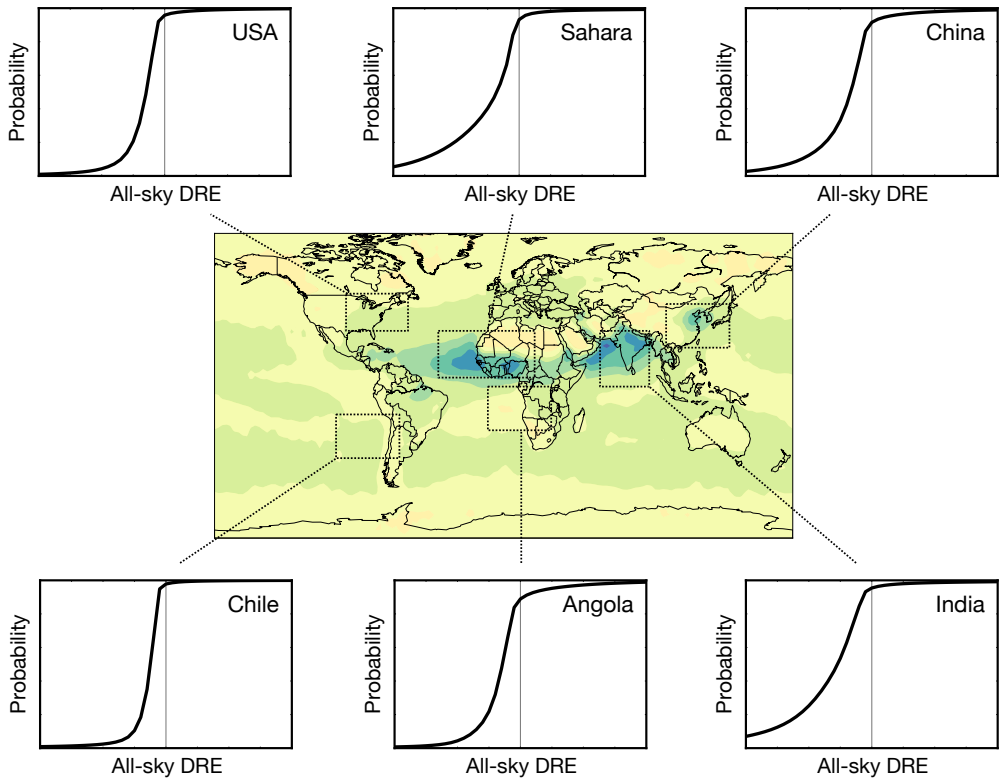

FIGURE 6.1: Regional CDFs highlight the large variability in global DRE observations.

6.3 The Americas

6.3.1 United States

The first region presented in this analysis, hereafter referred to as 'USA', consists of the area bounded by 30°N, 50°N, 100°W, and 60°W. This region encompasses the eastern half of the continental United States, as well as parts of southeastern Canada and the North Atlantic Ocean.

A major source of aerosols in this region is industrial emissions, which result in the production of primary and secondary aerosols. During boreal summer, gas-to-particle reactions contribute to elevated particle concentrations over the eastern United States. In addition, windblown mineral dust from Africa can be carried thousands of kilometers across the Atlantic Ocean before settling over the southeastern United States. The

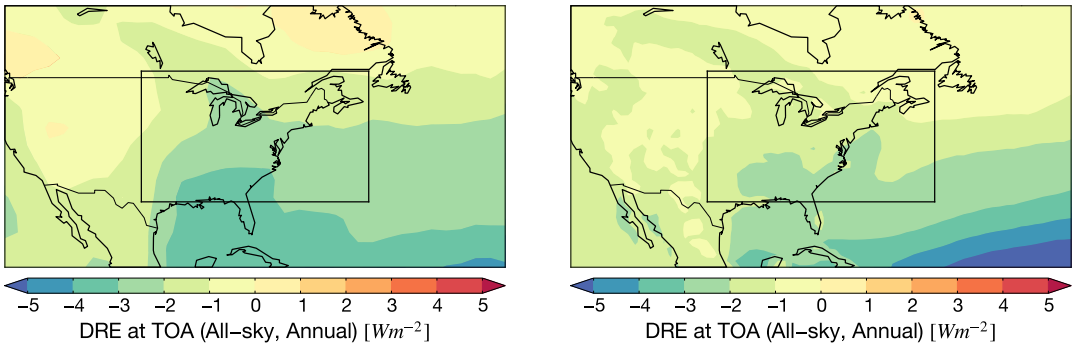

(a) 2B-FLXHR-ERB Observations (b) CESM Simulation

FIGURE 6.2: Maps of annual average all-sky DRE over the 'USA' region shown from (a) 2B-FLXHR-ERB observations and (b) CESM simulation.

presence of domestic and foreign sources of atmospheric particles can greatly influence aerosol direct effects over the United States.

Figure 6.2 compares maps of annual average all-sky DRE from 2B-FLXHR-ERB observations and CESM simulations. The observations are shown at a horizontal resolution of 2.5°x2.5°, whereas the model has a horizontal resolution of 1.0°x1.25°. A black rectangular bounding box is drawn to highlight the 'USA' region. Coastlines illustrated on both maps delineate regions defined as land and ocean in the subsequent analysis.

Within this region, observed annual average all-sky DRE are negative over both land and ocean, as shown in Figure 6.2(a). Observed and modeled DRE is strongest over the southeastern United States, where observational estimates exceed -3 W m^{-2} in some places and become increasingly weaker further north and west. CESM appears to perform well in capturing the spatial pattern of all-sky DRE but tends to slightly underestimate its magnitude.

The sources and sinks of aerosols in this region are driven largely by interannual shifts in temperature and vegetation causing significant responses in aerosol direct effects. To explore the interannual variability over the eastern United States, the seasonal cycle of aerosol direct effects from 2B-FLXHR-ERB observations and CESM simulations is presented in Figure 6.3.

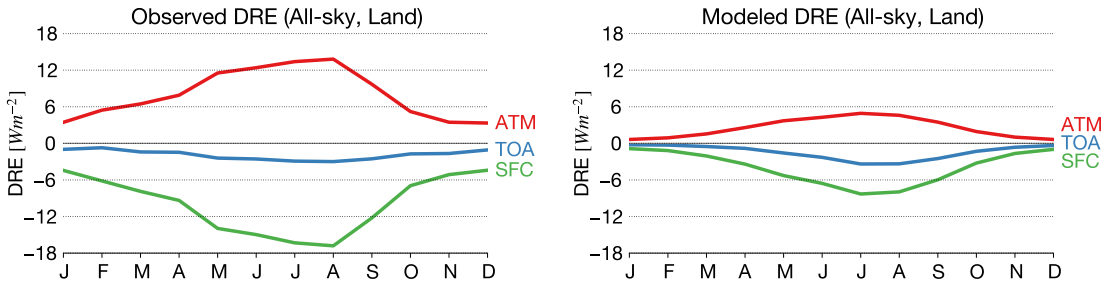

(a) 2B-FLXHR-ERB Observations (b) CESM Simulation

FIGURE 6.3: Seasonal cycle of aerosol atmospheric heating (red), top-of-atmosphere DRE (blue), and surface DRE (green) over the 'USA' land region.

Seasonal trends are similar for both observations and simulations. Throughout the year, DRE remains positive within the atmospheric column and negative at the top-of-atmosphere and surface. All-sky DRE at the top-of-atmosphere is most negative during JJA. However, surface DRE and aerosol atmospheric heating is weaker in magnitude in the model compared to observations. Despite significant discrepancies at the surface and within the atmospheric column, DRE at the top-of-atmosphere shows reasonably good agreement between observations and simulations.

The CDFs describe the random probabililty of an observation less than or equal to a given value of DRE. There is a 0% probability of observing DRE less than a large negative value and a 100% probability of observing DRE less than a large positive value. The shape of a CDF depends on several factors, including seasonality and sky conditions. Another measure of the variability in DRE is its standard deviation. Figure 6.4 presents CDFs of observed DRE under various sky conditions, observed over the United States. The beige shading highlights the spread of data observed within one standard deviation of the median, that is, between the 15.9 and 84.1 percentiles.

The seasonal variability in clear-sky DRE over the United States is illustrated in Figure 6.4(a). DRE is strongest (most negative) during JJA and weakest (least negative) during DJF. Variability, as indicated by both the shape of the CDF and the range of values encompassed by one standard deviation, is also largest for JJA and smallest in DJF. Similar trends are observed under cirrus conditions in Figure 6.4(b).

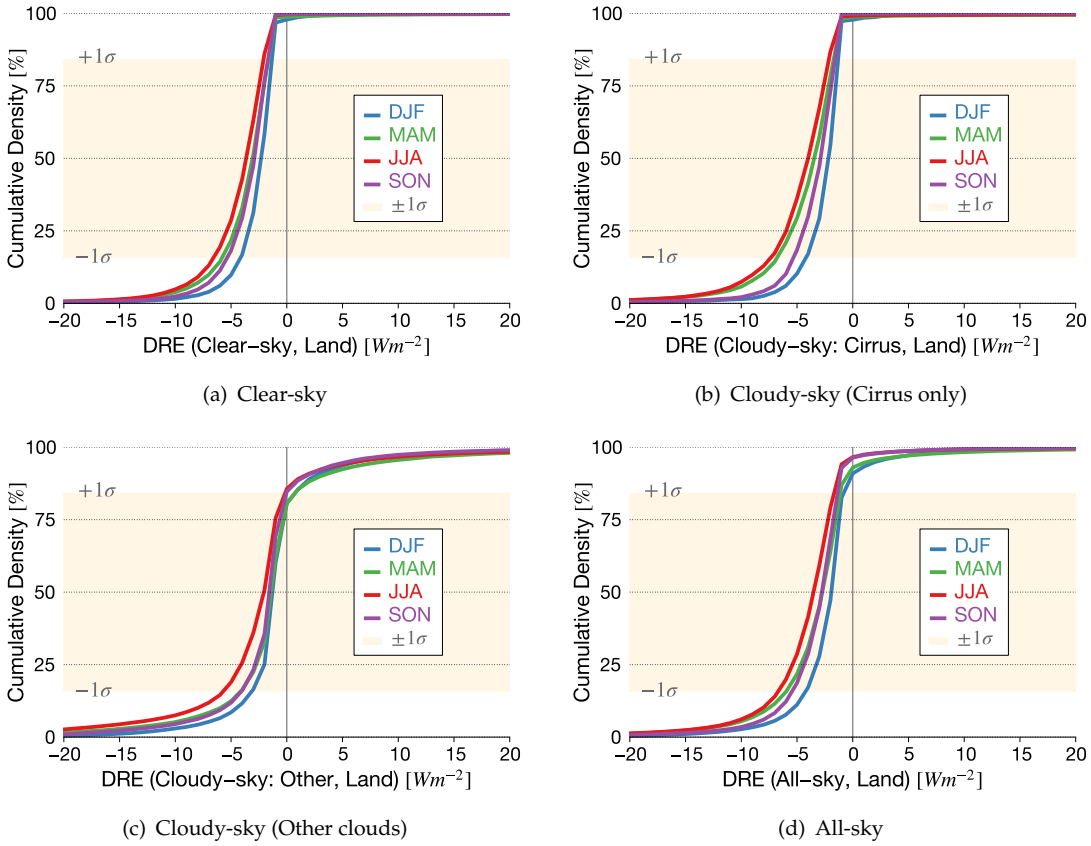

(a) Clear-sky

(b) Cloudy-sky (Cirrus only)

(c) Cloudy-sky (Other clouds)

(d) All-sky

FIGURE 6.4: CDFs of (a) clear-sky DRE, (b) cloudy-sky (cirrus only) DRE, (c) cloudy-sky (other clouds) DRE, and (d) all-sky DRE observed over the 'USA' land region.

Figure 6.4(c) reveals a slightly different distribution of DRE observed under cloudy skies. CDF plots are considerably more s-shaped, which suggests a greater percentage of extreme negative DRE observations and a significant number of scenes exhibiting positive DRE that are seldom found in clear-sky or cirrus scenes. The one-sigma range includes values from -6 W m^{-2} to 0 W m^{-2} during JJA and -3 W m^{-2} to 1 W m^{-2} in DJF. During all seasons, over 15% of cloudy-sky DRE observations are greater than zero. In contrast, less than 5% of clear-sky DRE observations are greater than zero at any given season and these occur primarily during winter and spring when absorbing aerosols are observed over bright snow-covered surfaces.

When combined over all conditions, as shown in Figure 6.4(d), the greatest probability of positive DRE (8%) occurs during DJF. The standard deviation of all-sky DRE ranges from -7 W m^{-2} to -2 W m^{-2} in JJA and ranges from -4 W m^{-2} to -1 W m^{-2} in

TABLE 6.1: Estimates of annual average DRE [W m^{-2}] and fractional occurrence [%] for each category over the 'USA' region, from 2B-FLXHR-ERB (top) and CESM (bottom) datasets. The standard deviations of observed values are shown in parentheses.

2B-FLXHR-ERB Observed DRE and Percent of Total

$[Wm^{-2}]$	Clear-sky	Cloudy-sky (cirrus)	Cloudy-sky (other)	Mixed-sky	All-sky
Land	-2.5 (4.0)	-2.9 (5.7)	-0.3 (10.3)	-3.2 (5.6)	-2.1 (6.5)
Ocean	-2.1 (3.3)	-2.1 (3.9)	-1.0 (8.4)	-2.3 (4.0)	-1.8 (5.3)
Total	-2.6 (3.6)	-3.0 (4.7)	-0.7 (8.0)	-3.2 (4.6)	-2.2 (5.4)
[%]	Clear-sky	Cloudy-sky (cirrus)	Cloudy-sky (other)	Mixed-sky	All-sky
Land	29	5	15	11	60
Ocean	16	3	10	11	40
Total	45	8	25	22	100

CESM Simulated DRE and Percent of Total

$[Wm^{-2}]$	Clear-sky		Cloudy-sky		All-sky
Land	-3.1		0.4		-1.4
Ocean	-3.0		-0.3		-1.2
Total	-3.4		0.1		-1.5
[%]	Clear-sky	Cloudy-sky (high clouds)	Cloudy-sky (low clouds)	Cloudy-sky (mid clouds)	All-sky
Land	23	15	8	6	60
Ocean	23	19	17	8	40
Total	46	33	25	13	100

DJF. Overall, the JJA season exhibits slightly more variability in all-sky DRE observations than any other season.

Table 6.1 compares the contributions of various sky and surface conditions to annual average DRE. The top table shows results from 2B-FLXHR-ERB observations and the bottom table shows results from the CESM simulation. The corresponding standard deviations of observed values are shown in parentheses. Also displayed are the percentages of pixels observed and simulated for each category. Note that 2B-FLXHR-ERB observed DRE is sorted into five sky conditions, whereas CESM simulated DRE is sorted into only three sky conditions.

Clear-sky DRE values are less negative in the observations (-2.6 W m^{-2}) than the simulations (-3.4 W m^{-2}). Both observations and simulations report stronger aerosol direct effects over land than over ocean. Under cloudy skies, much larger differences exist. Observed DRE (-0.7 W m^{-2}) is negative whereas simulated DRE (0.1 W m^{-2}) is positive. The modeled and observed contributions of land and ocean surfaces are also significantly different. In both cases, simulated values of DRE are 0.7 W m^{-2} more positive than observed values of DRE. However, cloudy-sky values are consistently more positive than all-sky values.

In the United States, all-sky DRE is more negative in observations (-2.2 W m^{-2}) than simulations (-1.5 W m^{-2}). Observations reveal an all-sky DRE over land of -2.1 W m^{-2} and an all-sky DRE over ocean of -1.8 W m^{-2}. These values are more negative than the simulated all-sky DRE over land (-1.4 W m^{-2}) and ocean (-1.2 W m^{-2}). The contribution to DRE from the 'USA' region is comparable to the global value of all-sky DRE.

Overall, the eastern United States is strongly influenced by both domestic and foreign sources of aerosols. Annual averages over this region are shown to be comparable for observed and simulated DRE. However, there are regional discrepancies which become increasingly more apparent once DRE is categorized by surface and sky conditions. Over the United States, aerosol direct effects are relatively small compared to other parts of the world. As we will see, regional aerosol direct effects and model biases can be much larger in other parts of the world.

6.3.2 Chile

Consisting of the western coastline of South America and the southeastern Pacific Ocean, the 'CHILE' region shifts our analysis to the Southern Hemisphere. The 'CHILE' region is defined as a box bounded by 40°S, 15°S, 105°W and 65°W and includes the industrialized city of Santiago, Chile, where heavy industry is a source for anthropogenic aerosols. Furthermore, the southeast Pacific Ocean is an area known for its wide variability in boundary layer, cloud, and aerosol properties.

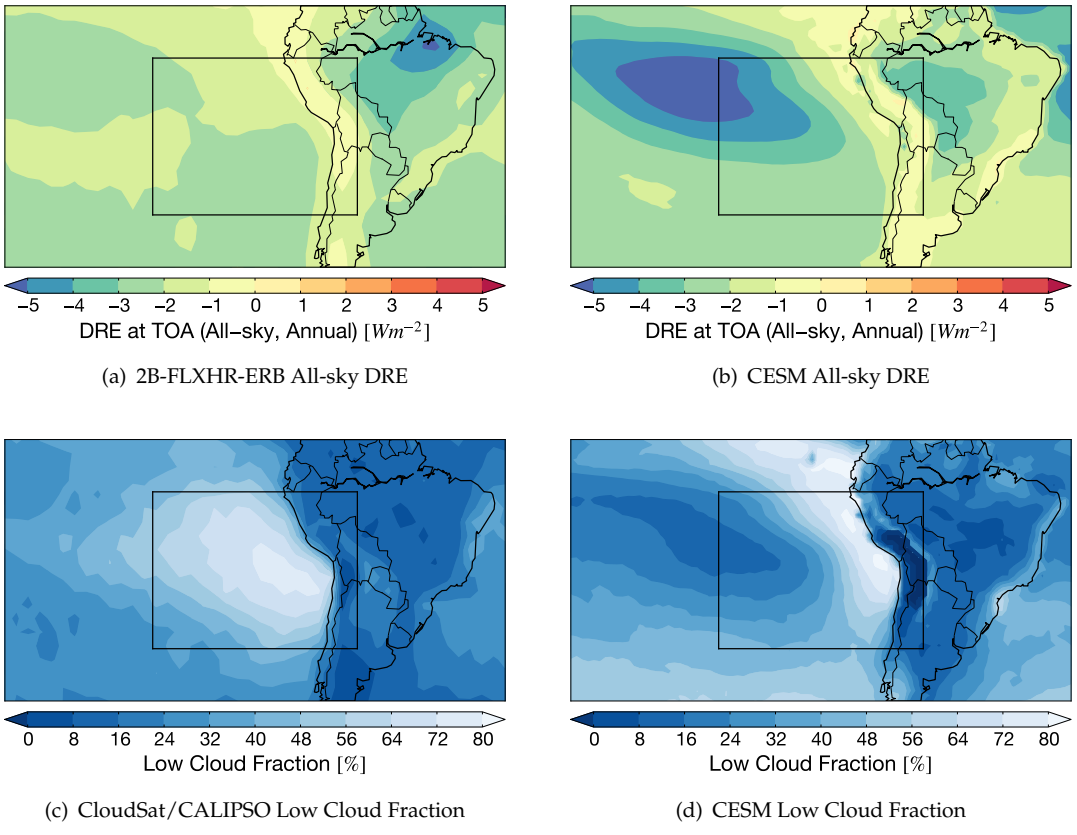

(a) 2B-FLXHR-ERB All-sky DRE

(b) CESM All-sky DRE

(c) CloudSat/CALIPSO Low Cloud Fraction

(d) CESM Low Cloud Fraction

FIGURE 6.5: Maps of annual average all-sky DRE and low cloud fraction over the 'CHILE' region from (left) 2B-FLXHR-ERB observations and (right) CESM simulation.

The major sources of aerosols in this region include copper smelting emissions and oceanic sea spray. The Andes mountains exert significant topographic effects on atmospheric transport in this region and strongly influence the distribution of aerosols along the western coast of South America. By design, a sizable fraction of the 'CHILE' region is located over ocean to allow observed and simulated aerosol direct effects over the southeast Pacific Ocean to be compared.

Figure 6.5 presents maps of annual average all-sky DRE from both 2B-FLXHR-ERB observations and CESM simulations. The 'CHILE' region is marked by the black rectangular box. Observed all-sky DRE is negative over the ocean over the southeast Pacific, as indicated in Figure 6.5(a). However, there are several observations of positive DRE over the Andes Mountains due to the presence of absorbing aerosols over snow-capped surfaces. The distribution of all-sky DRE is relatively homogeneous over ocean,

but exhibits a strong gradient associated with the Andes mountains over land.

Simulated DRE's tend to agree well with observations over land but exhibit anomalously large negative values ($<$ -5 W m^{-2}) in the northwest quadrant. The southeast Pacific region supports one the world's largest semi-permanent cloud decks. These marine stratocumulus clouds can strongly influence aerosol direct effects over the ocean. Also shown in Figure 6.5 are maps of the annual average fraction of low clouds from CloudSat/CALIPSO observations and CESM simulations. Low clouds are defined as those with a ECMWF-derived cloud top temperature warmer than 273 K.

Observations and simulations resolve different distributions of low cloud fraction. CloudSat and CALIPSO observe a stratocumulus deck which extends westward over 3000 km from the Chilean coast. On the contrary, CESM simulates a stratocumulus deck which extends westward less than 1500 km from the Chilean coast. This result is consistent with findings from Kay et al. (2012), which found that CAM5 simulations underestimate the low cloud fraction of marine stratocumulus. By comparing maps of all-sky DRE and low cloud fraction, it is evident that the geographic extent of the clouds play an important role in determining the regional aerosol direct effects.

The simulated distribution of low cloud fraction mirrors the simulated distribution of DRE. The trend is most apparent within the northern extent of the 'CHILE' region. An area of relatively clear sky ($<$ 40% low cloud fraction) corresponds to strong negative DRE ($<$ -4 W m^{-2}). Conversely, an area of relatively cloudy skies ($>$ 40% low cloud fraction) corresponds to nearly neutral DRE ($\sim$ 0 W m^{-2}). The gradient in simulated low cloud fraction is located in the same area as the gradient in simulated DRE.

Monthly-averaged all-sky DRE over ocean from 2B-FLXHR-ERB observations and CESM simulations are plotted in Figure 6.6. Overall, monthly-averaged DRE values are significantly weaker over the southeast Pacific than the United States. Observed all-sky DRE at the top-of-atmosphere vary between 0.5 W m^{-2} and 1.5 W m^{-2}. At the surface, DRE is negative with minimum values around 4 W m^{-2} during DJF.

Similar seasonal trends are observed in simulated DRE. Figure 6.6(b) reveals a slight seasonal cycle in which DRE is strongest during DJF and weakest during JJA. DRE values within the atmospheric column, at the top-of-atmosphere, and at the surface are

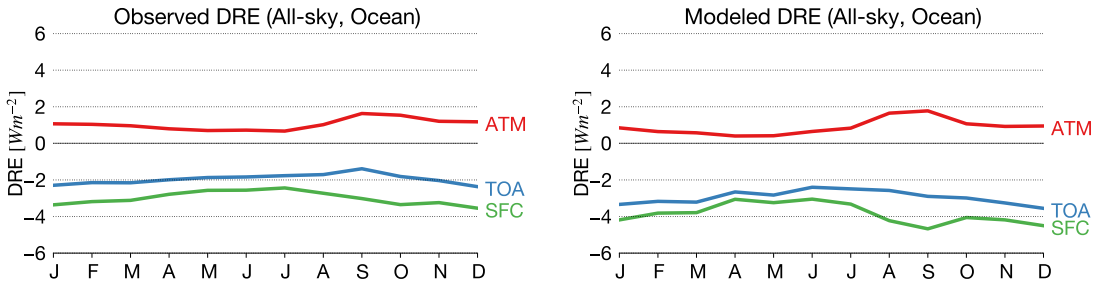

(a) 2B-FLXHR-ERB Observations (b) CESM Simulation

FIGURE 6.6: Seasonal cycle of aerosol atmospheric heating (red), top-of-atmosphere DRE (blue), and surface DRE (green) over the 'CHILE' ocean region.

consistent between model and observations. Overall, the CESM simulation over the southeast Pacific is in very good agreement with 2B-FLXHR-ERB observations.

Figure 6.7 plots CDFs of DRE under various sky conditions. The southeast Pacific is the only region featured in this study without a pronounced seasonal cycle in DRE. There are few source regions for aerosols in this part of the world, besides occasional volcanic eruptions. Sea salt is the main contributor to DRE over remote oceanic areas. Over the southeast Pacific, aerosol direct effects are relatively weak, which is indicative of clean and mostly aerosol-free air. Only cloudy skies exhibit an appreciable seasonal change in cloud properties or aerosols.

Table 6.2 evaluates the regional contribution of the southeast Pacific to annual average DRE, revealing overall consistency between observed and simulated estimates of DRE. Under clear skies, observed DRE values (-1.9 W m^{-2}) are less negative than simulated DRE values (-3.3 W m^{-2}). This result is evident in the land and ocean categories as well. Estimates of clear-sky DRE over land are in much better agreement. Furthermore, clear-sky DRE over ocean is -2.1 W m^{-2} and -3.8 W m^{-2} for observations and simulations, respectively. The unrealistic representation of marine stratocumulus contributes to a negative bias in simulated DRE over ocean.

Over this region, observed cloudy-sky DRE (-1.2 W m^{-2}) is similar to simulated DRE (-0.9 W m^{-2}). However, cloudy-sky DRE over land is nearly 1 W m^{-2} greater in the observations (1.2 W m^{-2}) than simulations (0.3 W m^{-2}). This result is apparent in Figure 6.5(a), where positive DRE exists over mountaneous terrain. Exceptionally

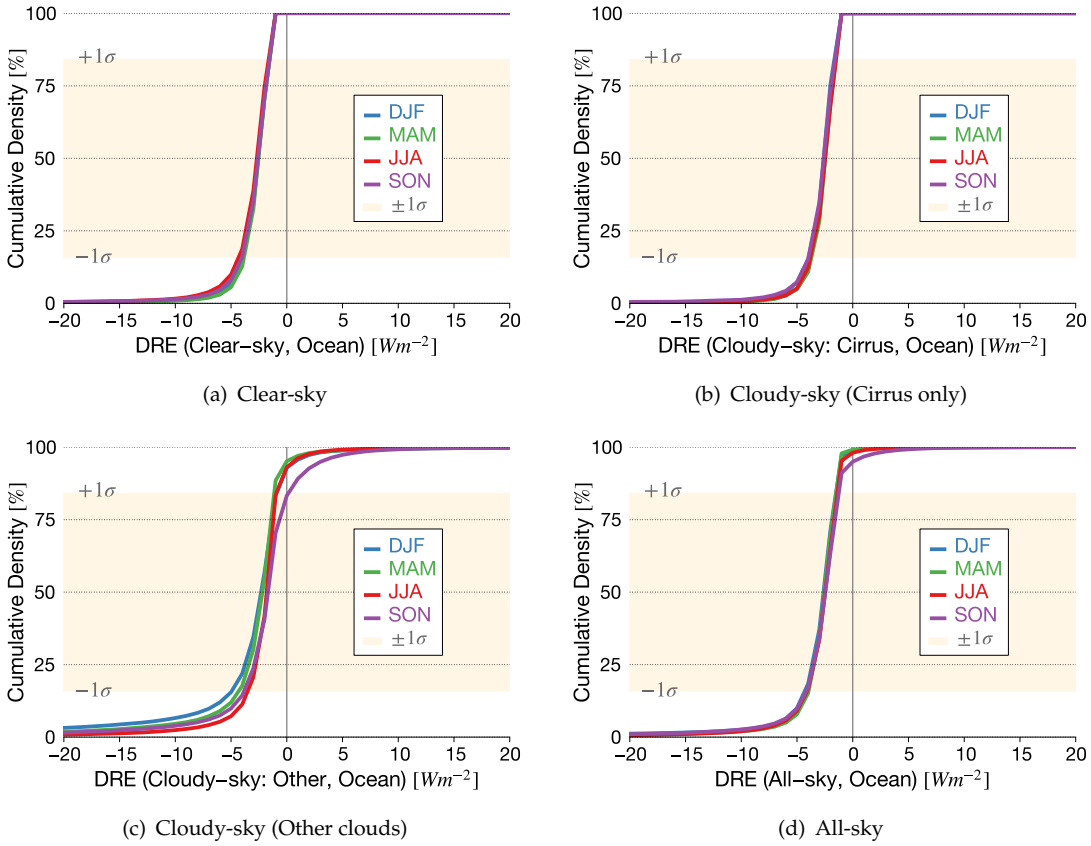

(a) Clear-sky

(b) Cloudy-sky (Cirrus only)

(c) Cloudy-sky (Other clouds)

(d) All-sky

FIGURE 6.7: CDFs of (a) clear-sky DRE, (b) cloudy-sky (cirrus only) DRE, (c) cloudy-sky (other clouds) DRE, and (d) all-sky DRE observed over the 'CHILE' ocean region.

dry conditions on the leeward side of the Andes lead to the production of absorbing mineral dust aerosols. The warming effect from absorbing aerosols is not resolved to the same extent in the CESM simulation.

All-sky DRE values are quite similar in observations (-1.8 W m^{-2}) and simulations (-2.0 W m^{-2}). There is good agreement between values over land and ocean as well. The 2B-FLXHR-ERB dataset observes an all-sky DRE over land of -0.5 W m^{-2} and an all-sky DRE over ocean of -2.1 W m^{-2}. Similarly, CESM simulates an all-sky DRE over land of -0.8 W m^{-2} and an all-sky DRE over ocean of -2.4 W m^{-2}. However, closer inspection reveals that this agreement is the result of a cancellation of errors in clear-sky and cloudy-sky DRE.

Overall, the southeast Pacific is one of the cleanest areas of the world, in terms of

TABLE 6.2: Estimates of annual average DRE [W m^{-2}] and fractional occurrence [%] for each category over the 'CHILE' region, from 2B-FLXHR-ERB (top) and CESM (bottom) datasets. The standard deviations of observed values are shown in parentheses.

2B-FLXHR-ERB Observed DRE and Percent of Total

$[Wm^{-2}]$	Clear-sky	Cloudy-sky (cirrus)	Cloudy-sky (other)	Mixed-sky	All-sky
Land	-2.0 (5.1)	-2.0 (4.9)	1.2 (10.0)	-1.0 (5.8)	-0.8 (7.0)
Ocean	-1.9 (2.5)	-1.7 (2.2)	-1.7 (5.9)	-2.3 (3.5)	-2.0 (3.9)
Total	-2.0 (2.9)	-1.8 (3.0)	-1.2 (6.4)	-2.1 (3.8)	-1.8 (4.3)
[%]	Clear-sky	Cloudy-sky (cirrus)	Cloudy-sky (other)	Mixed-sky	All-sky
Land	6	1	3	4	14
Ocean	34	2	20	30	86
Total	40	3	23	34	100

CESM Simulated DRE and Percent of Total

$[Wm^{-2}]$	Clear-sky		Cloudy-sky		All-sky
Land	-2.6		0.1		-1.3
Ocean	-4.4		-1.4		-2.9
Total	-4.0		-1.2		-2.6
[%]	Clear-sky	Cloudy-sky (high clouds)	Cloudy-sky (low clouds)	Cloudy-sky (mid clouds)	All-sky
Land	8	5	2	3	14
Ocean	45	11	31	2	86
Total	53	17	33	5	100

aerosol concentrations. There are few sources of aerosols within the domain. Furthermore, the aerosols present in the southeast Pacific are not exceptionally radiatively-active. The dominant control in determining aerosol direct effects in this region is clouds. The marine stratocumulus deck has a dominant influence in shaping the regional distribution of DRE. Whereas observations reveal an expansive cloud deck, model simulations show more confined cloud cover. Unrealistic representations in marine stratocumulus contribute a significant source of systematic error in model simulations of aerosol direct effects.

6.4 Africa

6.4.1 Sahara

In the previous section, we discussed aerosol direct effects over the United States and southeast Pacific, regions which experience moderately weak aerosol direct effects. We now shift our attention to Africa, a continent with considerably more abundant sources of natural aerosols. The 'SAHARA' region is defined as a box bounded by 5°N, 30°N, 40°W, and 20°E. This region encompasses most of North Africa and the Sahel, as well as parts of the north Atlantic Ocean. Although this region includes large industrialized cities, the largest contribution originates from mineral dust from the Sahara Desert.

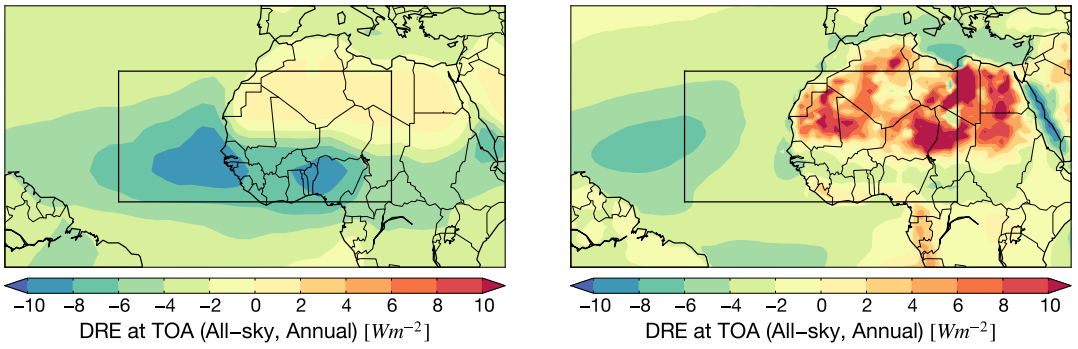

(a) 2B-FLXHR-ERB Observations (b) CESM Simulation

FIGURE 6.8: Maps of annual average all-sky DRE over the 'SAHARA' region shown from (a) 2B-FLXHR-ERB observations and (b) CESM simulation.

The Sahara Desert is the largest source of mineral dust worldwide, although dust distributions are highly variable at different timescales (Mahowald et al., 2006). These particles can be lifted by convection over the hot desert surface and carried to high altitudes. In the troposphere, winds can transport the aerosols over thousands of kilometers. The lack of precipitation over arid regions extends the lifetime of mineral dust aerosols, which are rarely scavenged by wet deposition over the Sahara Desert.

As shown in Figure 6.8, large discrepancies exist between regional distributions of annual average all-sky DRE from 2B-FLXHR-ERB observations and CESM simulations.

The differences occur not only in the magnitude in DRE, but over the spatial distribution as well. Both maps reveal distinctly different aerosol direct effects over the Sahara Desert versus the Sahel further south.

Observed annual average all-sky DRE, as mapped in Figure 6.8(a), is positive over the Sahara, negative over the Sahel, and negative over the North Atlantic. Positive values reach 2 W m^{-2} over the desert, while negative values exceed -8 W m^{-2} in some ocean locations. The area of negative DRE extends several thousand kilometers off the western coast of Africa.

Observations are significantly different from modeled all-sky DRE, as illustrated in Figure 6.8(b). CESM simulates a patchy distribution of extremely strong positive DRE over the desert, as values exceed 10 W m^{-2} in some locations. The expansive area of strongly negative DRE over oceans found in the 2B-FLXHR-ERB dataset is nonexistent in model simulations. Weaker negative values, around -2 W m^{-2}, are found over the Sahel and North Atlantic. Interannual variability in aerosol direct effects over West Africa is primarily caused by the meridionally shifting ITCZ that influences the production of mineral dust aerosols and subsequent long-range transport. The greatest activity in Saharan dust transport typically occurs during the JJA season.

Figure 6.9 compares the annual cycle of all-sky DRE over land from 2B-FLXHR-ERB observations and CESM simulations. Simulated DRE is much stronger in magnitude than observed DRE, which is consistent with findings from Shindell et al. (2013) which found that CMIP5 overestimates the absorbing aerosol optical depth of Saharan dust. Observed all-sky DRE remains fairly constant throughout the year, whereas simulated DRE exhibits a pronounced seasonal cycle peaking in June and reaching a minimum in November. The seasonal cycle shown in Figure 6.9(b) is consistent with the seasonal cycle in Saharan dust loading. However, the magnitudes in the simulation are inconsistent with observations.

CDFs of DRE are plotted under various sky conditions in Figure 6.10. These plots reveal the distribution of observed DRE values over northwestern Africa. There is slight seasonal variability in clear-sky DRE over the Sahara, according to Figure 6.10(a). The

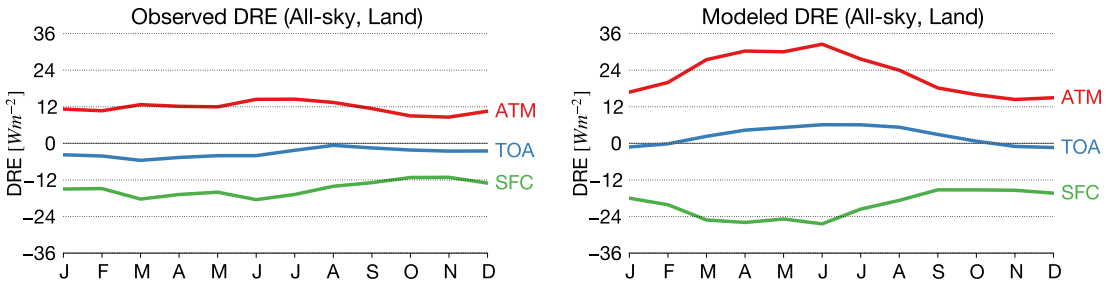

(a) 2B-FLXHR-ERB Observations (b) CESM Simulation

FIGURE 6.9: Seasonal cycle of aerosol atmospheric heating (red), top-of-atmosphere DRE (blue), and surface DRE (green) over the 'SAHARA' land region.

variability in DRE is strongest during DJF and weakest during JJA. In DJF standard deviation ranges from -10 W m^{-2} to -1 W m^{-2}. In JJA, the standard deviation ranges from -4 W m^{-2} to 0 W m^{-2}. Nearly 20% of clear-sky DRE observations in JJA are greater than zero, which is more than in any other month. The ITCZ advances to its northernmost position during the boreal summer which corresponds to the most active period for Saharan dust storms.

Similarly, Figure 6.10(c) shows a slight seasonal variability in cloudy-sky DRE. The spread in observed values is comparable under both clear and cloudy skies. In DJF standard deviation ranges from -10 W m^{-2} to 0 W m^{-2}. In JJA standard deviation ranges from -6 W m^{-2} to 1 W m^{-2}. The greatest probability of positive cloudy-sky DRE occurs during JJA. In contrast, the greatest probability of observing cloudy-sky DRE stronger than -10 W m^{-2} occurs during DJF.

Figure 6.10(d) reveals seasonal variability in all-sky DRE, especially for negative values. Results reflect the combination of observations under clear-sky and cloudy-sky conditions. The most variable season is MAM, whereas the least variable season is SON. In MAM standard deviation ranges from -13 W m^{-2} to 0 W m^{-2}. In SON standard deviation ranges from -8 W m^{-2} to 0 W m^{-2}. The interannual variability in all-sky DRE is largely influenced by the seasonally-shifting ITCZ.

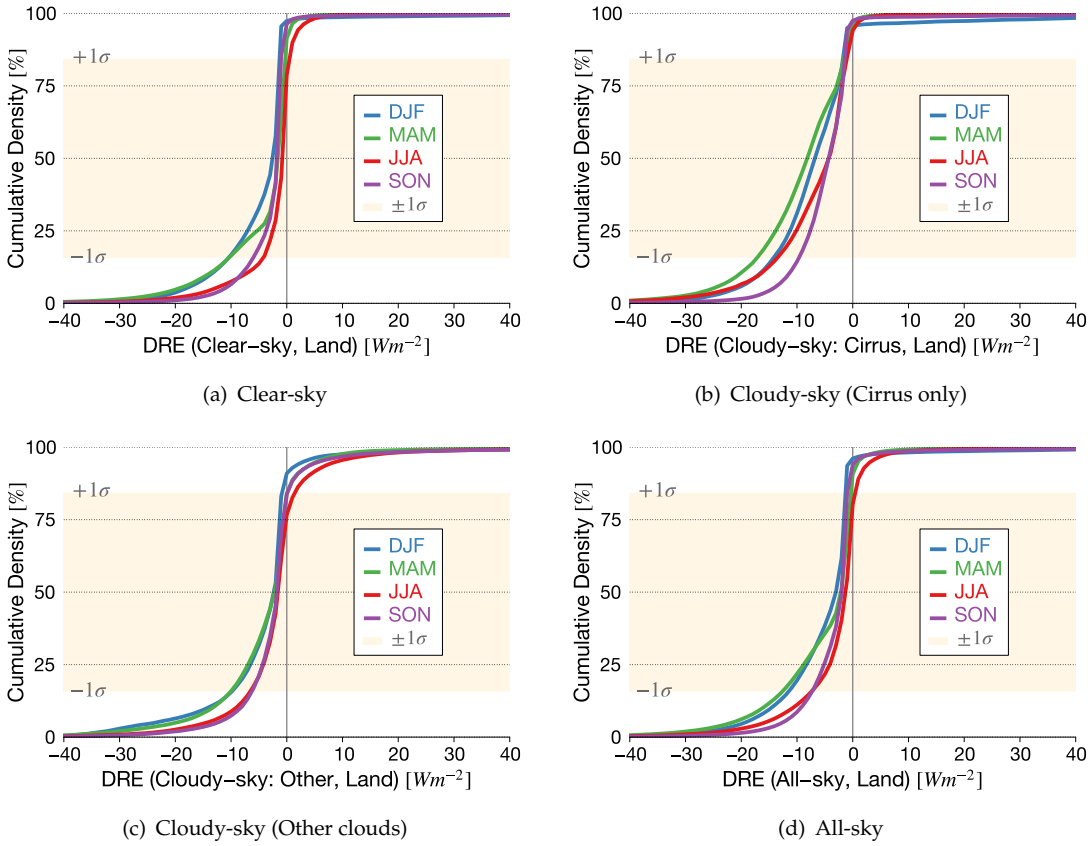

(a) Clear-sky

(b) Cloudy-sky (Cirrus only)

(c) Cloudy-sky (Other clouds)

(d) All-sky

FIGURE 6.10: CDFs of (a) clear-sky DRE, (b) cloudy-sky (cirrus only) DRE, (c) cloudy-sky (other clouds) DRE, and (d) all-sky DRE observed over the 'SAHARA' land region.

Table 6.3 quantifies the contributions of different surface and sky conditions to annual average DRE. Both observations and simulations report strong aerosol direct effects over ocean. Clear-sky DRE values are significantly more negative from observations (-5.9 W m^{-2}) than simulations (-3.5 W m^{-2}). The largest discrepancies between observations and models occur over land. Clear-sky DRE over land is -4.3 W m^{-2} from observations as compared to 0.5 W m^{-2} from the model.

This comparison further reveals that observed cloudy-sky DRE (-2.0 W m^{-2}) is almost exactly opposite of the simulation (2.9 W m^{-2}), with large discrepancies apparent over land and ocean. While observed all-sky DRE (-4.7 W m^{-2}) is strongly negative, simulated DRE (-0.3 W m^{-2}) is neutral. Observations report negative all-sky values over both land and ocean, while CESM simulates a positive value over land and a negative value over ocean.

TABLE 6.3: Estimates of annual average DRE [W m^{-2}] and fractional occurrence [%] for each category over the 'SAHARA', from 2B-FLXHR-ERB (top) and CESM (bottom) datasets. The standard deviations of observed values are shown in parentheses.

2B-FLXHR-ERB Observed DRE and Percent of Total

$[Wm^{-2}]$	Clear-sky	Cloudy-sky (cirrus)	Cloudy-sky (other)	Mixed-sky	All-sky
Land	-4.3 (8.5)	-4.1 (9.5)	-0.8 (12.0)	-2.8 (11.6)	-3.2 (9.8)
Ocean	-7.9 (8.6)	-7.2 (9.0)	-3.7 (10.1)	-4.9 (8.9)	-6.5 (9.3)
Total	-5.9 (8.8)	-5.5 (9.3)	-2.0 (10.6)	-4.6 (10.0)	-4.7 (9.5)
[%]	Clear-sky	Cloudy-sky (cirrus)	Cloudy-sky (other)	Mixed-sky	All-sky
Land	33	6	7	9	56
Ocean	17	3	10	15	44
Total	50	9	17	24	100

CESM Simulated DRE and Percent of Total

$[Wm^{-2}]$	Clear-sky		Cloudy-sky		All-sky
Land	0.5		4.5		2.4
Ocean	-8.8		0.4		-3.9
Total	-3.5		2.9		-0.3
[%]	Clear-sky	Cloudy-sky (high clouds)	Cloudy-sky (low clouds)	Cloudy-sky (mid clouds)	All-sky
Land	36	14	5	4	56
Ocean	22	11	15	3	44
Total	58	25	20	6	100

The treatment of aerosols over land clearly contributes to significant differences between observed and simulated aerosol direct effects over this region. The predominant aerosol type over this region is mineral dust, an absorbing aerosol, although quantifying the precise amount of absorption remains quite challenging. Furthermore, since Saharan dust storms are episodic, distributions of Saharan dust are highly variable at different timescales. A lack of quality measurements over this region produces large discrepancies between observations and model. The most significant discrepancies occur in remote locations over land where ground-based observing stations are limited.

6.4.2 Angola

While northern Africa is dominated by mineral dust, southern Africa experiences a greater diversity of aerosol sources. The 'ANGOLA' region is defined as a box bounded by 25°S, 0°N, 10°W, and 30°E. This region includes Namibia, Botswana, Zambia, and the Democratic Republic of Congo. The featured area of interest is the southeastern Atlantic Ocean.

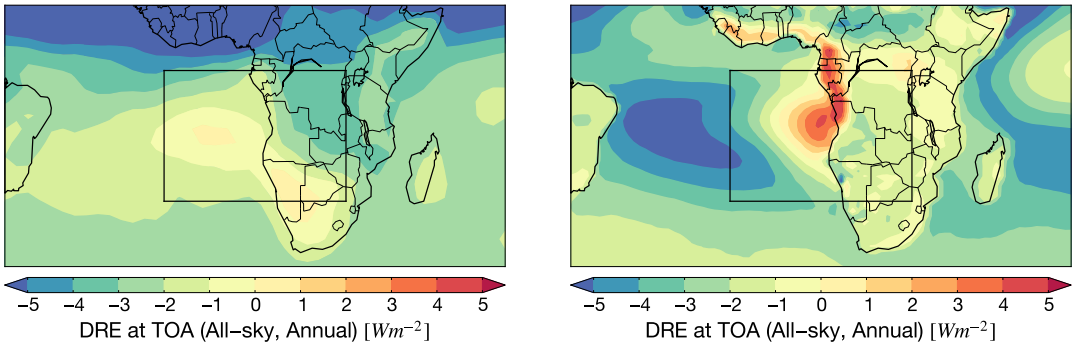

(a) 2B-FLXHR-ERB Observations (b) CESM Simulation

FIGURE 6.11: Maps of annual average all-sky DRE over the 'ANGOLA' region shown from (a) 2B-FLXHR-ERB observations and (b) CESM simulation.

Within the 'ANGOLA' region, the major source of aerosols is from biomass burning. The burning of savanna vegetation in Africa is predominantly human-initiated for land clearing and land-use change. Lightning is also responsible for the initiating biomass burning in this region. Biomass burning releases strongly absorbing carbonaceous aerosols, including black carbon and organic carbon, into the atmosphere. Another major source of aerosols is mineral dust emissions from the Namib Desert in western Namibia.

Maps of annual average all-sky DRE are shown for 2B-FLXHR-ERB observations and CESM simulations in Figure 6.11, where the 'ANGOLA' region is marked by the black rectangular box. These estimates of annual all-sky DRE illustrate that the region is characterized by both regions of positive and negative aerosol direct effects. Within the 'ANGOLA' region, some areas indicate positive values up to 2 W m^{-2}, whereas other areas indicate negative values as low as -2 W m^{-2}. Over land, positive DRE exists at

the southern extent of the region over Namibia and Botswana. Over ocean, positive values are found due west of Angola over the South Atlantic Ocean.

Figure 6.11(b) reveals that similar trends are observed in the spatial distribution of modeled DRE, but CESM tends to produce stronger positive effects in the annual mean than observations. Most notably, there is a bullseye of positive DRE located off the coast of Angola where CESM simulates positive values exceeding 5 W m^{-2}. The origin of this apparent positive DRE off the Angolan coast lies in the seasonal variability in aerosol direct effects.

Similar to the southeast Pacific, the southeast Atlantic supports a semi-permanent deck of marine stratocumulus clouds. Stable, sinking air coupled with cool sea surface temperatures provide ideal environmental conditions for the formation of stratiform clouds off the coast of Angola. Absorbing aerosols transported over this marine stratocumulus deck can produce a positive DRE, or warming of the climate system. Globally, this region presents one of the best examples of this atmospheric phenomenon.

Fires in Africa exhibit a strong seasonal cycle associated with the natural cycle of burning dried savanna and grasslands. The cycle oscillates between the Sahel in DJF to southern Africa in JJA. The evolution of the aerosol warming off the Angolan coast in response to this cycle is shown in Figure 6.12. Biomass burning in Africa is largely confined to the Sahel during DJF. This time period corresponds with the rainy season in southcentral Africa. Over southeast Atlantic, observed all-sky DRE is predominantly negative. Over Namibia, absobring mineral dust from the Namib Desert contributes to positive DRE over land, with values as high as 2 W m^{-2} in some locations.

In MAM, biomass burning in the Sahel begins to subside as the ITCZ shifts northward. There are still few fires in southcentral Africa during this period. Observations indicate all-sky DRE over the ocean reaches a minimum in MAM, during which no positive values are observed over the ocean. Over land, all-sky DRE is predominantly negative with isolated positive values over Namibia and Botswana.

The ITCZ shifts towards the Sahel during JJA, which ushers in the dry season for southcentral Africa. Fires cover an expansive area, including Angola, Zambia, and the Democratic Republic of Congo. Over land, observations show much stronger negative

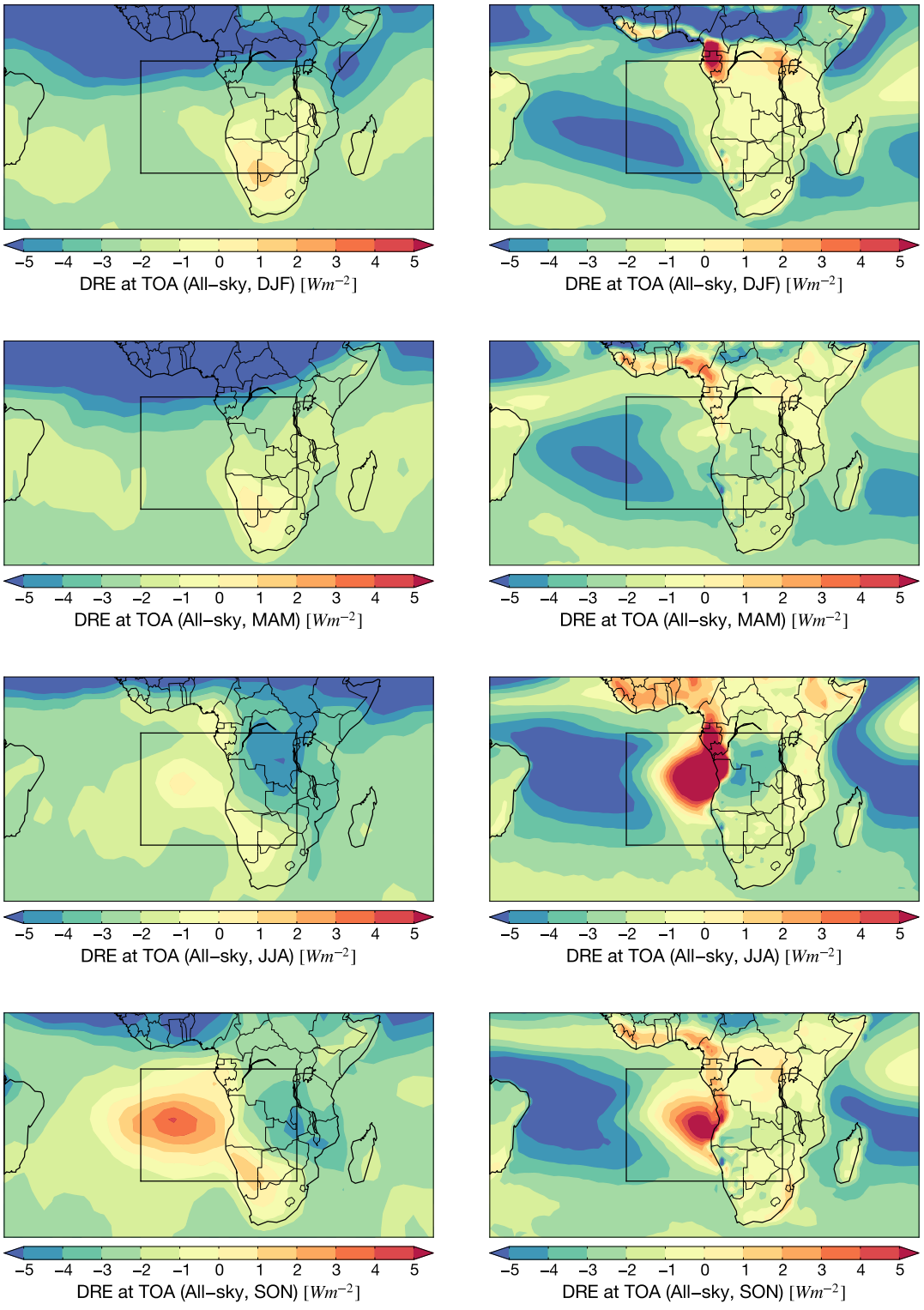

FIGURE 6.12: Maps of seasonally-averaged all-sky DRE over the 'ANGOLA' region from (left) 2B-FLXHR-ERB observations and (right) CESM simulations.

DRE ($<$ -4 W m^{-2}) over these three countries. Positive DRE is observed over bright desert areas of Namibia. Over ocean, there is an area of positive DRE off the coast of Angola with DRE values as high as 1 W m^{-2} during JJA.

By SON, the fires advance further southeast to Zimbabwe and Mozambique. Negative DRE ($<$ -3 W m^{-2}) exists over these countries. Over Namibia, aerosol warming intensifies as values exceed 2 W m^{-2}. The most notable feature in Figure 6.12(d) is the area of positive DRE off the Angolan coast. Much stronger than in JJA, all-sky DRE reaches values of 5 W m^{-2}. The feature extends over 3000 km from the coast of Angola to the middle of the South Atlantic Ocean.

Modeled all-sky DRE reveals a similar trend compared to observations. Averaged within the 'ANGOLA' region, seasonal estimates of observed and simulated DRE are nearly identical. However, Figure 6.12 reveals much stronger spatial variability from CESM simulations. Whereas observed DRE peaks in magnitude during September, modeled DRE is strongest one month earlier in August. During JJA, modeled all-sky DRE reaches as high as 15 W m^{-2} and as low as -5 W m^{-2}. CESM simulates a more gradual amplification which lasts about twice as long as compared to observations. The duration of this cycle, lasting from May through October, corresponds with the biomass burning season in southern Africa.

Despite the biomass burning season lasting from May to October, observations indicate that aerosol direct effects intensify only from August to October. The difference in timing is the main discrepancy between observed and simulated time series of DRE. It should be noted that, over the 'ANGOLA' region, there are two main ingredients for positive DRE: absorbing aerosols and clouds. Both ingredients must be present for a positive DRE to exist. Therefore, biomass burning aerosols that are not transported over marine stratocumulus do not contribute to a positive aerosol direct effect.

Figure 6.13 shows that this strong seasonal cycle is almost exclusively due to cloudy scenes. Cloudy skies are observed in 45% of profiles in SON, compared to only 27% in JJA. Under clear-sky, cirrus-only, and mixed-sky conditions, DRE remains consistent

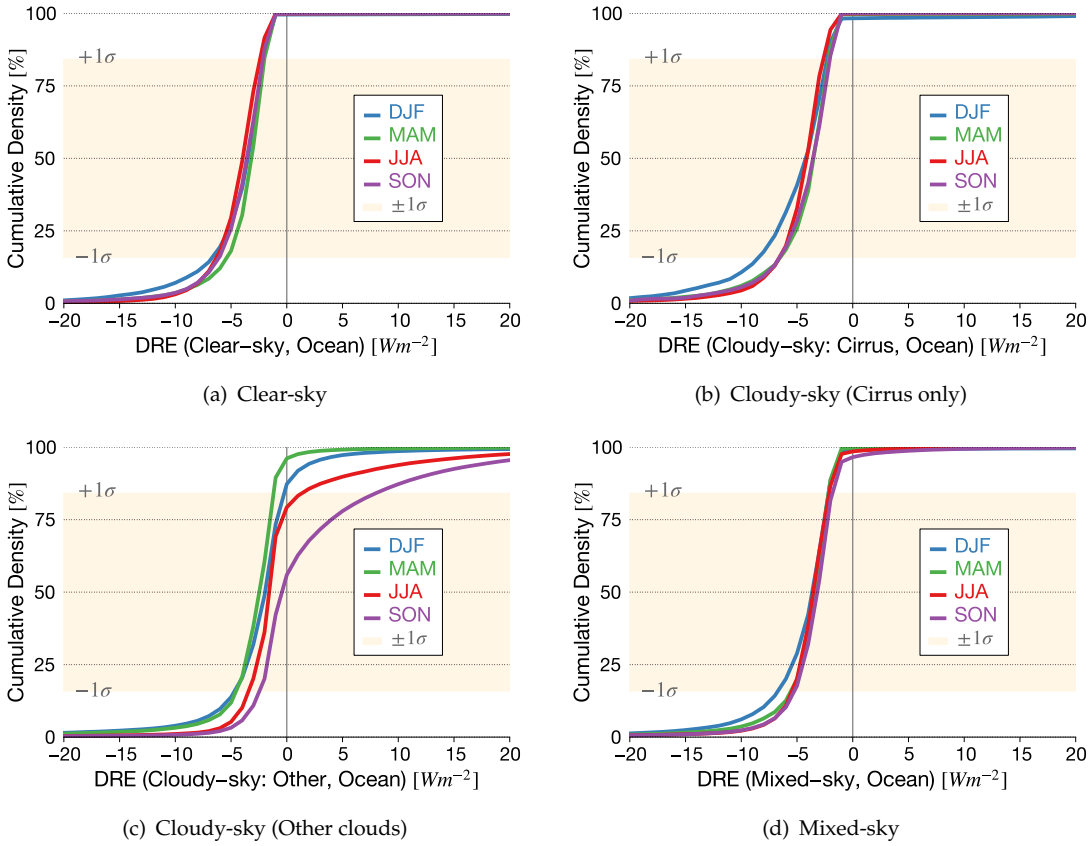

(a) Clear-sky

(b) Cloudy-sky (Cirrus only)

(c) Cloudy-sky (Other clouds)

(d) Mixed-sky

FIGURE 6.13: CDFs of (a) clear-sky DRE, (b) cloudy-sky (cirrus only) DRE, (c) cloudy-sky (other clouds) DRE, and (d) all-sky DRE observed over 'ANGOLA' ocean region.

during all seasons. Observations report similar standard deviations under these conditions. However, Figure 6.13(c) shows that the number and strength of positive DRE observed in profiles containing stratocumulus clouds depends on the season.

Positive values of cloudy-sky DRE are most pronounced in SON, with over 20% of observations indicating DRE greater than 5 W m^{-2}. During SON, cloudy-sky DRE has a standard deviation range of -3 W m^{-2} to 8 W m^{-2}. This result is consistent with seasonal trends observed in Figure 6.11(a). Biomass burning in southern Africa produces a wide range of observed DRE values under cloudy-sky conditions.

The seasonal variability in aerosol direct effects over the southeast Atlantic is strongly dependent on the seasonal variability of marine stratocumulus clouds. Table 6.4 shows the frequency of observed and modeled sky conditions over the 'ANGOLA' ocean region. In both 2B-FLXHR-ERB observations and CESM simulations, clear skies are least

TABLE 6.4: The seasonal frequency of occurrence for DRE over the 'ANGOLA' region, from 2B-FLXHR-ERB (top) and CESM (bottom) datasets.

2B-FLXHR-ERB Percent of Total

[%]	Clear-sky	Cloudy-sky (cirrus)	Cloudy-sky (other)	Mixed-sky	All-sky
DJF	31	8	26	35	100
MAM	30	7	25	38	100
JJA	32	3	40	25	100
SON	19	2	58	21	100

CESM Percent of Total

[%]	Clear-sky	Cloudy-sky (high clouds)	Cloudy-sky (low clouds)	Cloudy-sky (mid clouds)	All-sky
DJF	52	11	40	4	100
MAM	52	10	40	2	100
JJA	50	4	48	0	100
SON	38	5	59	2	100

frequent during SON. However, the model consistently simulates over 15% more clear sky over the southeast Atlantic than observations suggest.

The seasonal frequency of clouds are inconsistent as well. During JJA, cloud skies comprise 40% of observed pixels and 48% of simulated pixels. An increase in simulated low clouds during JJA is likely responsible for the stronger modeled aerosol direct effects during this season. Cloudy skies are also more frequently simulated in this CESM simulation during DJF and MAM than observations.

The southeast Atlantic Ocean is a unique location in that absorbing aerosols are periodically transported over marine stratocumulus clouds. The resulting positive DRE contributes significantly towards altering the radiative balance in this region. However, there exists strong disagreement between observations and models. The ability to accurately simulate DRE over this region requires a more realistic treatment of marine stratocumulus cloud extent and biomass burning aerosol transport in models.

6.5 Asia

6.5.1 India

Whereas aerosol sources in Africa are largely natural in origin, aerosol contributions in Asia are much more influenced by human activity. To contrast observational estimates of aerosol DRE and model performance in these different environments, we examine two regions in Asia. The first region explored is South Asia, which will be followed by a discussion of aerosol direct effects over East Asia.

Defined as a box bounded by 0°N, 30°N, 60°E, and 90°E, the 'INDIA' region encompasses India, southern Pakistan, and the Arabian Sea. This area includes highly populated urban centers, such as Mumbai, Delhi, and Bangalore, which produce high emissions of anthropogenic aerosols. Topography plays an important role in shaping aerosol distributions over India. The highest aerosol concentrations are typically confined to northern India, where the Himalayan Mountains block southerly and westerly flow. Populous cities in northern India, such as Delhi, experience elevated levels of aerosols due to contributions from both local and foreign aerosol sources.

The South Asian monsoon is a largest interannual driver of aerosol transport over this region. The summertime heating of the Indian subcontinent draws in moisture-laden winds from the Indian Ocean. Monsoonal winds also serve to transport mineral dust from the Arabian peninsula across the Arabian Sea to India. Lasting from June through September, the South Asian monsoon accounts for 80% of the rainfall in India (Menon et al., 2013). Seasonal changes in wind and precipitation fields produces significant temporal variability in aerosol distributions over India.

Figure 6.14 exposes large discrepancies in annual average all-sky DRE between 2B-FLXHR-ERB observations and CESM simulations. The largest differences apper to occur over northern India and the Arabian Sea. In some locations, values differ by over 6 W m^{-2} between observations and simulations.

Observed all-sky DRE is negative over the entire domain except for isolated positive values over Pakistan and Tibet. Figure 6.14(a) shows that negative values exceed -10 W m^{-2} in some locations. The strongest aerosol cooling exists over northern India

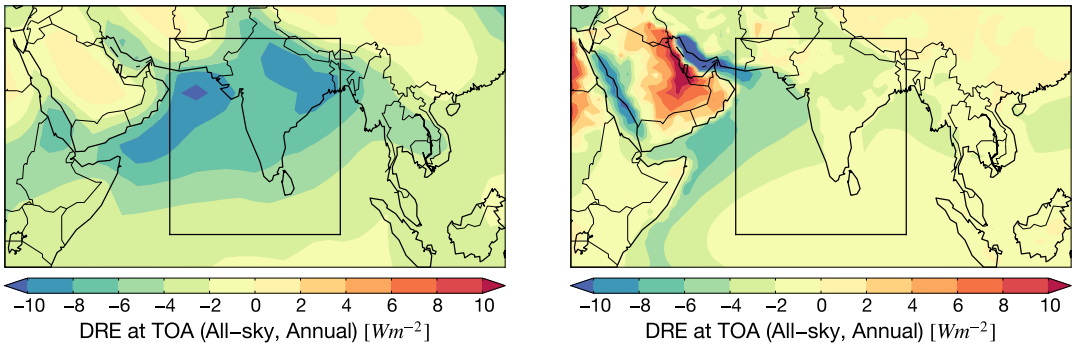

(a) 2B-FLXHR-ERB Observations (b) CESM Simulation

FIGURE 6.14: Maps of annual average all-sky DRE over the 'INDIA' region shown from (a) 2B-FLXHR-ERB observations and (b) CESM simulation.

and the Arabian Sea. Over India, DRE values reach as low as -5 W m^{-2} in some areas. All-sky DRE values over ocean are strongest near the Indian coastline.

The distribution of modeled all-sky DRE reveals a significantly different pattern than observed in the 2B-FLXHR-ERB dataset. Overall, simulated all-sky DRE is considerably weaker than in observations. Over land, values range between -4 W m^{-2} and 2 W m^{-2}. Over ocean, values range between -8 W m^{-2} and 0 W m^{-2}. Whereas the Arabian peninsula exhibits strong warming, the effects over India are nearly negligible. Despite the differences, there are few similarities between observed and modeled DRE. Consistent in both maps, all-sky DRE is relatively strongest over the Arabian Sea.

Similar to the southeast Atlantic, there is evidence that observation-model discrepancies may be linked to differences in their representation of the seasonal cycle. Due to the South Asian Monsoon, India experiences large interannual variability in weather conditions. Heavy precipitation during the summer removes aerosols from the atmosphere, which reduces the impact of aerosol direct effects. The seasonal variability in aerosols is largely influenced by the South Asian Monsoon.

Seasonal cycles of all-sky DRE, based on 2B-FLXHR-ERB observations and CESM simulations, are compared in Figure 6.15 over the land area of the 'INDIA' region. Observed values of DRE at the top-of-atmosphere vary between -7.2 W m^{-2} in May and -2.8 W m^{-2} in September. The peak in all-sky DRE occurs during MAM, which

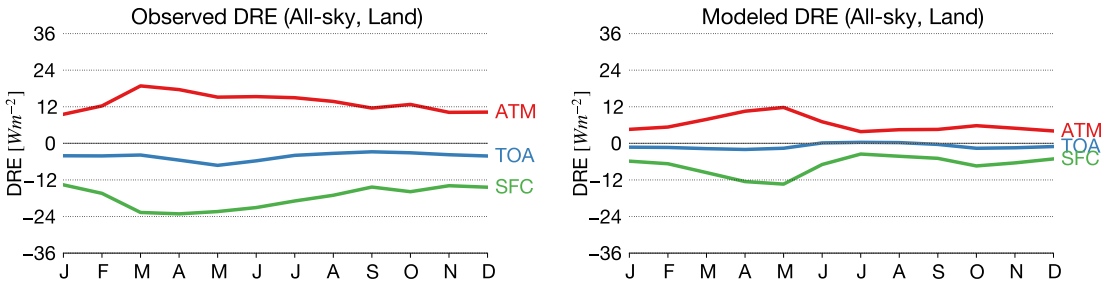

(a) 2B-FLXHR-ERB Observations (b) CESM Simulation

FIGURE 6.15: Seasonal cycle of aerosol atmospheric heating (red), top-of-atmosphere DRE (blue), and surface DRE (green) over the 'INDIA' land region.

corresponds to the season preceeding the South Asian Monsoon. Values decrease in magnitude gradually after May, throughout the remainder of the year.

Simulated DRE exhibits a more pronounced seasonal cycle than observations. Within the atmospheric column and at the surface, DRE reaches its largest magnitude in May and smallest magnitude in July. However, DRE at the top-of-atmosphere remains relatively neutral throughout the year. Simulated DRE at the top-of-atmosphere ranges from -1.6 W m^{-2} in October to 0.3 W m^{-2} in July, which is considerably weaker than observations.

Whereas both plots exhibit a seasonal cycle, the trend is much more pronounced in the CESM simulation. Observations indicate a reduction in DRE magnitudes after the onset of the South Asian Monsoon, however DRE at the top-of-atmosphere remains negative throughout the year. In contrast, CESM simulates a more neutal DRE at the top-of-atmosphere. To further explain descripancies between observed and simulated DRE, CDFs of DRE are presented under various sky conditions in Figure 6.16. Plots are shown for all land surfaces over India, in which each line represents observed DRE within a given season.

Figure 6.16(a), Figure 6.19(b), and Figure 6.16(d) indicate seasonal variability, whereas Figure 6.16(c) does not. Under cloudy-sky conditions, the shapes of the CDFs remains fairly constant by season. Under clear and cloudy skies, the shapes of the CDFs vary greatly by season. Therefore, unlike the southeast Atlantic, the main source of interannual variability is from DRE under clear-sky conditions.

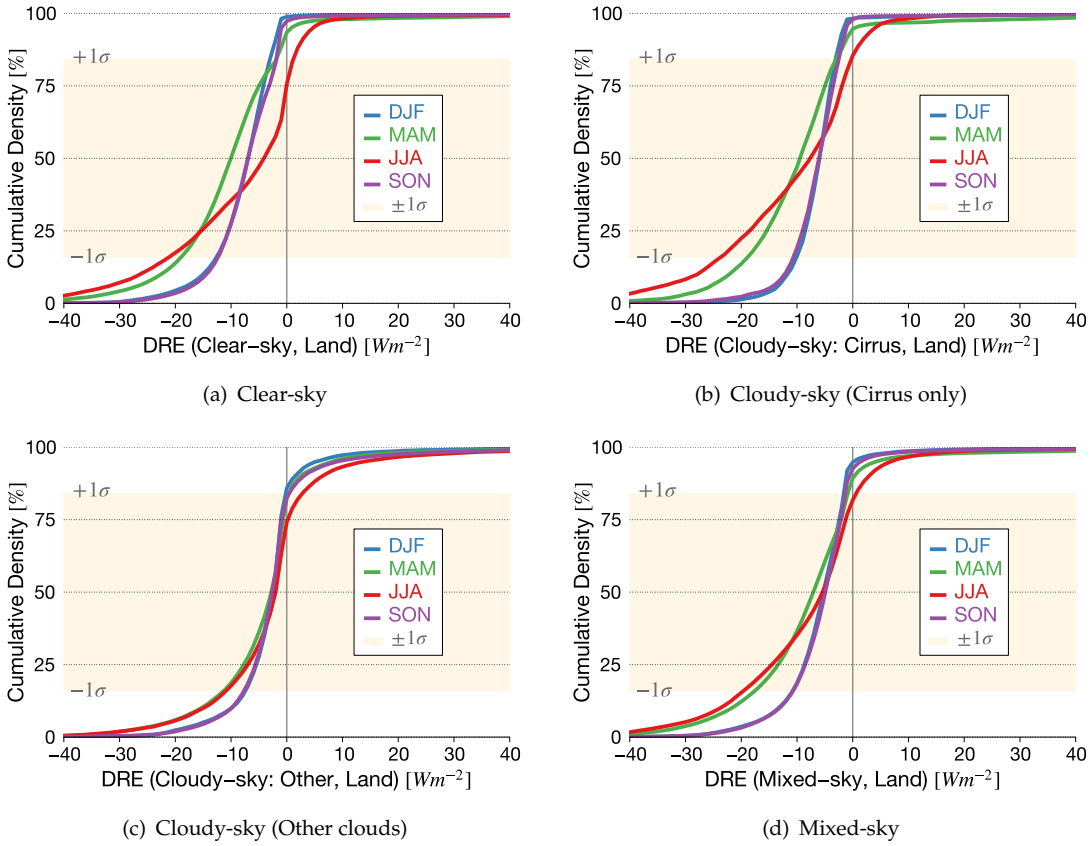

(a) Clear-sky

(b) Cloudy-sky (Cirrus only)

(c) Cloudy-sky (Other clouds)

(d) Mixed-sky

FIGURE 6.16: CDFs of (a) clear-sky DRE, (b) cloudy-sky (cirrus only) DRE, (c) cloudy-sky (other clouds) DRE, and (d) all-sky DRE observed over the 'INDIA' land region.

Clear-sky DRE remains negative throughout most of the year. The season of largest variability is JJA, where one standard deviation of observed clear-sky DRE ranges from -21 W m^{-2} to 1 W m^{-2}. This result is consistent with the wide variability expected during a transition period from a dry season to a wet season. During JJA, over 20% of clear-sky DRE observations are greater than zero. Positive values of DRE support the presence of absorbing aerosols, such as mineral dust, over India.

As a result of these considerations, clear-sky DRE over land is significantly stronger in observations (-5.2 W m^{-2}) than simulations (-2.5 W m^{-2}). In addition, observed cloudy-sky DRE (-3.0 W m^{-2}) is very different than simulated cloudy-sky DRE (1.0 W m^{-2}). As Figure 6.14 showed, observations indicate strong negative DRE over northern India, whereas simulations do not.

TABLE 6.5: The seasonal frequency of occurrence for DRE over the 'INDIA' region, from 2B-FLXHR-ERB (top) and CESM (bottom) datasets.

2B-FLXHR-ERB Percent of Total

[%]	Clear-sky	Cloudy-sky (cirrus)	Cloudy-sky (other)	Mixed-sky	All-sky
DJF	49	11	10	30	100
MAM	50	11	11	28	100
JJA	16	12	39	33	100
SON	39	11	18	31	100

CESM Percent of Total

[%]	Clear-sky	Cloudy-sky (high clouds)	Cloudy-sky (low clouds)	Cloudy-sky (mid clouds)	All-sky
DJF	57	29	7	18	100
MAM	55	29	4	20	100
JJA	22	67	13	21	100
SON	41	45	10	20	100

Similar to the southeast Atlantic, the seasonal variability in aerosol direct effects over South Asia is strongly influenced by the seasonal variability of clouds. The Southeast Asian Monsoon largely controls the temporal and spatial distribution of clouds over India. The seasonal frequency of observed and modeled sky conditions over India is displayed in Table 6.5. Significant discrepancies exist between both tables, suggesting that seasonal cloud cover is inconsistently represented in 2B-FLXHR-ERB observations and CESM simulations.

Seasonal variability in DRE is greatest under clear-sky conditions. Clear skies are more more frequently simulated in CESM than observed in the 2B-FLXHR-ERB dataset. The greatest discrepancy occurs during DJF, in which clear skies are observed in 49% of observed pixels compared to 57% of simulated pixels. Furthermore, high clouds appear more common in the model, reaching a maximum frequency of occurrence of 67% in JJA. Clear-sky observations and simulations are least common during JJA, when precipitation over India is generally most intense.

India hosts a variety of natural and anthropogenic aerosol sources, topographic

effects, and monsoonal variability. Collectively, these factors lead to significantly increased complexity in simulating aerosol direct effects over India. CESM simulations of DRE are vastly different than 2B-FLXHR-ERB observations. The primary discrepancy between observations and simulations exists over northern India and the Arabian Sea. Of all regions considered in this study, observed all-sky DRE is strongest over the 'INDIA' region. For this reason, it is extremely important to resolve these discrepancies in order to improve global assessments of aerosol direct effects.

6.5.2 China

Much like South Asia, East Asia is a significant source of atmospheric aerosols. The 'CHINA' region, defined as a box bounded by 20°S, 45°N, 100°E, and 140°W, includes eastern China, Korea, and Japan. The box also extends into the East China Sea and North Pacific Ocean. The primary focus of this analysis will be on evaluating aerosol direct effects over the land surface of the 'CHINA' region.

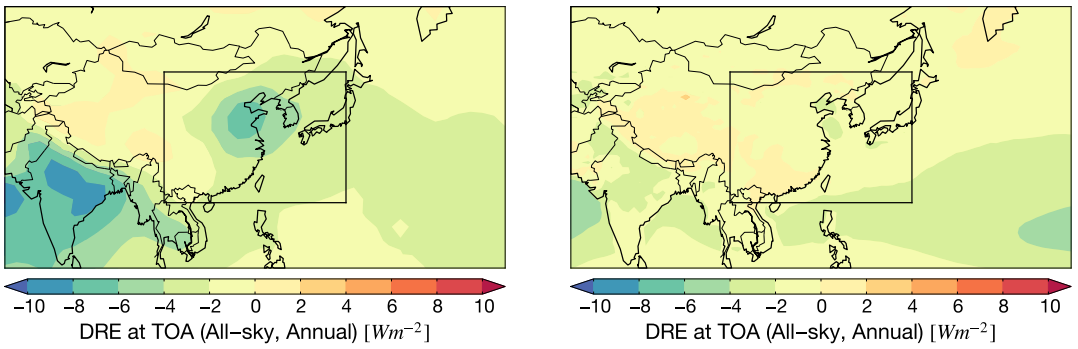

(a) 2B-FLXHR-ERB Observations (b) CESM Simulation

FIGURE 6.17: Maps of annual average all-sky DRE over the 'CHINA' region shown from (a) 2B-FLXHR-ERB observations and (b) CESM simulation.

Anthropogenic emissions are a major source of aerosols over East Asia. The largest contribution of airborne particles in this region originates from mainland China. Eastern China contributes largely urban aerosols, whereas northeastern China contributes industrial aerosols. The Gobi Desert in Mongolia is a major source for mineral dust, which can be transported eastward via strong low-level winds. During MAM, East

Asia is most prone to major dust storms. The diversity of aerosol sources over China gives rise to complex aerosol-radiation interactions in this region.

Annual average all-sky DRE from 2B-FLXHR-ERB observations and CESM simulations are compared in Figure 6.17. The 'CHINA' region is marked by the black rectangular box. Over China, observed all-sky DRE is largely negative, according to Figure 6.17(a). Values are more negative over land than over ocean, where aerosol cooling is largely confined near the coast. A bullseye of strong negative DRE ($<$ -5 W m^{-2}) exists over the populated area between Beijing and Shanghai. Aerosol direct effects are relatively weaker over southwest China and Mongolia.

Simulated all-sky DRE is mapped in Figure 6.17(b). Compared to 6.17(a), results are similar with one notable exception. The bullseye of negative DRE in the map of observed DRE is nonexistent in the map of simulated DRE. Over eastern China, values are no less than -1 W m^{-2}. Conversely, values over southwestern China are more positive and exceed 2 W m^{-2} in some locations.

The absence of aerosol cooling over eastern China is notable feature of the CESM simulation. Eastern China is one of the most populated and industrialized areas of China. Therefore, there is strong circumstanital evidence to support that most aerosols over this location are of anthropogenic origin. The reason for this discrepancy between observed and modeled DRE is unknown at present. However, investigating the seasonal variability in DRE provides hints as to the source behind these differences.

Monthly-averaged all-sky DRE shown in Figure 6.18 from 2B-FLXHR-ERB observations and CESM simulations show significant differences in the magnitude and timing of peak DRE over mainland China. In both cases, DRE within the atmospheric column and at the surface show a peak during the MAM season. This time period corresponds to the dust storm season in East Asia. Mineral dust, an absorbing aerosol, contributes to warming within the atmosphere consistent with both figures. However, only observations show a peak during JJA. During this time period, increased sunlight leads to an elevated production of secondary aerosols. Unlike the model output, observations indicate an increase in aerosol absorption during JJA.

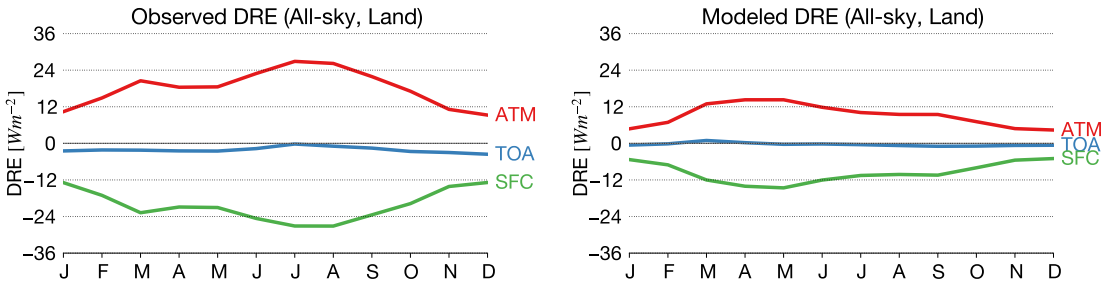

(a) 2B-FLXHR-ERB Observations (b) CESM Simulation

FIGURE 6.18: Seasonal cycle of aerosol atmospheric heating (red), top-of-atmosphere DRE (blue), and surface DRE (green) over the 'CHINA' land region.

The CDFs of DRE are displayed in Figure 6.19 over the 'CHINA' land region. Similar to India, the primary source of interannual variability is from DRE under clear-sky conditions, in which MAM is the season of greatest variability in observed DRE values. Clear-sky DRE is most negative during MAM while more positive values of clear-sky DRE occur during JJA. This result is consistent with the observed JJA peak in Figure 6.18(a). There are 2.6 times as many observations of positive clear-sky DRE during JJA than during any other season. The localized area of aerosol cooling over eastern China considerably influences regionally-averaged values of DRE. Over land, observed all-sky DRE is -2.2 W m^{-2}, which is more than 5 times the CESM estimate of -0.4 W m^{-2}.

These results have potentially important implications for quantifying the effects of anthropogenic aerosol globally. Over industrialized parts of eastern China, anthropogenic aerosols predominate. While the signature of these manmade particles is evident in maps of observed DRE, it is largely absent in maps of simulated DRE from the CESM model examined here. The fact that the treatment of anthropogenic aerosols in the CESM model appears to be significantly different than what is observed in the 2B-FLXHR-ERB dataset has potential implications for model-based assessments of the radiative forcing from anthropogenic aerosols.

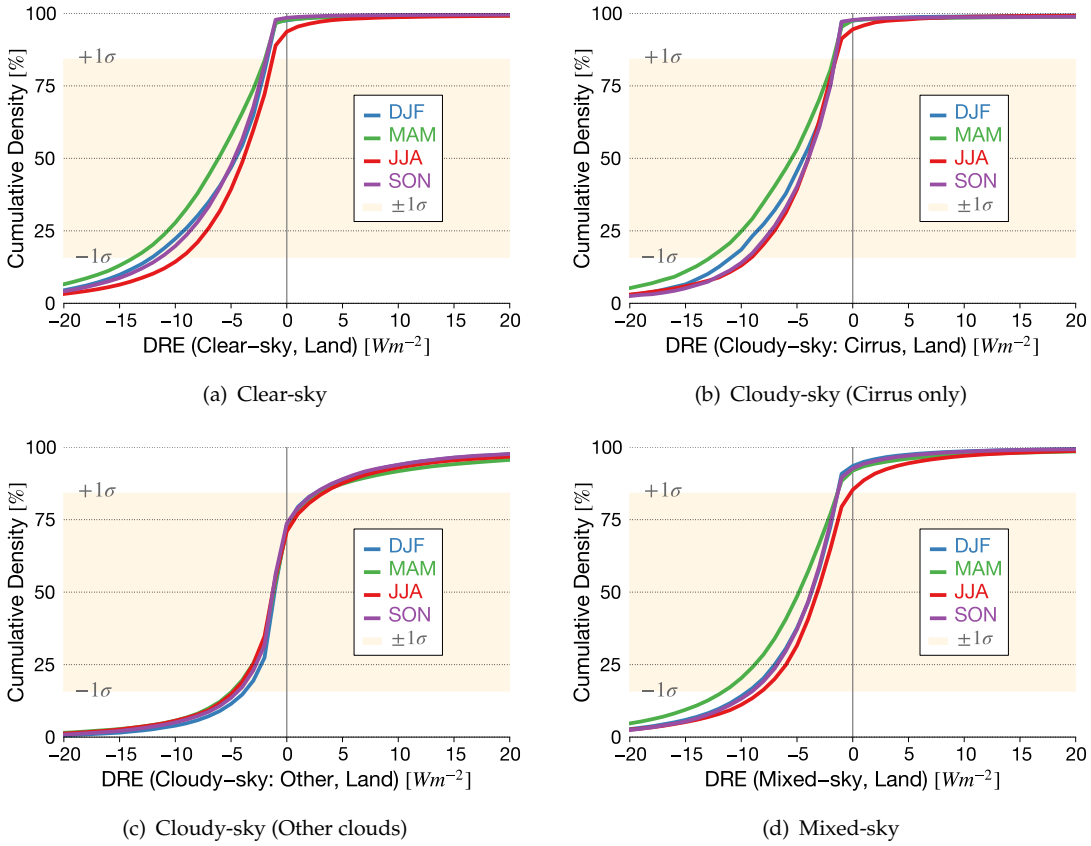

(a) Clear-sky

(b) Cloudy-sky (Cirrus only)

(c) Cloudy-sky (Other clouds)

(d) Mixed-sky

FIGURE 6.19: CDFs of (a) clear-sky DRE, (b) cloudy-sky (cirrus only) DRE, (c) cloudy-sky (other clouds) DRE, and (d) all-sky DRE observed over the 'CHINA' land region.

6.6 Summary and Discussion

In this chapter, six regions were investigated to highlight the regional variability in aerosol direct effects. While global averages provide useful guidance for climate analyses, regional studies reveal localized discrepancies which can be used to improve global model simulations. This study compares observed DRE from the 2B-FLXHR-ERB dataset and simulated DRE from CESM. Results reveal significant inconsistencies between observed and modeled DRE within these regions.

Under certain conditions, the discrepancies between observations and model become quite apparent. Clouds remain a challenging aspect for assessing aerosol direct effects. Whereas cirrus clouds produce effects comparable to clear-sky conditions, optically thicker clouds can drastically alter the radiative impacts of aerosols. For example,

marine stratocumulus is often unrealistically represented in global models. Inconsisent distributions of cloud fields can introduce large systematic errors in DRE simulations. These results are highlighted in the 'CHILE' and 'ANGOLA' regions.

Some aerosol types are more challenging to accurately characterize than others. The presence of mineral dust introduces difficulties for models due to the complex radiative properties of this aerosol type. Mineral dust can exert either a positive or negative aerosol direct effect, depending on the underlying surface reflectivity. Regions including the 'SAHARA' and 'INDIA' reveal large discrepancies between observations in simulations over locations largely influenced by mineral dust.

Anthropogenic aerosols are complicating factors for regional assessments of DRE. The diversity of aerosol compositions and chemical reactions of these particles make them difficult to adequately characterize using current observational techniques. The role of anthropogenic aerosols are explored in the 'USA' and 'CHINA' regions. Despite relatively good agreement over the eastern United States, there are large differences between observations and simulation over eastern China which are likely due to the presence of anthropogenic aerosols.

Overall, regional analyses provide critical benchmarks for improving global assessments of aerosol direct effects. It should be noted, however, that uncertainties in estimates do exist in both satellite-based and model-based approaches. This study featured results from a single CESM model simulation, which is not fully representative of the ensemble of model runs currently available. Also, the 2B-FLXHR-ERB algorithm is subject to uncertainties in observational inputs, including aerosol optical properties. Continued research on aerosol optical properties will lead to improved understanding of their role in influencing future climate.

Chapter 7

Conclusions

Atmospheric aerosols contribute a significant source of uncertainty in our ability to predict future climate. Improved representation of aerosol radiative processes in global models is the key to reducing these uncertainties. Multi-sensor observations from the A-Train satellite constellation provide observational constraints needed to reduce uncertainties in model simulations of aerosol direct effects.

CloudSat's new multi-sensor radiative flux and heating rates product (2B-FLXHR-ERB) is used to evaluate aerosol direct effects both globally and regionally. This approach leverages the capability of CloudSat and CALIPSO to retrieve vertically-resolved estimates of cloud and aerosol properties. Whereas previous satellite-based assessments are typically limited to daytime cloud-free measurements of aerosol properties, the 2B-FLXHR-ERB data product has the ability to quantify aerosol direct effects over thick clouds, under thin cirrus, and at night.

Based on the 2B-FLXHR-ERB data product, the global annual average aerosol direct effect is -2.0 $\pm$ 0.6 W m^{-2}. This estimate is in better agreement with estimates from global models than previous satellite-based estimates. However, regional discrepancies exist between modeled and observed values of aerosol DRE that likely result from inconsistent representations of aerosol optical properties and cloud cover from satellite observations and model simulations.

In Chapter 6, regional cases studies were presented to illustrate the wide spatial variability in aerosol direct effects. These regional analyses reveal that aerosol direct

effects are highly dependent on the surface type and the seasonal distribution of clouds and aerosols.

Mineral dust emissions are significant sources of aerosols over North Africa and South Asia. The radiative properties of mineral dust aerosols, which vary by region, can exert positive and negative effects on climate. Over the Sahara, observed all-sky DRE (-4.7 W m^{-2}) is over 3 W m^{-2} stronger than simulated all-sky DRE (-0.3 W m^{-2}). Similarly, all-sky DRE over India is larger for observations (-5.8 W m^{-2}) than simulations (-2.1 W m^{-2}). The greatest source of discrepancy occurs over bright deserts where CESM simulates much stronger positive DRE compared to observations. Furthermore, the spatial distribution of modeled DRE is more heterogeneous over deserts than suggested by observations. As a result, deserts are areas where there needs to be a concerted effort for improving aerosol measurements.

Marine stratocumulus clouds play an important role in modulating aerosol direct effects. The southeast Pacific and southeast Atlantic are two regions featured in this study with semi-permanent stratocumulus cloud decks. Both 2B-FLXHR-ERB observations and CESM simulations produce comparable DRE estimates over Chile (-1.8 W m^{-2} vs. -2.0 W m^{-2}) and Angola (-1.7 W m^{-2} vs. -1.4 W m^{-2}). While the southeast Pacific has relatively low aerosol concentrations, the southeast Atlantic hosts large concentrations of biomass burning aerosols during boreal summer. These absorbing aerosols overlay bright clouds to cause a localized warming of the climate system over the southeast Atlantic. However, discrepancies between observed and simulated cloud cover results in discrepancies between the spatial distributions of observed and simulated DRE.

Anthropogenic aerosols can produce locally strong direct effects over industrialized countries, such as the United States and China. In both regions, aerosol direct effects exhibit a seasonal cycle which peaks in magnitude during summer. Similar seasonal trends are evident in observations and simulations. However, the magnitude of DRE at the top-of-atmosphere and surface is at least 50% weaker during most months in the CESM simulation as compared to 2B-FLXHR-ERB observations. As a result, DRE

at the top-of-atmosphere is largely inconsistent between the two. Observed and simulated all-sky DRE differ over China (-2.8 W m^{-2} vs. -0.9 W m^{-2}) and the USA (-2.2 W m^{-2} vs. -1.5 W m^{-2}). Over China, stronger DRE is shown over urbanized areas in 2B-FLXHR-ERB observations but not in CESM simulations. Therefore, anthropogenic aerosols likely account for the stronger aerosol direct effects in observations compared to the model.

Research presented in this study is designed to provide an overall assessment of aerosol direct effects using state-of-the-art satellite observations and model simulations. Despite recent advances in aerosol observing and modeling capabilities, there is still much work to be done to improve characterization of aerosol radiative effects.

Different species of aerosols elicit different responses on climate. Since aerosol species have variable optical properties, it is important to understand the relative contribution from each aerosol type individually. Using the aerosol classification from CALIPSO, we may evaluate 2B-FLXHR-ERB direct effects for various aerosol types, including marine, continental, dust, and smoke. Sorting observed DRE by aerosol type may offer valuable insights into quantifying the contribution of anthropogenic aerosols on global and regional aerosol direct effects.

Improving parameterizations of aerosol optical properties is a critical aspect of algorithm development. Working with modeling groups to test new parameterizations of aerosol sources and properties will greatly enhance the 2B-FLXHR-ERB algorithm. Aerosol optical properties calculated using the SPRINTARS global transport model strongly influence radiative transfer through the atmosphere. We plan to conduct sensitivity tests of retrieved single scattering albedo and asymmetry parameter and evaluate against in situ measurements from AERONET.

The 2B-FLXHR-ERB alogrithm can improved upon to produce a more robust representation of environmental factors which influence radiative balance. Future algorithm development plans also include using AIRS temperature and humidity sounding retrievals to reduce dependence on ECMWF analyses. However, it is worth noting that

the source of temperature and humidity information has a negligible impact on estimates of aerosol DRE since this is derived from flux differences. Improved observational inputs will help advance our understanding of the radiative impact of aerosols.

Appendix A

2B-FLXHR-ERB Aerosol Screening

Throughout this study, we presented results from the 2B-FLXHR-ERB dataset using only aerosol-detected profiles. However, there are realistic scenarios in which CALIPSO may not be able to detect aerosols. Lidar measurements are strongly attenuated by most clouds; therefore, CALIPSO has difficulty detecting aerosol features under optically thick clouds. In such cases, the aerosols will have a negligible impact on DRE but these 0 W m^{-2} values represent valid data that should be included in averages.

Furthermore, the tenuous, weakly-scattering edges of cirrus clouds are sometimes misclassified as aerosol by the CALIPSO Cloud Aerosol Discrimination algorithm (Winker et al., 2013). The limitations of CALIPSO aerosol retrievals can translate into systematic biases in the 2B-FLXHR-ERB dataset. Therefore, some non-aerosol profiles screened in the 2B-FLXHR-ERB dataset may actually be valid for analysis of aerosol direct effects.

Figure A.1 shows global maps of annual average DRE for all 2B-FLXHR-ERB profiles (including profiles for which CALIPSO detects no aerosol). The maps shown in Figure A.1 resemble those displayed in Figure 4.3. However, the magnitude of observed values is smaller since non-aerosol profiles contribute 0 W m^{-2}. Sorting DRE by sky conditions lends further insight into the environmental conditions that influence the magnitude and sign of aerosol direct effects.

In Figure A.1(a), the most negative clear-sky DRE exists over western Africa, India, and China. Clear-sky DRE exceeds -10 W m^{-2} in parts of western Africa. The bright

Sahara and Arabian Deserts are the only locations where clear-sky DRE is positive. Positive values of DRE are generally less than 1 W m^{-2}.

The global map of clear-sky DRE is similar to the global distribution of cloudy-sky DRE when only cirrus are considered. Compared to Figure 4.3(b), values are largely reduced over global oceans. The strongest cirrus-only DRE occurs over the Arabian Sea, where values exceed -10 W m^{-2}.

In cloudy skies, positive DRE predominates globally. However, positive values typically do not exceed 2 W m^{-2} at any location. The aerosol warming is most prominant at higher latitudes and over reflective surfaces, such as deserts. Negative values of cloudy-sky DRE is found over two locations: the North Atlantic Ocean and Arabian Sea. Both of these regions experience large contributions from mineral dust emissions.

Similar to Figure 4.3(d), the distribution of mixed-sky DRE resembles the distribution of clear-sky DRE. Mixed-sky DRE is most negative over western Africa, India, and China. Positive mixed-sky DRE exists over the Sahara. Positive values reach 2 W m^{-2}, whereas negative values dip below -10 W m^{-2}. In mixed-sky conditions, negative DRE predominates indicative of a cooling of the climate system.

All-sky DRE is mostly negative as shown in Figure A.1(e). The strongest all-sky DRE is observed over the Arabian Sea, where values approach -8 W m^{-2}. Although the distribution is similar, Figure 4.2(a) reveals considerably stronger aerosol direct effects for aerosol-detected profiles. The largest differences between figures occur at low latitudes, especially equatorial Africa and the Middle East, where DRE is typically largest.

Results show that there are notable differences in distributions of observed DRE depending on whether or not non-aerosol profiles are included in the analysis. While there are certain conditions in which CALIPSO is unable to detect aerosols, CALIPSO remains the premier spaceborne sensor for aerosol observations. In reality, aerosol direct effects likely include all profiles in which CALIPSO detects aerosols as well as those profiles in which remain aerosols remain undetected.

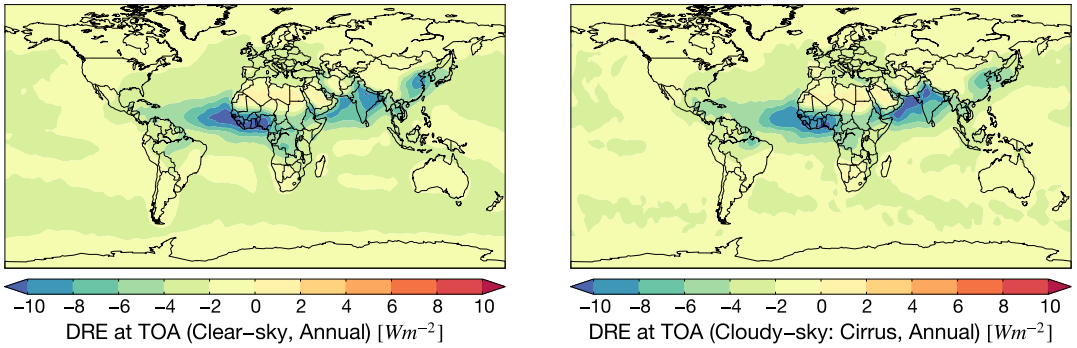

(a) Clear-sky

(b) Cloudy-sky: Cirrus only

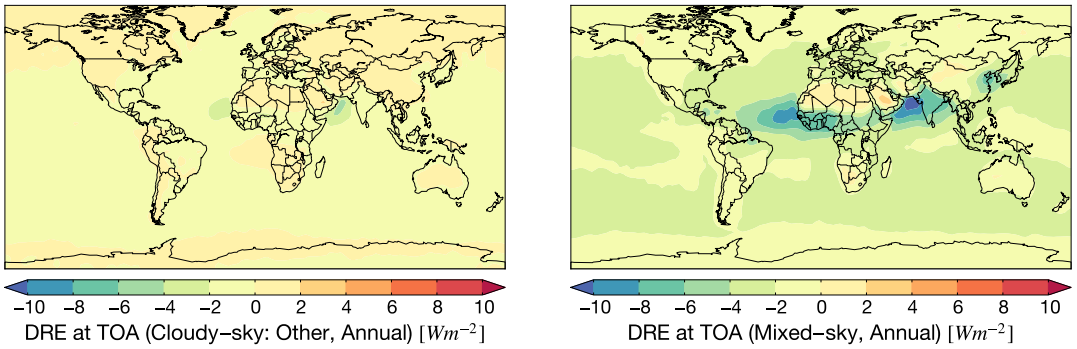

(c) Cloudy-sky: Other Clouds

(d) Mixed-sky

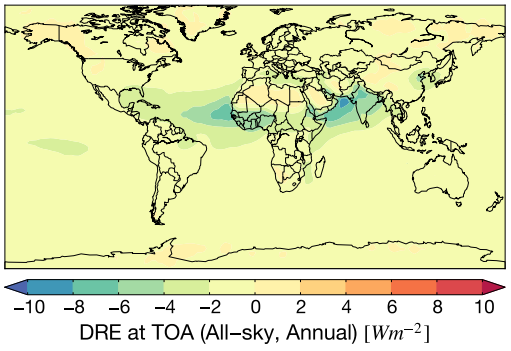

(e) All-sky

FIGURE A.1: Observed annual average DRE for all 2B-FLXHR-ERB profiles.

Bibliography

Albrecht, B. A., 1989: Aerosols, Cloud Microphysics, and Fractional Cloudiness. *Science*, **245 (4923)**, 1227–1230, doi:10.1126/science.245.4923.1227, URL http://www.sciencemag.org/cgi/content/abstract/245/4923/1227.

Balkanski, Y. and M. Schulz, 2007: Reevaluation of mineral aerosol radiative forcings suggests a better agreement with satellite and AERONET data. *Atmosphic Chemistry and Physics*, **(2001)**, 81–95, URL http://www.atmos-chem-phys.net/7/81/2007/acp-7-81-2007.pdf?FrameEngine=false.

Bellouin, N., O. Boucher, J. Haywood, and M. S. Reddy, 2005: Global estimate of aerosol direct radiative forcing from satellite measurements. *Nature*, **438 (7071)**, 1138–1141, URL http://www.ncbi.nlm.nih.gov/pubmed/16372005.

Boucher, O. and D. Tanré, 2000: Estimation of the aerosol perturbation to the Earth's radiative budget over oceans using POLDER satellite aerosol retrievals. *Geophysical research letters*, **27 (8)**, 1103–1106, URL http://www.agu.org/pubs/crossref/2000/1999GL010963.shtml.

CCSP, 2009: Atmospheric Aerosol Properties and Climate Impacts. Tech. Rep. January, NASA, 128 pp. URL http://purl.access.gpo.gov/GPO/LPS110658.

Chand, D., et al., 2012: Aerosol optical depth increase in partly cloudy conditions. *Journal of Geophysical Research: Atmospheres*, **117 (D17)**, doi:10.1029/2012JD017894, URL http://doi.wiley.com/10.1029/2012JD017894.

Charlson, R. J., S. E. Schwartz, J. M. Hales, R. D. Cess, J. A. Coakley, J. E. Hansen, and D. J. Hofmann, 1992: Climate forcing by anthropogenic aerosols. *Science*,

255 (5043), 423–430, URL http://www.sciencemag.org/content/255/5043/423.short.

Chin, M., P. Ginoux, and S. Kinne, 2002: Tropospheric aerosol optical thickness from the GOCART model and comparisons with satellite and Sun photometer measurements. *Journal of the Atmospheric Sciences*, 461–483, URL http://journals.ametsoc.org/doi/abs/10.1175/1520-0469(2002)059%3C0461:TAOTFT%3E2.0.CO%3B2.

Diner, D. J., J. C. Beckert, G. W. Bothwell, and J. I. Rodriguez, 2002: Performance of the MISR instrument during its first 20 months in Earth orbit. 1449–1466 pp., doi:10.1109/TGRS.2002.801584.

Dubovik, O. and B. Holben, 2002: Variability of absorption and optical properties of key aerosol types observed in worldwide locations. *Journal of the Atmospheric Sciences*, **(ii)**, 590–608, URL http://journals.ametsoc.org/doi/abs/10.1175/1520-0469(2002)059%3C0590:VOAAOP%3E2.0.CO%3B2.

Eck, T. F., 2003: Variability of biomass burning aerosol optical characteristics in southern Africa during the SAFARI 2000 dry season campaign and a comparison of single scattering albedo estimates from radiometric measurements. *Journal of Geophysical Research*, **108 (D13)**, 8477, doi:10.1029/2002JD002321, URL http://doi.wiley.com/10.1029/2002JD002321.

Forster, P., V. Ramaswamy, and P. Artaxo, 2007: Changes in Atmospheric Constituents and in Radiative Forcing. *Climate Change 2007 The Physical Science Basis Contribution of Working Group I to the Fourth Assessment Report of the Intergovernmental Panel on Climate Change*, **AR4**, 129–234, URL http://www.ipcc.ch/publications_and_data/publications_ipcc_fourth_assessment_report_wg1_report_the_physical_science_basis.htm.

Fu, Q. and K. N. Liou, 1992: On the correlated k-distribution method for radiative transfer in nonhomogeneous atmospheres. *Journal of the Atmospheric Sciences*, **49 (22)**, 2139–2156.

Haywood, J. M., 2003: The mean physical and optical properties of regional haze dominated by biomass burning aerosol measured from the C-130 aircraft during SAFARI 2000. *Journal of Geophysical Research*, **108 (D13)**, 8473, doi:10.1029/2002JD002226, URL http://doi.wiley.com/10.1029/2002JD002226.

Henderson, D. S. and T. S. L'Ecuyer, 2011: Level 2B Fluxes and Heating Rates and 2B Fluxes and Heating Rates w / Lidar Process Description and Interface Control Document. Tech. Rep. D, 1–28 pp.

Henderson, D. S., T. LEcuyer, G. Stephens, P. Partain, and M. Sekiguchi, 2013: A Multisensor Perspective on the Radiative Impacts of Clouds and Aerosols. *Journal of Applied Meteorology and Climatology*, **52 (4)**, 853–871, doi:10.1175/JAMC-D-12-025.1, URL http://journals.ametsoc.org/doi/abs/10.1175/JAMC-D-12-025.1.

Kahn, R. A., 2005: Multiangle Imaging Spectroradiometer (MISR) global aerosol optical depth validation based on 2 years of coincident Aerosol Robotic Network (AERONET) observations. *Journal of Geophysical Research*, **110 (D10)**, 1–16, doi:10.1029/2004JD004706, URL http://www.agu.org/pubs/crossref/2005/2004JD004706.shtml.

Kay, J. E., et al., 2012: Exposing Global Cloud Biases in the Community Atmosphere Model (CAM) Using Satellite Observations and Their Corresponding Instrument Simulators. *Journal of Climate*, **25 (15)**, 5190–5207, doi:10.1175/JCLI-D-11-00469.1, URL http://journals.ametsoc.org/doi/abs/10.1175/JCLI-D-11-00469.1.

Kittaka, C., D. M. Winker, M. a. Vaughan, a. Omar, and L. a. Remer, 2011: Intercomparison of column aerosol optical depths from CALIPSO and MODIS-Aqua. *Atmospheric Measurement Techniques*, **4 (2)**, 131–141, doi:10.5194/amt-4-131-2011, URL http://www.atmos-meas-tech.net/4/131/2011/.

Koch, D., 2005: Distant origins of Arctic black carbon: A Goddard Institute for Space Studies Model-E experiment. *Journal of Geophysical Research*, **110 (D4)**, D04 204, doi:10.1029/2004JD005296, URL http://doi.wiley.com/10.1029/2004JD005296.

L'Ecuyer, T. S., N. B. Wood, T. Haladay, G. L. Stephens, and P. W. Stackhouse, 2008: Impact of clouds on atmospheric heating based on the R04 CloudSat fluxes and heating rates data set. *Journal of Geophysical Research*, **113**, D00A15, doi:10.1029/2008JD009951, URL http://doi.wiley.com/10.1029/2008JD009951.

Loeb, N. and N. Manalo-Smith, 2005: Top-of-atmosphere direct radiative effect of aerosols over global oceans from merged CERES and MODIS observations. *Journal of Climate*, 3506–3526, URL http://journals.ametsoc.org/doi/pdf/10.1175/JCLI3504.1.

Loeb, N. G., N. Manalo-Smith, K. Loukachine, S. Kato, and B. A. Wielicki, 2002: Advances in top-of-atmosphere radiative flux estimation from the Clouds and the Earth's Radiant Energy System (CERES) satellite instrument. doi:10.1109/IGARSS.2002.1025753.

Mahowald, N. M., D. R. Muhs, S. Levis, P. J. Rasch, M. Yoshioka, C. S. Zender, and C. Luo, 2006: Change in atmospheric mineral aerosols in response to climate: Last glacial period, preindustrial, modern, and doubled carbon dioxide climates. *Journal of Geophysical Research*, **111 (D10)**, D10 202, doi:10.1029/2005JD006653, URL http://doi.wiley.com/10.1029/2005JD006653.

Menon, A., A. Levermann, and J. Schewe, 2013: Enhanced future variability during India's rainy season. *Geophysical Research Letters*, n/a–n/a, doi:10.1002/grl.50583, URL http://doi.wiley.com/10.1002/grl.50583.

Mikami, M., et al., 2006: Aeolian dust experiment on climate impact: An overview of JapanChina joint project ADEC. *Global and Planetary Change*, **52 (1-4)**, 142–172, doi:10.1016/j.gloplacha.2006.03.001, URL http://linkinghub.elsevier.com/retrieve/pii/S092181810600035X.

Moody, E. G., M. D. King, S. Member, S. Platnick, and C. B. Schaaf, 2005: Spatially Complete Global Spectral Surface Albedos : Value-Added Datasets Derived From Terra MODIS Land Products. **43 (1)**, 144–158.

NRC, 2005: *Radiative Forcing of Climate Change: Expanding the Concept and Addressing Uncertainties*. National Academies Press, URL http://books.google.com/books?id=nWKlVLa5N0sC.

Ocko, I. B., V. Ramaswamy, P. Ginoux, Y. Ming, and L. W. Horowitz, 2012: Sensitivity of scattering and absorbing aerosol direct radiative forcing to physical climate factors. *Journal of Geophysical Research*, **117 (D20)**, D20 203, doi:10.1029/2012JD018019, URL http://www.agu.org/pubs/crossref/2012/2012JD018019.shtml.

Ramanathan, V., P. J. Crutzen, J. T. Kiehl, and D. Rosenfeld, 2001: Aerosols, climate, and the hydrological cycle. *Science*, **294 (5549)**, 2119–24, doi:10.1126/science.1064034, URL http://www.ncbi.nlm.nih.gov/pubmed/11739947.

Reddy, M. S., 2005: Estimates of global multicomponent aerosol optical depth and direct radiative perturbation in the Laboratoire de Météorologie Dynamique general circulation model. *Journal of Geophysical Research*, **110 (D10)**, D10S16, doi:10.1029/2004JD004757, URL http://doi.wiley.com/10.1029/2004JD004757.

Remer, L. A. and Y. J. Kaufman, 2006: Aerosol direct radiative effect at the top of the atmosphere over cloud free ocean derived from four years of MODIS data. *Atmospheric Chemistry and Physics*, **6 (1)**, 237–253, doi:10.5194/acp-6-237-2006, URL http://www.atmos-chem-phys.net/6/237/2006/.

Remer, L. A., et al., 2005: The MODIS Aerosol Algorithm, Products, and Validation. *Journal of the Atmospheric Sciences*, **62 (4)**, 947–973, doi:10.1175/JAS3385.1, URL http://journals.ametsoc.org/doi/abs/10.1175/JAS3385.1.

Ritter, B. and J.-F. Geleyn, 1992: A Comprehensive Radiation Scheme for Numerical Weather Prediction Models with Potential Applications

in Climate Simulations. *Monthly Weather Review*, **120 (2)**, 303–325, doi:10.1175/1520-0493(1992)120⟨0303:ACRSFN⟩2.0.CO;2, URL http://cat.inist.fr/?aModele=afficheN&cpsidt=5205974.

Schulz, M., et al., 2006: Radiative forcing by aerosols as derived from the AeroCom present-day and pre-industrial simulations. *Atmospheric Chemistry and Physics*, **6 (12)**, 5225–5246, doi:10.5194/acp-6-5225-2006, URL http://www.atmos-chem-phys.net/6/5225/2006/.

Shindell, D. T., et al., 2013: Radiative forcing in the ACCMIP historical and future climate simulations. *Atmospheric Chemistry and Physics*, **13 (6)**, 2939–2974, doi:10.5194/acp-13-2939-2013, URL http://www.atmos-chem-phys.net/13/2939/2013/.

Smirnov, A., B. N. Holben, T. F. Eck, O. Dubovik, and I. Slutsker, 2000: Cloud-Screening and Quality Control Algorithms for the {AERONET} Database. *Remote Sensing of Environment*, **73 (3)**, 337–349, doi:10.1016/S0034-4257(00)00109-7, URL http://www.sciencedirect.com/science/article/pii/S0034425700001097.

Takemura, T. and T. Nakajima, 2002: Single-scattering albedo and radiative forcing of various aerosol species with a global three-dimensional model. *Journal of Climate*, 333–352, URL http://journals.ametsoc.org/doi/abs/10.1175/1520-0442(2002)015%3C0333%3ASSAARF%3E2.0.CO%3B2.

Tegen, I. and I. Fung, 1995: Contribution to the atmospheric mineral aerosol load from land surface modification. *Journal of Geophysical Research*, **100 (D9)**, 18 707–18 726, doi:10.1029/95JD02051, URL http://dx.doi.org/10.1029/95JD02051.

Twomey, S., 1974: Pollution and the planetary albedo. *Atmospheric Environment*, **8 (12)**, 1251–1256, doi:10.1016/0004-6981(74)90004-3, URL http://www.sciencedirect.com/science/article/pii/0004698174900043.

Winker, D. M., J. L. Tackett, B. J. Getzewich, Z. Liu, M. a. Vaughan, and R. R. Rogers, 2013: The global 3-D distribution of tropospheric aerosols as characterized by CALIOP. *Atmospheric Chemistry and Physics*, **13 (6)**, 3345–3361, doi:10.5194/acp-13-3345-2013, URL http://www.atmos-chem-phys.net/13/3345/2013/.

Wong, J. and Z. Li, 2002: Retrieval of optical depth for heavy smoke aerosol plumes: uncertainties and sensitivities to the optical properties. *Journal of the Atmospheric Sciences*, 250–261, URL http://journals.ametsoc.org/doi/abs/10.1175/1520-0469(2002)059%3C0250%3AROODFH%3E2.0.CO%3B2.

Worley, P. and A. Craig, 2011: Performance of the community earth system model. *High Performance Computing*, URL http://ieeexplore.ieee.org/xpls/abs_all.jsp?arnumber=6114445.

Yu, H., 2004: Direct radiative effect of aerosols as determined from a combination of MODIS retrievals and GOCART simulations. *Journal of Geophysical Research*, **109 (D3)**, D03 206, doi:10.1029/2003JD003914, URL http://doi.wiley.com/10.1029/2003JD003914.

Yu, H., et al., 2006: A review of measurement-based assessments of the aerosol direct radiative effect and forcing. *Atmospheric Chemistry and Physics*, **6 (3)**, 613–666, doi:10.5194/acp-6-613-2006, URL http://www.atmos-chem-phys.net/6/613/2006/.

Zhang, J., 2005: Shortwave aerosol radiative forcing over cloud-free oceans from Terra: 2. Seasonal and global distributions. *Journal of Geophysical Research*, **110 (D10)**, D10S24, doi:10.1029/2004JD005009, URL http://doi.wiley.com/10.1029/2004JD005009.